

HIGH PRESSURE PHASE TRANSFORMATIONS IN POLYCRYSTALLINE

YTTRIUM OXIDE

by

STUART DEUTSCH

A Dissertation submitted to the

Graduate School-New Brunswick

Rutgers, The State University of New Jersey

in partial fulfillment of the requirements

for the degree of

Doctor of Philosophy

Graduate Program in Materials Science and Engineering

written under the direction of

Dr. Bernard H. Kear

and approved by

New Brunswick, New Jersey

October, 2012

ABSTRACT OF THE DISSERTATION

High Pressure Phase Transformations in Polycrystalline Yttrium Oxide

By STUART DEUTSCH

Dissertation Director:
Dr. Bernard H. Kear

Numerous studies have been performed on high-pressure/high temperature phase transitions in rare-earth sesquioxides. Most of these studies were performed using diamond-anvil presses, which limits the size of samples that can be processed. Hence, studies of microstructural and properties changes accompanying phase transitions have been largely neglected.

The purpose of this study has been to fill this gap, working with polycrystalline cubic- Y_2O_3 because of its importance in IR window and dome applications. We selected Diamond Materials Inc. as partner in this investigation, since this company has the expertise to make test pieces under well-controlled HPHT-processing conditions, thus ensuring that the results obtained for one batch of samples to the next are reproducible. This turned out to be crucial, since variations in applied pressure (1.0 to 8.0 GPa range), and holding times (seconds to hours), resulted in significant changes in observed micro/nano-structures. The temperature was fixed at 1000°C in order to limit HPHT-processing variables to pressure and holding time. In view of the results reported here, it now seems

clear that extending the investigation to higher temperatures and lower pressures would be productive.

The principal accomplishments of this research are as follows: (1) optimization of a *reversible-phase transformation* process to convert polycrystalline cubic- Y_2O_3 into the nanocrystalline state, involving a *forward-phase transformation* from cubic-to-monoclinic (c-to-m) Y_2O_3 at a high pressure (8.0 GPa) followed by a *reverse-phase transformation* from monoclinic-to-cubic (m-to-c) Y_2O_3 at a lower pressure (1.0 GPa); (2) discovery of a *transformation-induced crystallization* process to convert polycrystalline c- Y_2O_3 into *columnar-grained* m- Y_2O_3 , and possibly into *single-crystal* m- Y_2O_3 - the driving force is attributed to a pressure-induced phase transformation that occurs at the tips of the growing columnar-grains; (3) formation of a mixed-phase (c- Y_2O_3 /m- Y_2O_3) nanocomposite due to incomplete reverse transformation from m-to-c Y_2O_3 - a near 50:50 nanocomposite displays the highest hardness; and (4) insight into infiltration of carbon-containing gases (e.g. CO, CO_2), formed via reactions between carbon heater and entrapped gases (e.g. O_2 , H_2O) in the pressure cell, into *cracked* grain boundaries to form carbon particles/films via a *vapor-deposition* mechanism, and into *uncracked* grain boundaries to form carbon-rich species via a *boundary-diffusion* mechanism.

DEDICATION

This work is dedicated to my grandfather, Baruch Meilik, who often spoke of the value of education and pursuit of knowledge. His love, encouragement, words of wisdom, and many lessons will continue to encourage and guide me.

ACKNOWLEDGEMENTS

This work would not have been possible without: the guidance of and many insightful discussions with my thesis advisor, Dr. Bernard H. Kear; insight from my co-advisor Dr. Stephen D. Tse; experiments conducted at Diamond Materials Inc. by Dr. Oleg A. Voronov; equipment training by and experienced perspectives of Dr. Jafar Al-Sharab and Dr. Rajendra Sadangi; Y_2O_3 samples provided by Scott Nordahl at Raytheon IDS; and the Office of Naval Research who supported this work with Grant No. N00014-08-1-1029.

Deepest gratitude to my thesis committee members for their insight, feedback, and suggestions:

Prof. Bernard H. Kear

Prof. Stephen D. Tse

Prof. Lisa C. Klein

Prof. Thomas Tsakalakos

Dr. Oleg A. Voronov (Diamond Materials Inc.)

I am immeasurably grateful for the unconditional support of my parents, Rachel and Sol, my twin sister Esther, and my family, for their continued encouragement.

Last but certainly not least, thank you to my wife, Janice, for her unwavering love, support, and motivating words.

Table of Contents

Abstract	ii
Dedication	iv
Acknowledgements	v
Table of Contents	vi
List of Tables	xi
List of Figures	xii
1 Introduction	1
2 Background	5
2.1 Rare Earth Sesquioxide Polymorphs	5
2.2 High-Temperature Polymorphs	6
2.3 R_2O_3 Crystallographic Structures	7
2.4 Fields of Polymorph Stability	9
2.5 Pressure-Assisted R_2O_3 Transformations	13
2.6 Y_2O_3 Polymorphs	19
2.6.1 Cubic Y_2O_3 Structure	19
2.6.2 Y_2O_3 Phase transitions	20
2.6.3 High-Temperature Phase	24
2.6.4 Monoclinic Y_2O_3 Synthesis	25
2.7 Cubic Y_2O_3 Window and Dome Fabrication	26
2.8 Cubic Y_2O_3 Optical and Mechanical Performance	27
2.9 Discussion	31
3 Objectives	32

4	Experimental Methods	34
4.1	Experimental Setup – High Pressure and Temperature Processing	34
4.1.1	Apparatus	34
4.1.2	Methods.....	37
4.1.3	Calibration	38
4.1.4	Dimensional Changes and Complex Stress Conditions.....	41
4.2	Analytical Techniques	43
4.2.1	X-Ray Diffraction	43
4.2.2	Optical Microscopy	45
4.2.3	Nano-Indentation	46
4.2.4	Micro-Hardness	46
4.2.5	Raman Spectroscopy	47
4.2.6	SEM Imaging	48
4.2.7	EDS Analysis	49
4.2.8	TEM Analysis.....	50
4.2.9	XPS Analysis	51
4.2.10	Archimedes Density	51
4.2.11	Sample Fracturing.....	52
4.2.12	Sample Polishing and Surface Preparation	53
5	Cubic Y ₂ O ₃ Physical and Chemical Characterization	55
5.1	As-Received Samples.....	55
5.2	SEM Imaging of Fracture Surface Microstructure.....	56
5.3	EDS Characterization.....	57

5.4	X-ray Diffraction.....	58
5.5	Raman Spectroscopy	59
5.6	Density and Hardness	59
6	Monoclinic Y_2O_3 Physical and Chemical characterization	60
6.1	Initial Observations	60
6.2	X-ray Diffraction.....	61
6.3	SEM Imaging	62
6.4	EDS Chemical Analysis	63
6.5	TEM Analysis	64
6.6	Raman Spectroscopy	66
6.7	Density and Hardness	67
7	Reversible Phase Transformation.....	68
7.1	Overview	68
7.1.1	Prior Research.....	68
7.1.2	Current Research	72
7.2	Changes in Sample Dimensions	77
7.3	Cubic-to-Monoclinic (Forward) Transformation.....	80
7.3.1	Influence of Pressure	83
7.3.2	Incomplete Phase Transformation	85
7.3.3	Transformation Mechanism	87
7.3.4	Crystal Growth	92
7.3.5	Conclusions	94
7.4	Monoclinic-to-Cubic (Reverse) Transformation	98

7.4.1	Influence of Temperature and Holding Time	99
7.4.2	Mixed-Phase Nanocomposite	102
7.4.3	XRD vs. Raman Analysis	103
7.4.4	Conclusions	106
8	Interactions with Carbon Heater.....	108
8.1	Carbon Infiltration	110
8.2	Carbon Diffusion	119
8.3	Grain Coarsening	123
8.4	Conclusions	127
9	Measurement of Hardness	128
9.1	Effect of Phase Transformation.....	129
9.2	Effect of Pressure.....	133
9.3	Effect of Temperature	136
9.4	Conclusions	137
10	Summary and Discussion	139
10.1	Reversible Phase Transformation.....	140
10.2	Forward Phase Transformation.....	142
10.3	Reverse Phase Transformation	144
10.4	Crystal Growth.....	146
10.5	Powder Processing	149
11	Appendices.....	153
	A: Nanopowder Solution Synthesis & Densification	153
	A1: Y_2O_3 Nanopowder Synthesis	153

	A2: Single-Step Consolidation and Densification via HPHT Processing	154
	B: X-Ray Diffraction Powder Diffraction Files (PDF).....	157
	C: Full-range Raman Spectra for c-Y ₂ O ₃ and m-Y ₂ O ₃ With 633nm Source	160
	D: Monoclinic Y ₂ O ₃ JEMS Simulation for TEM Analysis.....	161
	E: XRD Holder Designs	163
12	References	165

List of Tables

Table 2-1 Pressure and temperature conditions used in synthesis of B-type sesquioxides	17
Table 2-2 Critical parameters for pressure-assisted Y_2O_3 transformations.	22
Table 2-3 Physical and mechanical properties of several IR window materials	28
Table 4-1 Pressure dependence of phase transitions in several materials at ambient temperature, used to calibrate pressure	38
Table 5-1 Raman shift for as-received cubic Y_2O_3	59
Table 6-1 Raman shift peak list for transformed monoclinic Y_2O_3	66
Table 7-1 Density and grain size of Y_2O_3 samples after processing at 1.0-8.0 GPa/1000°C/240 min.	84
Table 7-2 Comparison of physical properties of reference samples	99
Table 7-3 Monoclinic-to-cubic Y_2O_3 transformation for samples processed at 1.0 GPa for varying temperature and holding time.....	100
Table 8-1 Density and grain size measurements for samples processed at given pressures at 1000°C and 240mins.	123
Table 9-1 Density, grain size, and hardness measurements for samples processed at the given pressures at 1000°C and 240 mins.	134

List of Figures

Figure 2.1 Polyhedral representation of five rare earth sesquioxide polymorphs.....	8
Figure 2.2 Field of phase stability diagram for lanthanide-series sesquioxides	9
Figure 2.3 Phase stability diagrams for R_2O_3 compounds with respect to ionic radii and annealing temperature.	10
Figure 2.4 Polymorphic transformation scheme for RE sesquioxides	12
Figure 2.5 Absolute volume changes for polymorphic RE sesquioxide transitions	14
Figure 2.6 Relative volume changes for sesquioxide and cations upon melting	14
Figure 2.7 Minimum processing pressure and temperature conditions for polymorphic transformation for rare earth sesquioxides.....	15
Figure 2.8: Cubic- Y_2O_3 unit cell structure	19
Figure 2.9 Raman Spectra of Y_2O_3 as pressure is increased from 100kPa (ambient) to 22GPa..	21
Figure 2.10 Transmission performance for various IR-Window material candidates	28
Figure 2.11 Data showing that flexural strength of Y_2O_3 (and ThO_2) is inversely proportional to the square-root of the grain size (Hall-Petch relationship).	30
Figure 4.1 Schematic of DMI HPHT apparatus.....	35
Figure 4.2 HPHT Processing Steps	37
Figure 4.3 Dependence of pressure on loading force for known solid phase transitions at room temperature.	39
Figure 4.4 Dependence of temperature on power required to heat reaction cell.	40
Figure 4.5 FESEM images of same area, showing carbon decoration on a monoclinic- Y_2O_3 grain boundary, taken at 5.0 KV and 2.0 KV.....	49
Figure 5.1 SEM images of fractured samples from 300 μm grain cubic- Y_2O_3 material, and 1.5 μm grain starting material.....	56
Figure 5.2 EDS analysis of as-received 300- μm grain and 1.5 μm grain samples.	57
Figure 5.3 X-ray diffraction spectra of as-received Y_2O_3	58
Figure 5.4 Raman pattern for as-received cubic Y_2O_3	59

Figure 6.1 Characteristic XRD pattern for as-processed monoclinic Y_2O_3 .	61
Figure 6.2 SEM image of monoclinic- Y_2O_3 fracture surface.	62
Figure 6.3 EDS analysis of shear-transformed monoclinic Y_2O_3 .	63
Figure 6.4 TEM diffraction patterns of grains collected from different regions of a transformed monoclinic Y_2O_3 sample, showing presence of polycrystalline and single-crystal grains	65
Figure 6.5 Raman pattern for monoclinic Y_2O_3 .	66
Figure 7.1 XRD patterns for (a) as-received cubic Y_2O_3 (~300 μm GS); (b) forward-transformed monoclinic Y_2O_3 ; and (c) reverse-transformed cubic Y_2O_3 .	70
Figure 7.2 TEM images of coarse-grained (300 μm) material, after reversible transformation to nano-grained c- Y_2O_3 : (a) dark-field image, and (b) lattice image	71
Figure 7.3 SEM images of fracture surfaces: (a) initial coarse-grained Y_2O_3 (300 μm), (b) after forward transformation to m- Y_2O_3 , and (c) after reverse transformation to c- Y_2O_3	72
Figure 7.4 XRD patterns for (a) as-received cubic Y_2O_3 (~1.5 μm GS); (b) forward-transformed monoclinic Y_2O_3 ; and (c) reverse-transformed cubic Y_2O_3 .	74
Figure 7.5 TEM images of fine-grained (1.5 μm) material: (a) after forward transformation to m- Y_2O_3 , and (b) after reverse transformation to c- Y_2O_3	75
Figure 7.6 SEM images of fracture surfaces: (a) initial fine-grained Y_2O_3 (1.5 μm), (b) after forward transformation to m- Y_2O_3 , and (c) after reverse transformation to c- Y_2O_3	76
Figure 7.7 Diagram showing changes in sample dimensions due to a reversible-phase transformation	78
Figure 7.8 Diagram showing changes in sample dimensions due to repeated reversible-phase transformations	78
Figure 7.9 SEM images of fracture surfaces of samples processed at 1.0 and 3.0 GPa/1000°C/240 minutes, showing (a) equiaxed grains at 1.0 GPa in untransformed c- Y_2O_3 , and (b) columnar grains at 3.0 GPa in transformed m- Y_2O_3 .	81
Figure 7.10 SEM image showing the onset of cubic-to-monoclinic conversion at the corners of samples processed at (a) 3.0 GPa/1000°C/15 mins; (b,c) 3.0 GPa/1000°C/60 mins	82
Figure 7.11 XRD spectra for samples processed at 1.0, 2.0, and 3.0 GPa/1000°C/15 min	84

Figure 7.12 SEM images of the fracture surface of a sample processed at 2.5 GPa/1000°C/240 mins, showing a thin surface layer of transformed m-Y ₂ O ₃ phase, and an interior of untransformed c-Y ₂ O ₃ phase.....	85
Figure 7.13 XRD analysis of sample processed at 2.5 GPa/1000°C/240 min: (a) m-Y ₂ O ₃ surface layer; (b) appearance of c-Y ₂ O ₃ at 30-μm depth below the surface; and (c) c-Y ₂ O ₃ at 80-μm depth below the surface.	86
Figure 7.14 SEM images of fine-grained sample after processing at 3.0 GPa/1000°C/15 mins, showing growth of columnar m-Y ₂ O ₃ into untransformed equiaxed-grained c-Y ₂ O ₃	88
Figure 7.15 (a)SEM image of a fine-grained sample, after processing at 3.0 GPa/1000°C/60 mins, showing a progressive change in grain size and morphology with increasing distance from the surface. Columnar-grained m-Y ₂ O ₃ evidently grows at the expense of the initial fine-grained c-Y ₂ O ₃ ,with a clear texturing effect evident via XRD analysis (b).	89
Figure 7.16 SEM images of elongated grains in samples transformed to the monoclinic state at (a) 4.0 GPa/1000°C/ 240 mins; (b) 5.0 GPa/1000°C/240 mins; (c) 6.5 GPa/1000°C/240 mins.	92
Figure 7.17 Optical micrographs of a partially transformed sample, showing decohesion between untransformed-monoclinic core and transformed-cubic shell	101
Figure 7.18 Raman spectra for cubic and monoclinic Y ₂ O ₃	104
Figure 7.19 Line-profile Raman analysis of a sample that had been partially transformed from monoclinic-to-cubic at 1.0 GPa/700°C/240 mins.....	105
Figure 8.1 SEM micrograph of a fractured sample, after forward transformation at 8.0 GPa/1000°C/15 mins and partial reverse transformation at 1.0 GPa/600°C/15 min, showing a lacy-carbon network at intergranular-fractured grains but not at a transgranular-fractured grain.....	110
Figure 8.2 (a) SEM micrograph of an intergranular grain boundary showing patchy decoration with carbon in a coarse-grained (300 μm) sample converted to m-Y ₂ O ₃ and partially transformed back to c-Y ₂ O ₃ , and EDS spectra showing that dark-contrasting regions are carbon-rich and white-contrasting regions are carbon-poor.	111

Figure 8.3 SEM micrographs showing different morphologies of infiltrated carbon	112
Figure 8.4 Carbon-particle decoration of equiaxed grains of c-Y ₂ O ₃ , after processing at 8.0 GPa/1000°C/15 min and then at 1.0 GPa/1000°C/15 min	115
Figure 8.5 Carbon-particle decoration of columnar-grained m-Y ₂ O ₃	116
Figure 8.6 Examples of coarsening at the corners of a reversibly transformed sample.....	117
Figure 8.7 SEM and EDS analysis of a sample after a reversible phase transformation, comparing carbon segregation in regions of: (a) intergranular fracture near the edge of the sample, and (b) transgranular fracture near the midsection of the sample	120
Figure 8.8 (a) SEM image of columnar surface phase for reversibly-transformed sample; (b) Corresponding XRD spectra identifying the thin surface layer as Y ₂ O ₂ CO ₃ phase	121
Figure 8.9 SEM image of equiaxed grains of c-Y ₂ O ₃ , showing the presence of an unknown phase at fractured grain boundaries.	122
Figure 8.10 SEM image of a fine-grained c-Y ₂ O ₃ sample, after processing at 1.0 GPa/1000°C/240 min, showing significant coarsening of the initial equiaxed grain structure.....	124
Figure 8.11(a) SEM image, and (b) XPS spectra for an untransformed c-Y ₂ O ₃ sample that exhibits significant grain coarsening	125
Figure 8.12 SEM image of the corner of a reversibly-transformed c-Y ₂ O ₃ sample, showing a gradient in grain size	126
Figure 9.1 Density and hardness changes in Y ₂ O ₃ due to a reversible-phase transformation. ¹⁰	129
Figure 9.2 Plot of hardness versus reverse transformation processing conditions.	131
Figure 9.3 Plot of density versus reverse transformation processing conditions.....	132
Figure 9.4 Plot of hardness versus processing pressure.....	134
Figure 9.5 Plot of hardness vs. annealing temperature at 8.0 GPa and 240 minutes.	136
Figure 10.1 Effect of pressure on the grain size of sintered TiO ₂ at 400°C/60 min	150
Figure 10.2 Density vs. hot-pressing pressure for Y ₂ O ₃ and Y ₂ O ₃ -MgO composites	151
Figure A.1 Density vs. hot-pressing pressure for Y ₂ O ₃ and Y ₂ O ₃ -MgO composites	154
Figure A.2 SEM image of a powdered Y ₂ O ₃ sample completely transformed to the monoclinic phase at 8.0 GPa and 1000°C for 15 mins.	155

1 INTRODUCTION

Phase-pure cubic- Y_2O_3 is an attractive candidate material for mid-range IR transmission applications and as a potential replacement for single crystal Al_2O_3 (sapphire) in IR windows and domes for hypersonic flight applications. The thermo-mechanical properties of cubic Y_2O_3 make it suitable for use in some IR window and dome applications, but its mechanical properties, particularly hardness and toughness, must be improved to better meet the requirements of the most demanding applications.¹ To meet this goal, methods to fabricate *nanocrystalline cubic- Y_2O_3* have been investigated, in anticipation that this will yield significant improvements in hardness, strength, and toughness. Moreover, reducing the grain size of cubic- Y_2O_3 to ~ 100 nm should maintain high optical transparency over the wavelength range of interest.

Preliminary work on the sintering of nanostructured Y_2O_3 powders produced by flame- and plasma-synthesis methods has shown that complete densification is achievable, but that grain growth cannot be avoided without added sintering aids or inhibitors^{2,3}. When densification of these materials exceeds about 90% of the theoretical value, remaining nanopores are present in sufficient numbers to oppose grain boundary migration. However, when these start to disappear, the resulting high grain boundary surface area promotes rapid grain coarsening, often generating a microcrystalline structure.

To circumvent this problem, alternative methods to fabricate fully dense nanocrystalline Y_2O_3 have been investigated. This led to the unexpected

discovery of a reversible-phase transformation (RPT) process through which fully dense polycrystalline Y_2O_3 can be transformed directly into the nanocrystalline state.

RPT processing draws from *Transformation Assisted Consolidation* methods⁴, which can be used to control the grain size of nanocrystalline TiO_2 and Al_2O_3 during consolidation and sintering. Transformation Assisted Consolidation involves high pressure/low temperature (HPLT) processing, and has been shown to produce nano-scale grain structures from metastable polymorphs, such as anatase TiO_2 and $\gamma\text{-Al}_2\text{O}_3$.^{5,6,7,8,9}

A key factor in RPT processing is the design of a pressure cell that is capable of processing millimeter-sized samples suitable for properties evaluations. Given the high pressures used, scalability of the pressure cell is challenging.

Although feasibility of RPT processing has been demonstrated, much work was necessary before the finest possible nano-scale grains could be obtained. Hence, the primary objective of this research is to better understand and optimize the RPT processing method. Once this objective was achieved, the dependence of hardness and toughness on grain size, extending from nano- to micro-scale dimensions, could be determined. This work validates the applicability of the Hall-Petch relationship to c- Y_2O_3 , over a grain-size range hitherto inaccessible. A secondary objective is to investigate and better understand the underlying Y_2O_3 phase transformations and to control an

unexpected *surface modification* effect. As will be shown, the latter is due to interaction between the Y_2O_3 samples and its encapsulating graphite heater during high pressure/high temperature (HPHT) processing.

In its most striking form, complete conversion of fine-grained polycrystalline cubic Y_2O_3 into monoclinic Y_2O_3 with a coarse-grained columnar structure occurs, possibly involving intermediate or additional phases. With the effect more fully understood and controlled, attention was re-focused on RPT processing, with the objective of achieving grain sizes as small as 5-10 nm. Reliable data on mechanical properties of c- Y_2O_3 in the nanometer range was obtained.

Concurrently and independently, Raytheon IDS has been developing Y_2O_3 -base compositions for mid-IR dome applications. Much of this work is proprietary, but it is known that significant progress has been made in the processing of Y_2O_3 /MgO nanocomposites, starting with flame-synthesized nanopowders and using sinter-HIP for consolidation purposes.

A major advantage of working with a two-phase ceramic is that it enables fabrication of a nanocomposite structure, without significant grain coarsening, as discussed in a previous Rutgers' publication¹⁰. This is because the two phases, particularly when their volume fractions are comparable, tend to form bicontinuous or interpenetrating structures that are remarkably resistant to coarsening at high temperatures. One important consequence of this grain-coarsening resistance is that the material displays high-strain-rate

superplasticity¹¹. The effect has been shown to be due to enhanced grain boundary sliding in the nano-grained composite, as would be expected.

So far, Raytheon has been able to fabricate a prototype $\text{Y}_2\text{O}_3/\text{MgO}$ window with grain size ~ 100 nm, while satisfying both optical and mechanical performance requirements. On-going work at Raytheon has impacted research at Rutgers' Center for Nanomaterials Research (CNR) in several ways. First, Raytheon has provided high quality polycrystalline Y_2O_3 samples for RPT processing. Second, they have agreed to perform optical transmission measurements on *highly polished* samples on an as-needed basis. Third, they have provided technical information not readily available in the literature.

2 BACKGROUND

In what follows, a survey of relevant literature is presented, examining:

- Rare earth sesquioxide polymorphs
- High-temperature polymorphs
- R_2O_3 crystallographic structures
- Fields of polymorph stability
- Pressure-assisted phase transformations
- Y_2O_3 polymorphs
- Optical and mechanical performance of Y_2O_3

2.1 Rare Earth Sesquioxide Polymorphs

It is well established that rare earth sesquioxides (R_2O_3) can exist in 3 forms: A, B, and C-type. C-type refers to the cubic $Ia\bar{3}$ space group form, which is commonly stable at room temperature and atmospheric pressure; B-type describes the higher-pressure monoclinic phase with $C2/m$ space group; and A-type describes the highest-pressure hexagonal phase with $P\bar{3}m1$ space group.¹²

Most rare earth sesquioxides can only crystallize in the cubic form at low pressures and temperatures, independent of preparation methods, with the exception of nanopowder synthesis¹³. Some, such as neodymium oxide, can form either cubic or monoclinic structures, depending on decomposition and preparation methods.¹⁴

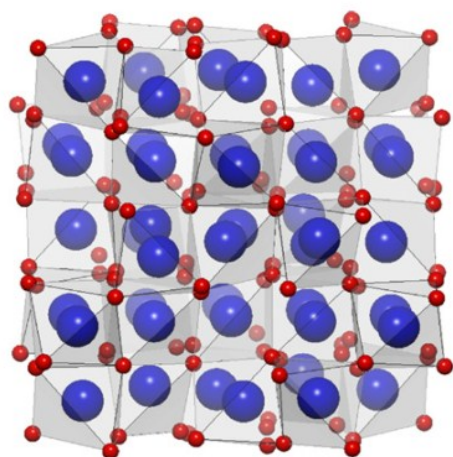
Although yttrium is a transition metal and not a lanthanide-series element, its electronegativity and ionic radius are chemically close to those of the lanthanide-series elements, most notably dysprosium and holmium. Cubic- Y_2O_3 also exhibits a similar structure to the cubic R_2O_3 structure (R=lanthanide series rare earths Sm-Lu) at ambient temperature and pressure, suggesting it should share similar high-pressure and high-temperature modifications.¹⁵

2.2 High-Temperature Polymorphs

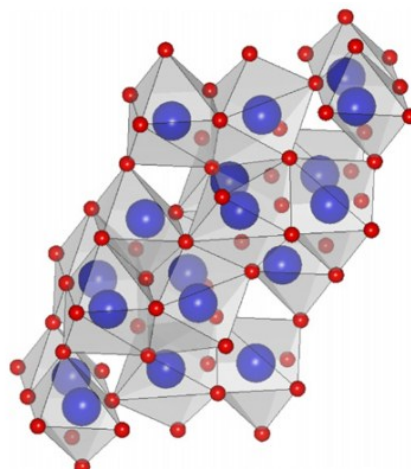
In addition to the three high-pressure R_2O_3 polymorphs, rare earth sesquioxides can form H- (hexagonal) or X- (cubic) type crystalline structures when heated close to their melting temperature.¹⁶ At high temperatures, cubic, monoclinic, and high-pressure hexagonal R_2O_3 structures transform into H-type high-temperature hexagonal structures, with the exception of Lu and Sc sesquioxides, which convert straight to the X-type high-temperature cubic phase. Certain H-type structures, R=La-Dy, can be further transformed to the X- R_2O_3 forms¹⁴.

2.3 R_2O_3 Crystallographic Structures

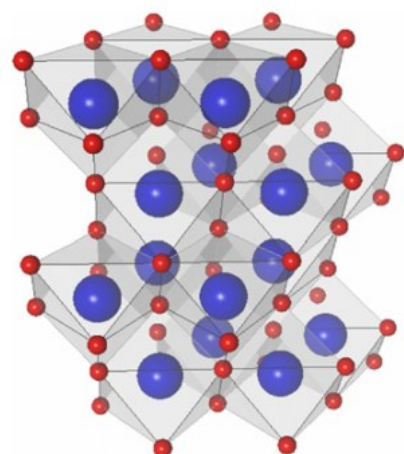
Figure 2.1 depicts polyhedral representations that apply to rare-earth sesquioxides R_2O_3 , where R = lanthanide series elements, yttrium, or scandium. The large spheres and small spheres represent R cations and O anions, respectively. The cubic- R_2O_3 structure (I) demonstrates cations in 6-fold symmetry. Some cations will be surrounded by seven oxygen anions in the monoclinic - R_2O_3 structure (II), and all cations will be in 7-fold coordination in the hexagonal phase (III). High-temperature hexagonal (IV) and cubic (V) phases are also shown.



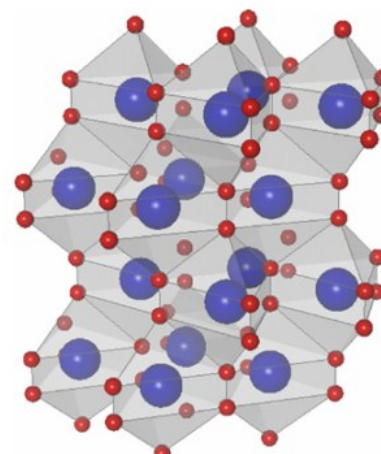
I) C-Type (cubic)



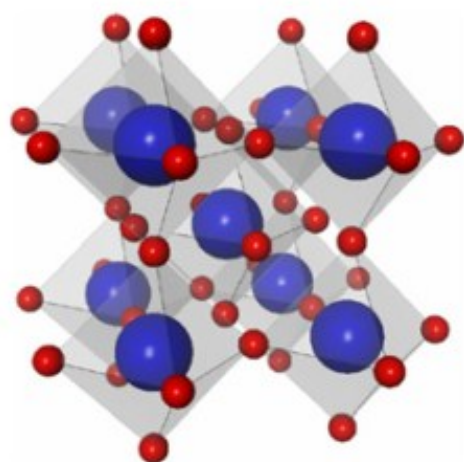
II) B-Type (monoclinic)



III) A-Type (hexagonal)



IV) H-Type (high-temperature hexagonal)



V) X-Type (high-temperature cubic)

Figure 2.1 Polyhedral representation of five rare earth sesquioxide polymorphs.¹⁴

2.4 Fields of Polymorph Stability

It has long been recognized that rare earth sesquioxide polymorph stability, under ambient pressure condition, is dependent on cation size. The melting temperature for the R_2O_3 oxides follows the same dependency. An early diagram, Figure 2.2, depicts the fields of stability with respect to ionic radius and temperature for A-, B-, and C-type phases. Coupled with the known differences in phase densities, it was also noted that the transformation temperature for cubic-to-monoclinic and monoclinic-to-hexagonal could be reduced by the application of high pressure.¹⁷

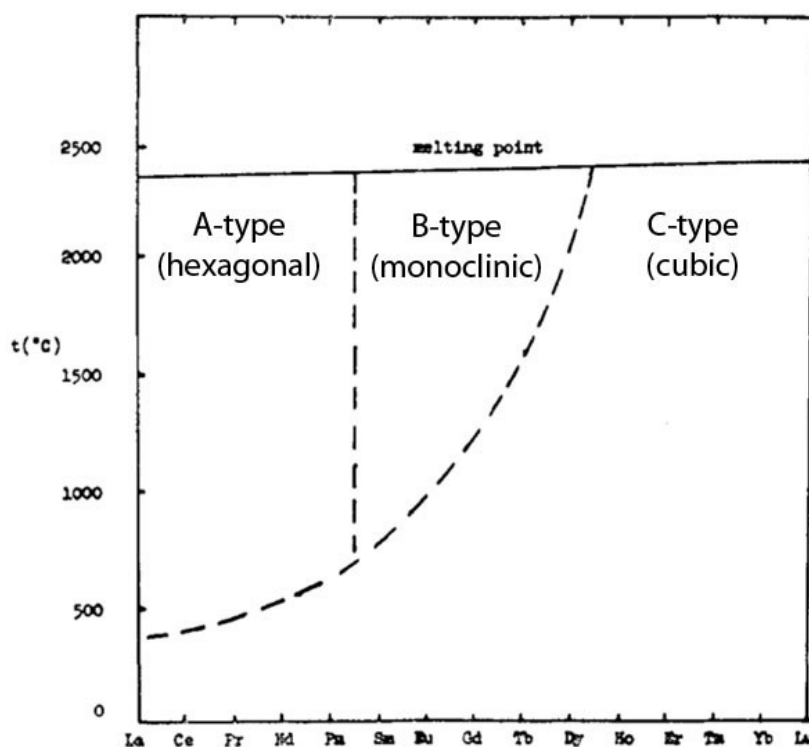


Figure 2.2 Field of phase stability diagram for lanthanide-series sesquioxides.¹⁷

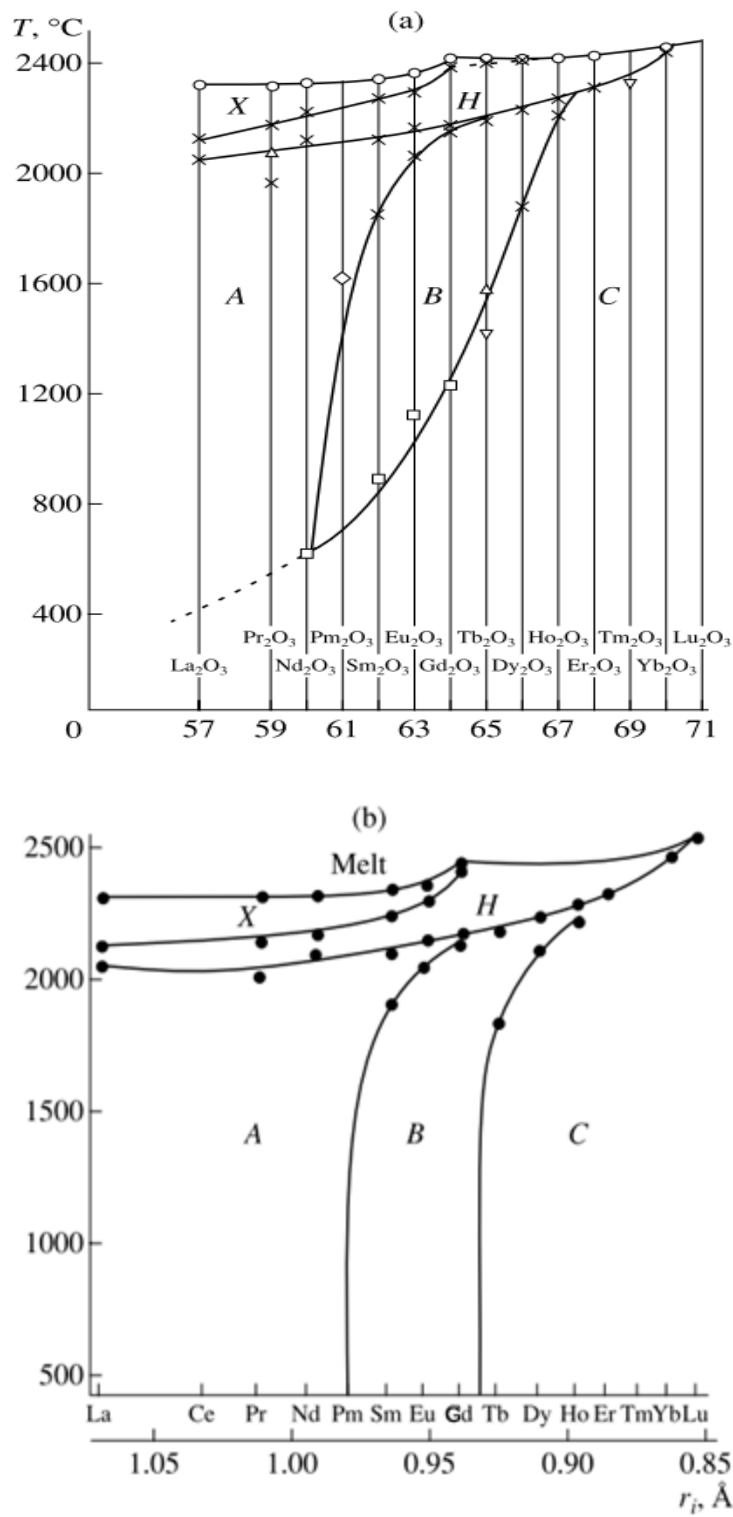


Figure 2.3 Phase stability diagrams for R_2O_3 compounds with respect to ionic radii and annealing temperature.¹⁸

A more thoroughly developed phase stability diagram¹⁹, Figure 2.3a, was compiled from several sources,^{20,21} and then modified to reflect new data. The modified phase stability diagram, Figure 2.3b, does not allow for any metastable phases dependent on ionic radius R^{3+} at lower temperatures²². Both diagrams reflect the three high-pressure polymorphs and two additional high-temperature modifications, H-type (hexagonal) and X-type (cubic).

The second model is considered to more accurately represent the stable polymorphic phases at ambient pressure, since it interprets the existence of cubic phase at low temperatures to be non-equilibrium and describes the possible stabilization of unstable modifications by crystalline impurities¹⁸. The thermodynamic function would then be a smooth function of ionic radius, r , and the curve separating the regions of thermodynamic stability of the phases should be a vertical tangent that approaches absolute zero¹⁸.

A further revised lanthanide sesquioxide polymorphic transformation scheme is presented in Figure 2.4. Various symbols represent experimental values as collected from reported literature, and the effective ionic radii are calculated for trivalent cations in six-fold coordination²³. With an ionic radii of 104 pm, yttrium would be placed on the horizontal axis between erbium (103 pm) and holmium (104.1 pm).

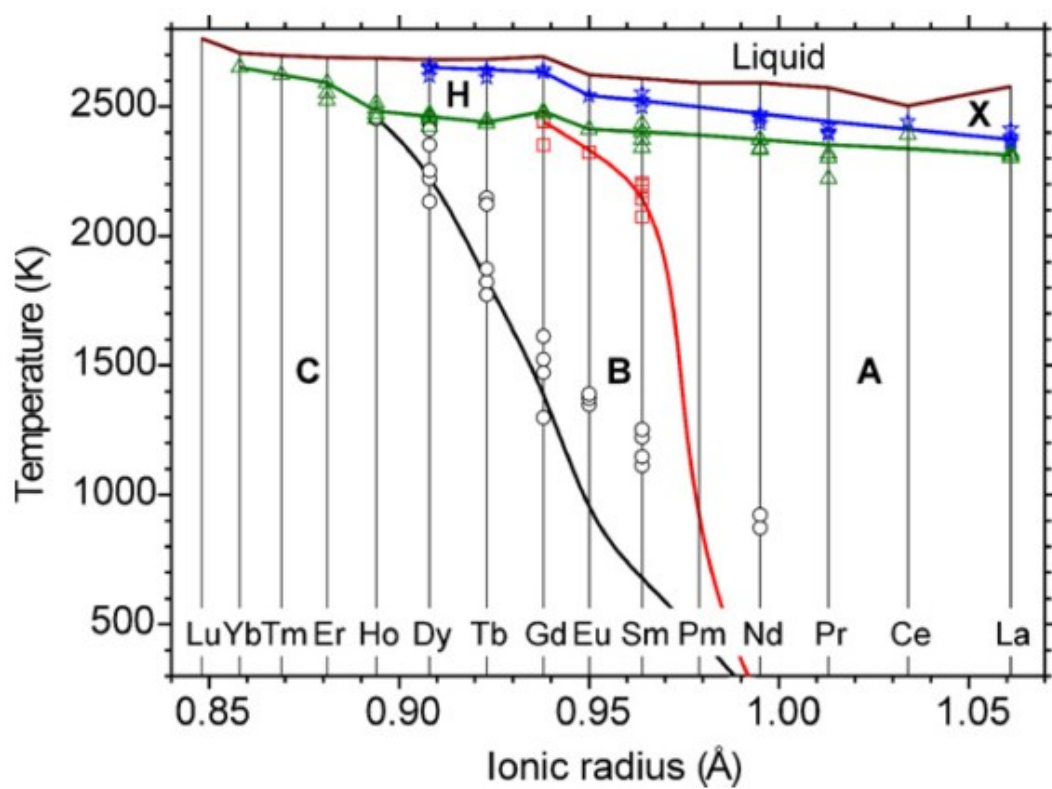


Figure 2.4 Polymorphic transformation scheme for RE sesquioxides.¹⁴

2.5 Pressure-Assisted R_2O_3 Transformations

It has been shown that, in order to achieve controlled polymorphic transformations in lanthanide-series R_2O_3 compounds, the application of pressure is necessary in cases where the critical transformation temperature exceeds the compounds' melting temperature. There is a distinct linear relationship between critical pressure and temperature values that is common for most rare earth sesquioxide compounds. It is also apparent that the thermodynamic threshold increases as ionic radii decrease.

Since the $C \Rightarrow B \Rightarrow A$ (cubic-to-monoclinic-to-hexagonal) polymorphic phase transitions are always accompanied by a *decrease in volume*, the application of high pressure increases the stability of the B-type structure with respect to the C-type structure, and A-type compared to the B-type structure. Supporting this, it has been shown that such $C \Rightarrow B \Rightarrow A$ transitions can occur at room temperature under high-pressure loading^{15,17,24,25,26,27,28,29}, and significant shock compression^{30,31,32}.

The absolute values of volume change for $C \Rightarrow B$ (square markers) and $B \Rightarrow A$ (circle markers) transformations are shown in Figure 2.5. Figure 2.6 shows the relative molar volume change of RE sesquioxides and the metal cations upon melting.

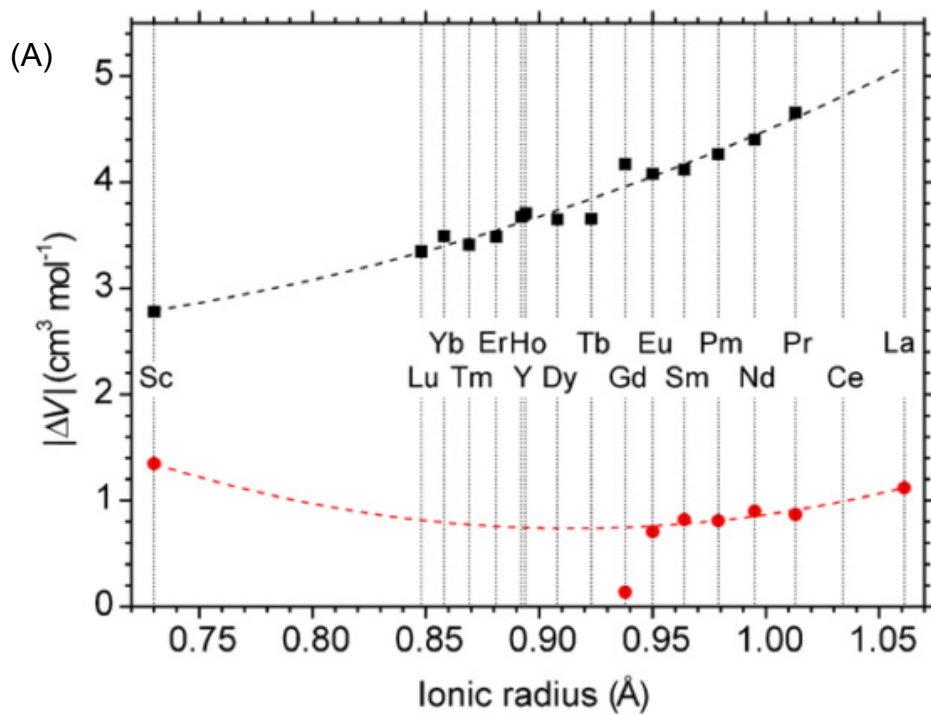


Figure 2.5 Absolute volume changes for polymorphic RE sesquioxide transitions.

14

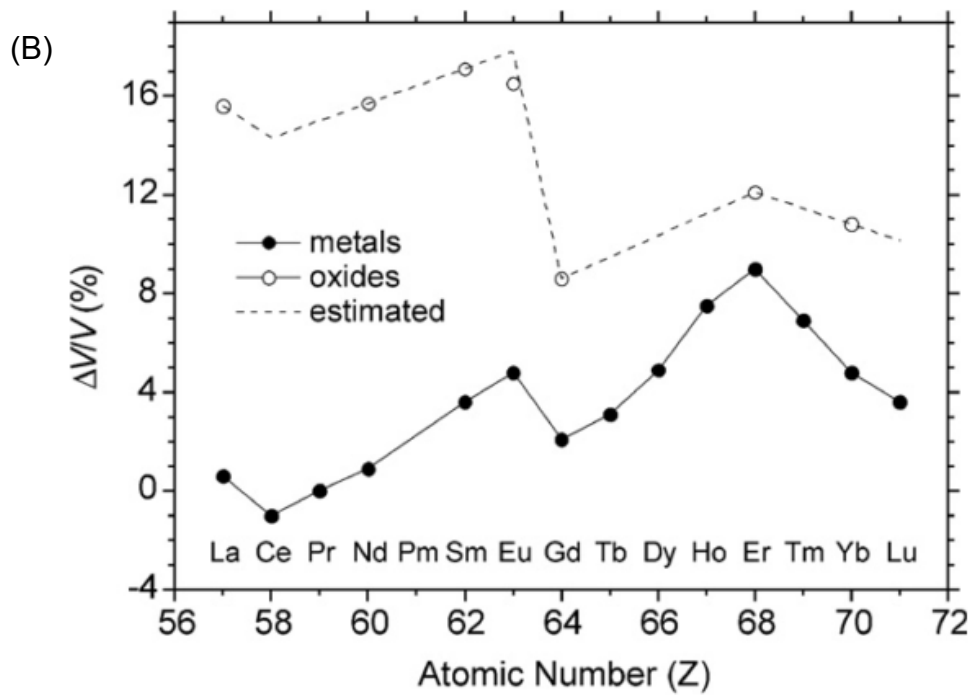


Figure 2.6 Relative volume changes for sesquioxide and cations upon melting.¹⁴

Equations (2.1) and (2.2) can be used to calculate the transition temperature as a function of pressure, and transition pressure as a function of temperature. The linear trend for the reversible phase transitions, Figure 2.7, confirms that the transition pressure and temperature are co-dependent. In the absence of calorimetric data, the critical processing pressure or annealing temperature necessary for the cubic-to-monoclinic transition to occur can be predicted by interpolation if the other value is fixed.

$$T_{transition} = \frac{\Delta H^\circ}{\Delta S^\circ} + \frac{\Delta V}{\Delta S^\circ} P \quad (2.1)$$

$$P_{transition} = \frac{\Delta H^\circ}{\Delta V} + \frac{\Delta S^\circ}{\Delta V} T \quad (2.2)$$

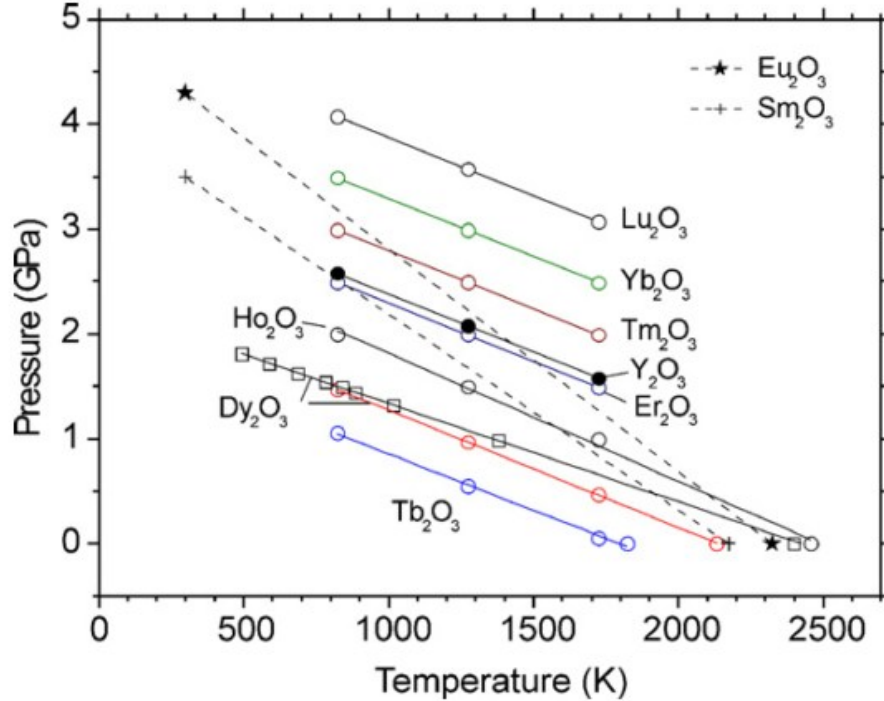


Figure 2.7 Minimum processing pressure and temperature conditions for polymorphic transformation for rare earth sesquioxides.¹⁴

Prior to 1964, rare earth sesquioxide phase transition studies were conducted using only high temperature processing. It was believed that the C-type to B-type transformations could only be achieved at temperatures higher than the melting points of most RE sesquioxides, with the B-type form theoretically being metastable at atmospheric pressure. Rare earth sesquioxides with smaller ionic radii, such as yttrium, erbium and ytterbium oxides, were thought to exist only in the C-type polymorph, since no transformations were observed below 2400°C.²⁰

Hoekstra³³ suggested that, given the decrease in volume when rare earth sesquioxides transform from C-type to a B or A-type phase, the higher density forms should be more favorable at higher temperatures. Since the transitions were thought to be of the reconstructive type, Hoekstra also suggested that high-pressure forms could potentially be retained if quickly quenched from processing to ambient conditions. Thus, it was considered possible to *convert the cubic forms of smaller ionic-radii rare earth oxides to the monoclinic and hexagonal forms* using a combination of high pressure and high temperature processing.

In Hoekstra's study, the first to report combined high-temperature and high-pressure (HPHT) processing methods, RE sesquioxide samples were first annealed in air at 1000°C to remove any absorbed H₂O or CO₂. A tetrahedral anvil apparatus was used to apply high pressure, with the pressure calibrated to Bi-I, Bi-II, and Yb transformations.

Samples were placed in platinum envelopes and then pressed into pellets. These pellets were separated with pyrophyllite spacers before being placed in a pyrophyllite tube. A graphite heater was fitted to the tube, which was placed in a pyrophyllite tetrahedron to be used for high pressure application.

The samples were heated slowly over a period of 30 minutes. Once processing was complete, the samples were rapidly quenched to 50°C by turning off power to the graphite heater. Pressure was then released gradually over a 5-10 minute period. Table 2-1 shows the critical processing parameters for successful cubic-to-monoclinic transformation for a number of materials. Hoekstra used X-ray diffraction to confirm that a cubic-to-monoclinic transition took place, and to zero-in on the critical processing conditions.

Table 2-1 Pressure and temperature conditions used in synthesis of B-type sesquioxides.³³

Sesquioxide	Pressure (GPa)	Temp (°C)
Yttrium	2.5	1000
Samarium	3.0	1020
Europium	2.5	905
Gadolinium	3.0	1020
Terbium	2.5	905
Dysprosium	3.0	1020
Holmium	2.5	1000
Erbium	3.0	1020
Thulium	4.0	1005
Ytterbium	4.0	1000
Lutetium	4.0	1005

Hoekstra also observed that, contrary to previous theories, *the cubic-to-monoclinic transformations were in some cases reversible and thus enantiotropic*. The transformations were shown to be reversible by heating the transformed monoclinic product in air to 1000°C at atmospheric pressure. All of the studied compositions, with the exception of europium and gadolinium oxides, reverted back to the cubic C-type form.³³

Most following studies turned to focus on the application of high pressure to drive the cubic-to-monoclinic conversion, using diamond anvil cells for the application of pressure. It was shown that the cubic-to-monoclinic transformation in Y_2O_3 requires about 13 GPa of pressure at 18°C and the monoclinic to hexagonal about 24.5 GPa.³⁴

Another study³⁵ showed that, for a range of RE sesquioxides, the cubic-to-monoclinic transformation required 12-20 GPa of pressure at a temperature of 700 °C. This was built upon by Husson et al ³⁶, who focused on the high pressure transformation of Y_2O_3 at ambient temperature.

There have been reports³⁷ of a size-dependent amorphization effect for nano- and sub-micro-scale c- Y_2O_3 under high pressure, suggesting that bulk R_2O_3 materials might behave differently than the powdered materials often discussed in literature.

2.6 Y_2O_3 Polymorphs

2.6.1 Cubic Y_2O_3 Structure

The cubic- Y_2O_3 unit cell is composed of 32 yttrium and 48 oxygen ions, which can be more easily visualized in the form of 64 minicubes, Figure 2.8. In this structure, yttrium atoms populate the center position of every other minicube. Each yttrium atom is surrounded by 6 oxygen atoms, with two out of eight cube corner positions vacant. Half of the minicubes in a unit cell are missing two oxygen atoms at the ends of face diagonals, with the other half missing two oxygen atoms at the ends of body diagonals. Actual atomic positions deviate due to oxygen vacancies, with each yttrium atom occupying a strong distorted octahedral configuration.³⁸

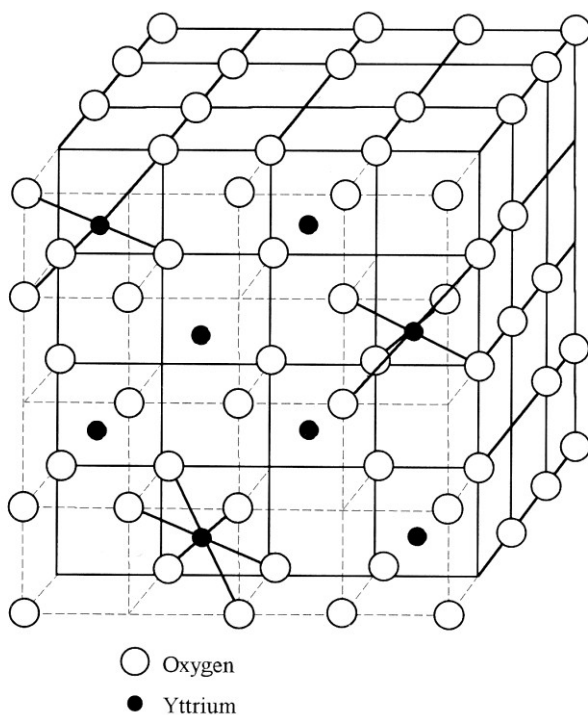


Figure 2.8: Cubic- Y_2O_3 unit cell structure.³⁸

The cubic- Y_2O_3 unit cell is therefore a defect structure with oxygen vacancies and open lattice sites. Under high temperature or high pressure conditions, the cubic crystal cell will be compressed, shortening the Y-O bond length. If the applied temperature or pressure is sufficiently increased, the cubic structure will lose stability, and the atoms will rearrange to form a higher density phase. As will be shown, this can occur by nucleation and growth or by a displacive (shear) transformation.

2.6.2 Y_2O_3 Phase transitions

Husson used a diamond anvil cell, with KBr as the pressure-transmitting medium, to process a 50 μm diameter single-crystal Y_2O_3 sample. Ruby chips used to measure the applied pressure, and Raman spectra were recorded as the pressure was increased from atmospheric pressure to 22GPa (Figure 2.9).¹⁵

Husson reported that their Raman data showed a significant hysteresis in the pressure cycle, suggesting that the cubic-to-monoclinic phase transformation mechanism is a displacive type. Under high pressure, the cubic Y_2O_3 crystal is compressed, with the Y-O bond length shortening and leading to increased covalency. The Y-O bond force constant increases by about 20%, Y-O-Y by about 25%, and O-Y-O by about 7%.

In light of not having observed a monoclinic-to-cubic transformation, Husson's group concluded that the cubic-to-monoclinic transformation is non-reversible. However, while in agreement with earlier work, more recent

studies^{33,39} have supported that the monoclinic-to-cubic transformation is achievable in Y_2O_3 and other RE sesquioxides.

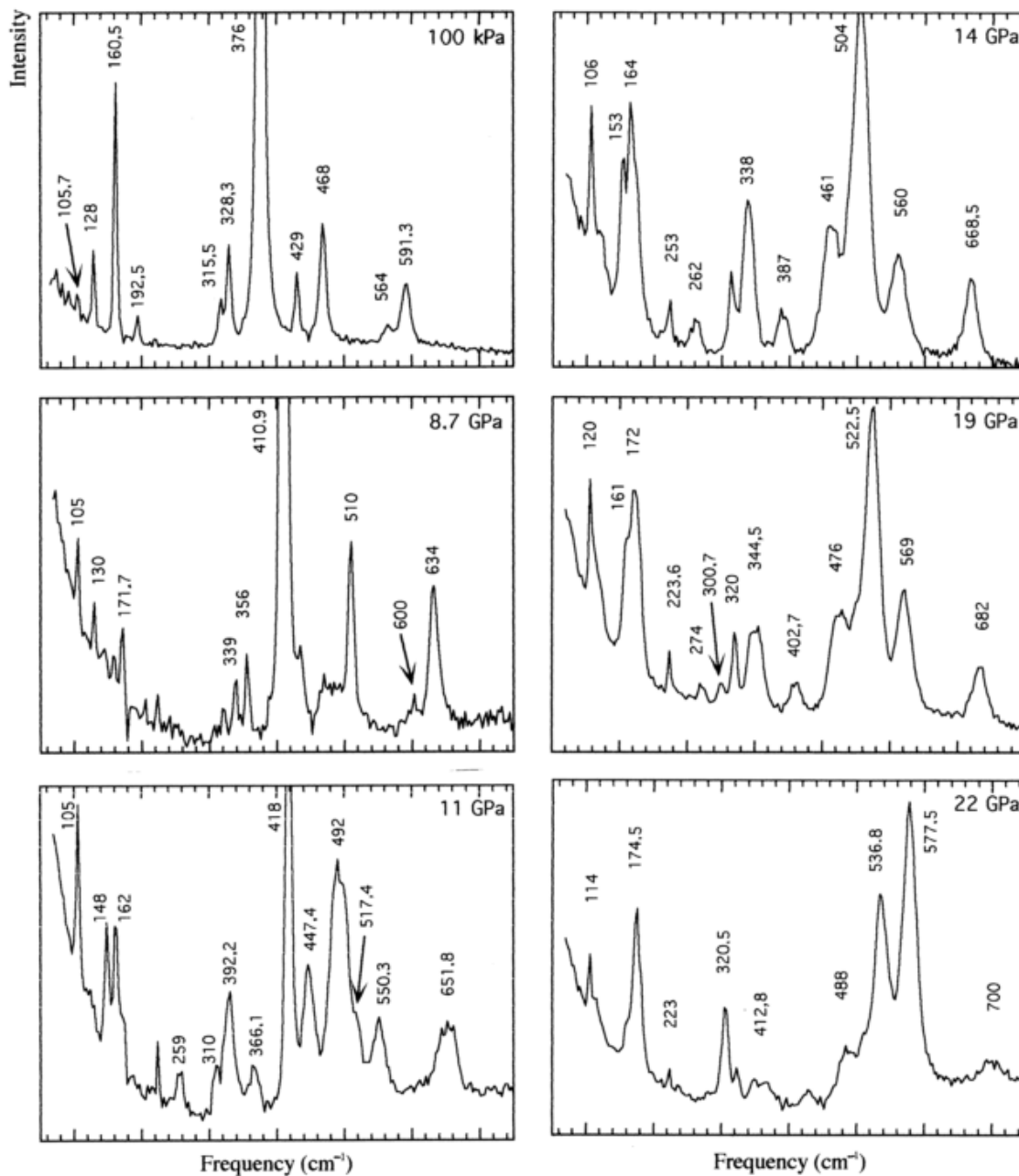


Figure 2.9 Raman Spectra of Y_2O_3 as pressure is increased from 100kPa (ambient) to 22GPa.¹⁵

Table 2-2 (adapted from Zinkevich), summarizes the reported polymorphic transition pressures for Y_2O_3 . Pressure-assisted transformations were accomplished using diamond anvil cells.

Table 2-2 Critical parameters for pressure-assisted Y_2O_3 transformations.

Transition	Temperature ($^{\circ}C$)	Pressure (GPa)	Reference
$C \Rightarrow B$	1000	2.1	Hoekstra ⁴⁰
$C \Rightarrow B$	25	12	Atou ³¹
$C \Rightarrow B$	25	10 \pm 2	Husson ¹⁵
$C \Rightarrow B$	25	12.8	Ma ³⁰
$B \Rightarrow A$	25	19 \pm 2	Husson ¹⁵
$B \Rightarrow A$	25	21.8	Ma ³⁰

Although most studies report observations of the cubic-to-monoclinic and monoclinic-to-hexagonal transformations, one group reported observing the onset of direct cubic-to-hexagonal Y_2O_3 transformation at 12.1 GPa, and complete conversion at 22.5 GPa. Wang et al. have concluded that the hexagonal form is not quenchable, but can be modified to the monoclinic form upon decompression. They point out the benefit of *in situ* characterization, which is not utilized in studies that explore the shock-induced phase transformation of rare earth sesquioxides.⁴¹ Other groups utilizing *in situ* characterization methods have observed a similar direct cubic-to-hexagonal transformation in other rare earth oxides, such as Sm_2O_3 ⁴², Gd_2O_3 ⁴³. One study noted evidence of a cubic to partial amorphous transition in Eu_2O_3 at high pressure that developed into the

hexagonal phase upon release of pressure.⁴⁴ Another study described a similar cubic-to-hexagonal transformation in Dy_2O_3 ⁴⁵. Wang et al. added that the cubic-to-monoclinic Y_2O_3 transformation is irreversible, contrary to what has been presented and corroborated by a number of other studies.

To summarize, Y_2O_3 is a sesquioxide of the rare earth (RE) R_2O_3 -type, and exists in three known polymorphs: cubic (Ia3), monoclinic (C2/m), and hexagonal (P3m1). Under standard pressure and temperature conditions, Y_2O_3 is only found in the cubic form. Under high-pressure processing using a diamond-anvil pressure cell, it has been observed that cubic- Y_2O_3 powder transforms into monoclinic- Y_2O_3 at pressures >13 GPa³⁴. However, samples obtained using this technique are too small for mechanical properties measurements. Using a high pressure/high temperature (HPHT) press, available at Diamond Materials Inc. (DMI), mm-sized samples have been fabricated, at pressures of 1.0-8.0 GPa. In this project, full use is made of this capability, enabling properties data for c- Y_2O_3 and m- Y_2O_3 in both micro- and nano-grained forms to be obtained for the first time.

The molar volume of Y_2O_3 is $44.804 \text{ cm}^3 \text{ mol}^{-1}$ (C-type), $41.132 \text{ cm}^3 \text{ mol}^{-1}$ (B-type), $40.385 \text{ cm}^3 \text{ mol}^{-1}$ (A-type, interpolated). Density is 5.03 g/cm^3 for the cubic phase, 5.35 g/cm^3 for the monoclinic phase.

2.6.3 High-Temperature Phase

The transition from C-type to high-temperature H-type structure occurs at about 2300°C for Y_2O_3 ¹⁸. A shift in lattice parameter from $a=10.604 \text{ \AA}$ ⁴⁶ for the cubic form to $a=3.81 \text{ \AA}$ and $c=6.08 \text{ \AA}$ for the high-temperature hexagonal form has been reported. In another study, the resulting x-ray diffraction pattern, lattice parameter shift ($a=5.264 \text{ \AA}$), and space group determination (Fm3m or Fm3) indicate a fluorite-type structure with one out of four oxygen sites being vacant.⁴⁷ The exact transition temperature has not yet been finalized, as several groups observed experimental transitions ranging from 2220°C to 2430°C^{18,48,49,50,51,52,53,54}. The observation that the transformation is from a low-temperature cubic form to a high-temperature fluorite-type cubic form is corroborated in several studies⁵⁵, but contested in others. Zinkevich analyzed the reported values and recommended $2327 \pm 30^\circ\text{C}$ for the reversible $\text{C} \rightleftharpoons \text{H}$ phase transition temperature. Several reported values are in good agreement⁵⁶, with differences potentially due to overheating and undercooling effects.

Some studies agree that Y_2O_3 forms the high-temperature hexagonal structure prior to melting⁵⁷, which is said to occur at 2439°C ^{58,59}, and undergoes a molar volume change of 11.2% upon fusion. DTA analysis differs slightly, showing that the cubic to fluorite-like structure forms at $2308 \pm 15^\circ\text{C}$ before melting at $2382 \pm 15^\circ\text{C}$ ⁶⁰.

Several studies are in conflict with each other, as the high-temperature Y_2O_3 phase is reported as both hexagonal and cubic. Supported by the scheme

of polymorphic stability, it is not ruled out that the hexagonal phase may form under one set of conditions and a fluorite-like cubic form under other conditions. The cubic fluorite form is logical as a high-temperature phase as it can be related to the low-temperature cubic form, but with added disordering of oxygen vacancies.⁶⁰

2.6.4 Monoclinic Y_2O_3 Synthesis

Although cubic Y_2O_3 is the most common form of Y_2O_3 , monoclinic Y_2O_3 can be successfully produced in a laboratory setting without turning to the high-pressure processing methods previously discussed. Several studies detail the synthesis of phase-pure monoclinic Y_2O_3 and other RE sesquioxide particles by flame aerosol methods^{61,62}. Although such methods produce materials of both cubic and monoclinic Y_2O_3 forms, a particle-size effect¹³ is exploited to exclude cubic-structured particles from the final product. It was found that 1.5 μm is the critical particle size where there is a 50% chance for a particle produced by flame synthesis to be cubic or monoclinic. Particles much smaller than 1.5 μm were often monoclinic-structured, and larger particles were of the cubic form⁶³, in agreement with the Gibbs-Thomson effect. It was theorized and then proved practical that an impactor could be utilized in flame spray pyrolysis to segregate phase-pure materials where a particle size-dependent crystal structure exists, by limiting droplet volumes to control maximum particle size of synthesized materials.⁶⁴ Even so, while this potentially allows for the greater study of phase-pure monoclinic Y_2O_3 , there is no means by which bulk monoclinic materials can be produced with such powders.

2.7 Cubic Y_2O_3 Window and Dome Fabrication

Cubic Y_2O_3 window and dome fabrication begins with 99.99%-purity Y_2O_3 powder with a particle size of 1-3 μm . The powder is mixed with methanol and milled with cubic Y_2O_3 as the grinding media before being passed through a 400-mesh sieve to produce 1-2 μm diameter particles. The powder is mixed with an organic binder and dispersant before being passed through an ultrasonic horn and then a spray dryer to remove solvent. Cold isostatic pressing compacts and consolidates the powder into a green body which is then sintered at 1700-1900°C. A Y_2O_3 enclosure is used to minimize the stoichiometric variations that would otherwise result from sintering in a tungsten or graphite furnace. Hot isostatic pressing (HIP) is performed at 1700-1900°C and 180MPa in an argon gas environment for final densification. Annealing in air at 1450-1800°C is necessary to restore the slightly oxygen-deficient stoichiometry before it can be polished to produce the final product.⁶⁶

2.8 Cubic Y_2O_3 Optical and Mechanical Performance

Infrared window and dome materials are designed to protect thermal imaging equipment against damaging conditions. The suitability of materials for these applications is based on three primary criteria: strength and fracture toughness, thermal shock resistivity, and infrared transmission efficiency.⁶⁵

Single-crystal cubic-structured materials are often favored for IR-window and dome applications over non-cubic materials, to avoid birefringence as light is transmitted through the material. Non-cubic polycrystalline materials are also more prone to severe scattering as the index of refraction may depend on crystallographic orientations. Polycrystalline cubic materials are desirable if measures are taken to reduce grain boundary contamination and internal stress that may promote birefringence or scattering.⁶⁶

Sapphire, ALON and spinel are the most commonly used materials for mid-range IR applications, Figure 2.10. Cubic Y_2O_3 was first considered for mid-range IR applications in the 1980's because it has excellent transmission over the 5-8 μm range. Such transmittance is desirable since it extends the usable bandwidth available for optical windows and domes. However, at that time, polycrystalline Y_2O_3 samples produced using conventional sintering methods were less durable due to lower hardness, flexural strength and fracture toughness compared to other mid-wave IR window materials, Table 2-3.¹

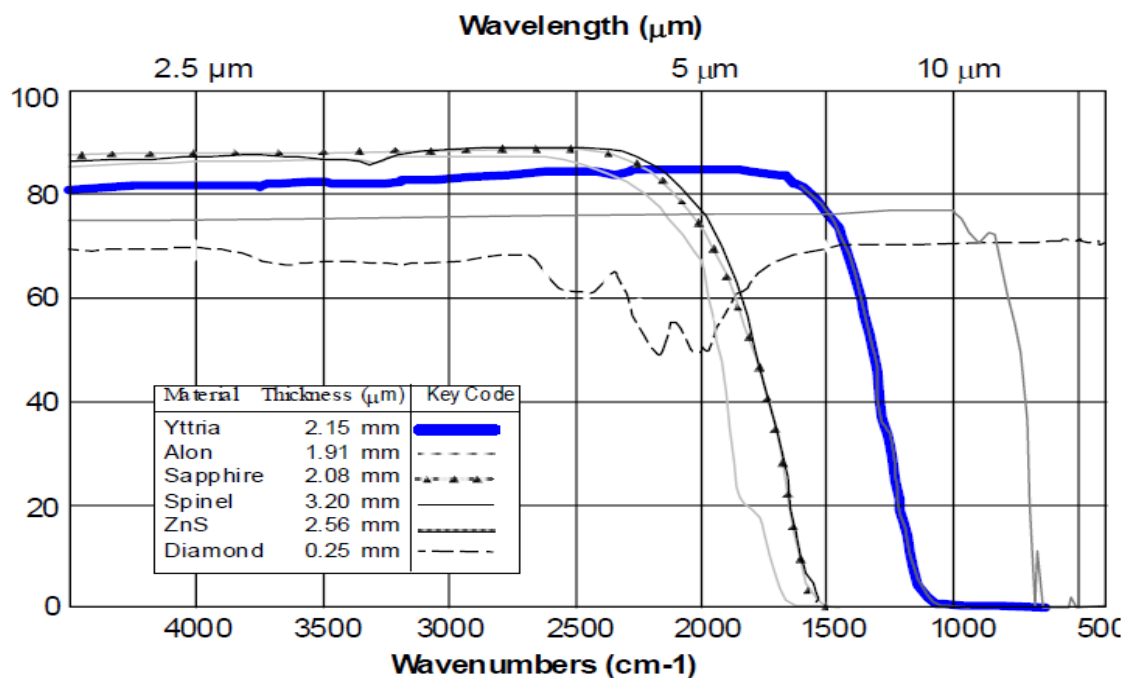


Figure 2.10 Transmission performance for various IR-Window material candidates (Raytheon) ¹

Table 2-3 Physical and mechanical properties of several IR window materials. ¹

Property	Units	ALON	Sapphire	Spinel	PSZ	Yttria
Refractive Index		1.75	1.75	1.75	2.15	1.95
IR Cut-off ($\beta=1\text{cm}^{-1}$)	(μm)	4.6	5.0	5.3	6.0	7.0
Flexural Strength	(MPa)	300	400	190	1400	160
Fracture Toughness	(MPa·m ^{1/2})	1.4	2.0	1.9	~5	0.7
Young's Modulus	(GPa)	88	340	131	180	70
Hardness	(GPa)	18.0	22.0	16.0	13.0	7.1
Thermal Conductivity	(W/m·K)	13	36	15	3	14
Thermal Expansion	(ppm/K)	5.8	5.3	5.6	9.0	6.6
Poisson's Ratio		0.24	0.27	0.26	0.30	0.30

Flexural strength data for Y_2O_3 and ThO_2 , Figure 2.11, shows that reducing the grain size of Y_2O_3 from 100 to 10 μm yields an approximate two-fold increase in flexural strength, with similar result also shown for ThO_2 . In both cases the data appears to obey a Hall-Petch relationship (Eq 2.1⁶⁷), in that the flexural strength (σ_y) is inversely proportional to the square-root of the grain size (d). σ_0 and k_y are constants. The plateau in strength displayed by ThO_2 for grain sizes $<10 \mu m$ is not understood. However, it is well known that residual micro-porosity, a possible contributing factor, adversely affects mechanical strength of ceramics. In general, fine-scale particles are susceptible to aggregation, with conventional sintering processing methods often resulting in isolated micro-pores that are located at the initial points of contact of the nanoparticle aggregates. Present work yields data on mechanical properties of fully dense c- Y_2O_3 over a hitherto inaccessible submicron-size range extending to nanoscale dimensions.

$$\sigma_y = \sigma_0 + \frac{k_y}{\sqrt{d}} \quad (2.1)$$

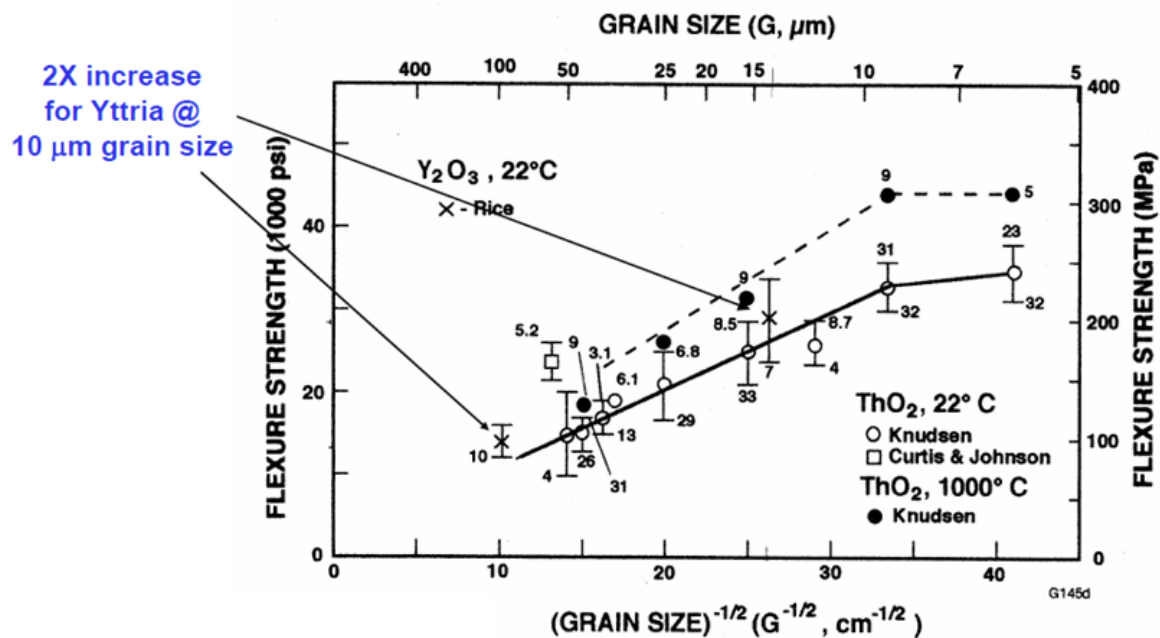


Figure 2.11 Data showing that flexural strength of Y₂O₃ (and ThO₂) is inversely proportional to the square-root of the grain size (Hall-Petch relationship). (Raytheon)¹

2.9 Discussion

The cubic, monoclinic, and hexagonal polymorphs of Y_2O_3 are well documented in the literature. There is disagreement about whether Y_2O_3 forms the high-temperature fluorite-like cubic phase or hexagonal phase at temperatures near its melting point. The tendency for Y_2O_3 to form a distinct high-temperature phase separate from the three other pressure-dependent polymorphs may potentially explain several interesting surface modifications that have been observed in a number of our experiments.

What stands out is that the cubic-to-monoclinic RE transition has only been observed for powders, micro-volume materials, or thin-films⁶⁸. To date, no other study exists where the morphology or physical properties of bulk monoclinic Y_2O_3 have been investigated, giving our study precedent.

3 OBJECTIVES

After initial work revealed that a novel phase transformation process could be used to refine the grain size of c-Y₂O₃, the need to resolve several critical issues guided much of the following research.

Although the cubic-to-monoclinic Y₂O₃ phase transition is well documented, most studies refer to pressure-only processing methods, usually performed with a diamond anvil cell (DAC). To develop a working understanding of the HPHT processing methods, it was necessary to first determine the critical pressure P_c at which the cubic-to-monoclinic Y₂O₃ phase transformation could be achieved at 1000°C. Based on the results from initial experiments, a processing temperature of 1000°C, which is well below 0.5 T_m for Y₂O₃ (2425°C), was chosen as the standard for forward and reverse transformations.

The next step was to determine how the processing temperature affects the reverse monoclinic-to-cubic Y₂O₃ transformation at 1.0 GPa. Since the monoclinic-to-cubic transformation results in a *decrease in density and accompanied increase in volume*, a processing pressure of 1.0 GPa is necessary to prevent complete structural failure. In fact, post-annealing at ambient pressures leads to disintegration of the material.

Our work also yielded unexpected surface morphology and chemistry effects that differed from that of the interior. It is thought that these effects are greatly influenced by HPHT processing technology. Although these effects are often localized at sample surfaces and edges, there is evidence that they could

negatively affect the properties of bulk regions. A greater understanding was needed to devise ways to reduce the extent and impact of these surface effects.

Early observations strongly suggested interactions between samples and HPHT graphite crucible, possibly explaining some of the unexpected surface effects that were produced. This interaction is explored in more detail in order to mitigate some of the morphological changes apparently due to carbon infiltration.

4 EXPERIMENTAL METHODS

In what follows, we describe details of the equipment used to anneal samples under pressure, considerations by which new experiments were devised, and methods by which such heat- and pressure-treated samples were characterized and analyzed.

4.1 Experimental Setup – High Pressure and Temperature

Processing

4.1.1 Apparatus

All high pressure/high temperature (HPHT) experiments were performed at Diamond Materials Inc. (DMI) - a spin-off company from Rutgers' Center for Nanomaterials Research (CNR). DMI's high-pressure press offers flexibility in size and shape of samples that can be processed, and is used for the synthesis of high pressure phases and consolidation of nanopowders^{69,70,71,72}.

A schematic of the HPHT system, described in detail in U.S. patent 8,021,639 B1⁷³, is shown in Figure 4.1. The apparatus consists of a matching pair of WC/Co anvils (5), which are reinforced with pre-stressed 4340 steel rings (9-17). Bearing inserts (6, 7) distribute the loading force from the hydraulic press (8) to the anvils, and a rubber ring (4) provides a non-conductive and deformable separation between anvil edges. At the center of the apparatus is the reaction cell, (1-3).

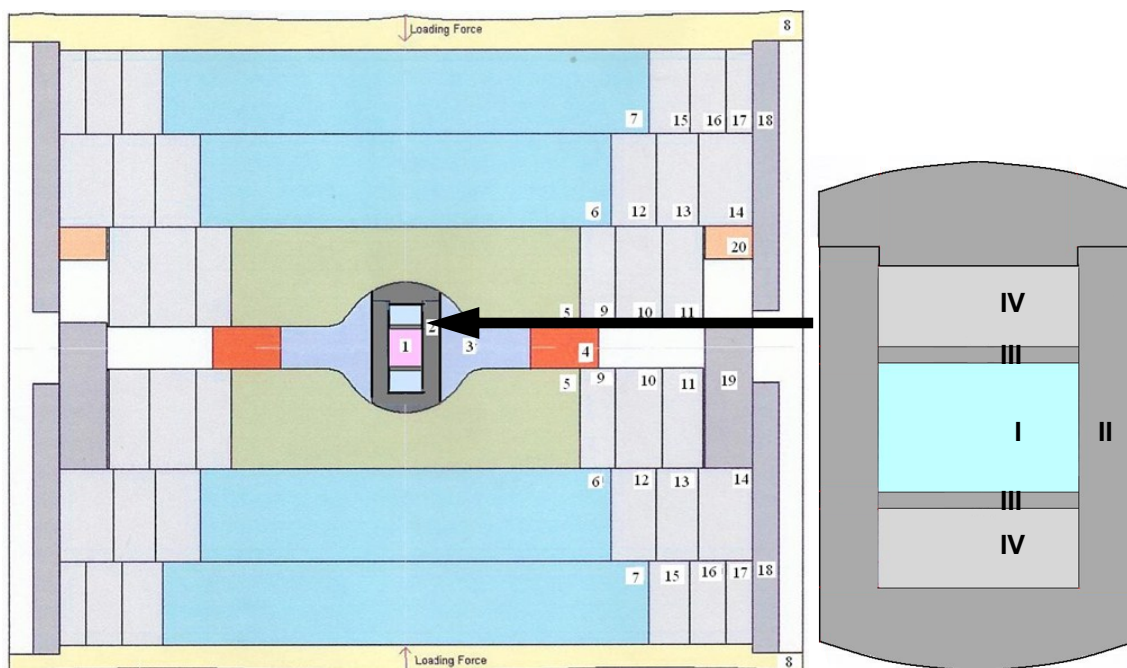


Figure 4.1 Schematic of DMI HPHT apparatus. (DMI)

The reaction cell, shown in Figure 4.1, contains a removable disc-shaped sample (I), and consists of a resistively-heated graphite crucible (II), graphite spacers (III), and insulating clay washers (IV). A critical component is the pressure-transmitting medium, which consists of a deformable ceramic ring (3) that encompasses the reaction cell. This ring deforms under high pressure to match the profile of the anvils. The lava stone ring then exerts a strong restraining force on the cell, generating a near-isostatic pressure in its working volume.⁷⁴

For the 5-mm diameter samples of interest herein, DMI's 300-ton press is capable of applying pressure up to 8.0 GPa and the resistive heating element can reach temperatures up to 2000°C. In this investigation, most of the reversible phase transformation testing was carried out at pressures of 1.0-8.0 GPa and temperatures of 600-1000°C. Holding time at the peak temperature during

processing turned out to be an important variable. This was varied from 1-240 minutes, depending on the requirements of a specific test. In a typical test, a sample is placed in the graphite container, subjected to high pressure, heated to high temperature, and held for a specific time. Heating and cooling rates are set at 70°C/min. After cooling to room temperature under high pressure, the sample is unloaded, removed from the graphite container, and characterized for composition, structure and grain size.

Due to limitations in the high-pressure high-temperature control system, a complete reversible-phase transformation (RPT) cycle must be performed in two steps. Thus, after a forward phase transformation from cubic-to-monoclinic Y_2O_3 , a sample is removed from its graphite container and examined before being re-inserted into another graphite container to complete the reverse phase transformation from monoclinic-to-cubic Y_2O_3 . This *two-step process* enables changes in density, hardness, *structure, and grain size*, accompanying forward and reverse phase transformations, to be *independently measured* for each phase transformation experiment.

4.1.2 Methods

After sample insertion, the graphite crucible/ clay assembly is placed in the press and loaded. Once the desired pressure is applied to the crucible (Figure 4.2-I), the temperature is ramped up at a rate of 70°C per minute (II) (~15-minute duration) with the resistive heating current carefully monitored. Once the annealing temperature is reached, conditions are maintained for the desired holding time (III), after which the temperature is decreased at a rate of 70°C (IV). Finally, once room temperature is reached, the applied pressure is reduced (V) and the sample is removed from the crucible.

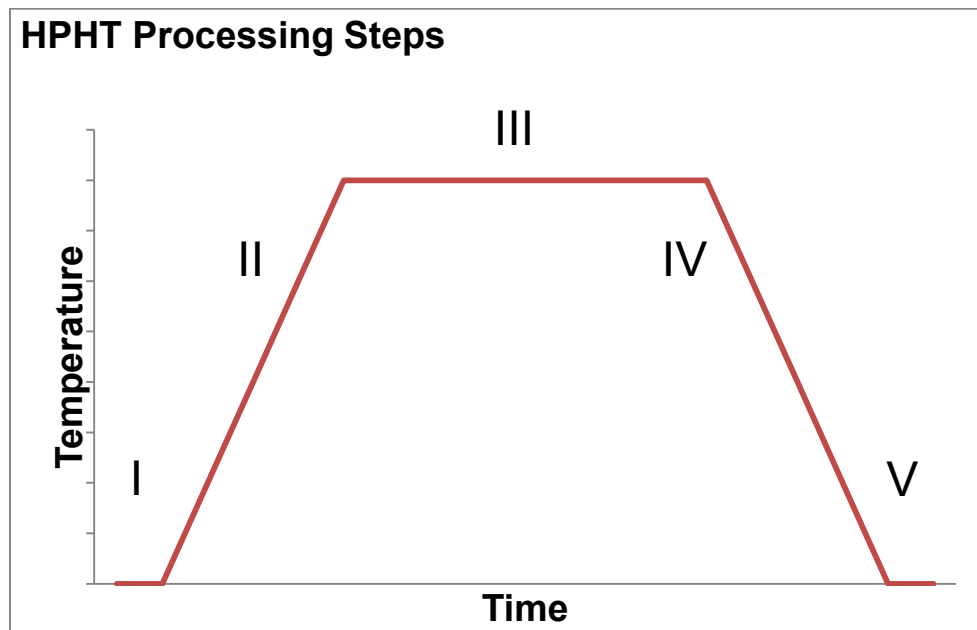


Figure 4.2 HPHT Processing Steps

Pressure is applied before the onset of heating for two reasons. First, pressure is required to create an electrically conductive path through the resistively-heated crucible. Second, the application of pressure deforms the

ceramic ring that surrounds the reaction cell to create a near-isostatic pressure condition.

4.1.3 Calibration

The pressure applied on the reaction cell is calibrated at ambient temperature for several known phase transitions in solid materials, Table 4-1. Variation in the electrical resistivity as a function of pressure signals that a phase transition has taken place. The dependence between loading force and resistivity allow for precise calibrations to be made. Figure 4.3 shows an example *pressure vs. loading force* calibration curve corresponding to the 1.0-8.0 GPa pressure range used for the relatively large sample volumes involved in this study.

Table 4-1 Pressure dependence of phase transitions in several materials at ambient temperature, used to calibrate pressure. (DMI)

Material	Pressure (GPa)	Material	Pressure (GPa)	Material	Pressure (GPa)
Ce	0.80 ±0.02	Yb	4.0 ±0.1	Fe	11.25 ±0.25
Bi I	2.55 ±0.01	Ba I	5.5 ±0.1	Ba II	12.6 ±0.5
Bi II	2.69 ±0.01	PbSe (Rmax)	5.9 ±0.7	Pb	13.0 ±1
PbSe (Rmin)	3.60±0.50	Bi III	7.7 ±0.02	GaP	22.0 ±3
Ti	3.67 ±0.05	Sn	9.4 ±0.04		

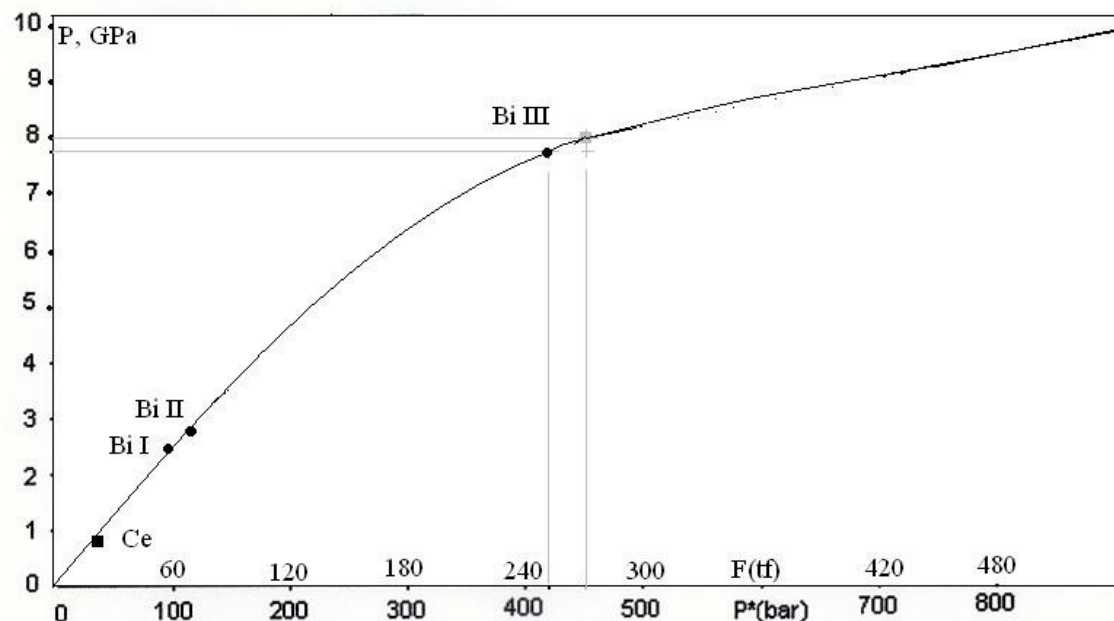


Figure 4.3 Dependence of pressure on loading force for known solid phase transitions at room temperature. (DMI)

Temperature is calibrated via known values of melting temperatures of different substances under high pressure: Sn (232°C), Pb (327.5°C), Al (660.3°C), and Cu (1084.6°C). Under ideal conditions, a sharp increase in electrical resistance of the reaction cell signals that fusion has occurred. In practice, the voltage drop across the reaction cell gradually increases as fusion occurs, and changes in current are measured. An example calibration curve, Figure 4.4, shows the dependence of temperature on the resistive heater power for a particular reaction cell in a particular container.

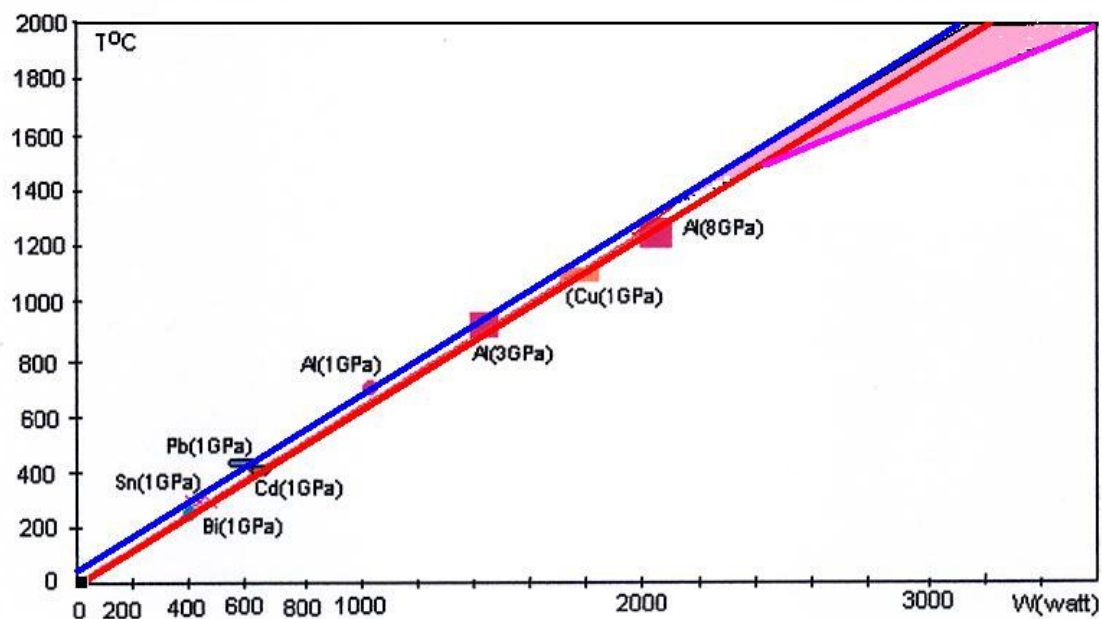


Figure 4.4 Dependence of temperature on power required to heat reaction cell.
(DMI)

4.1.4 Dimensional Changes and Complex Stress Conditions

Y_2O_3 samples that undergo phase transformation during HPHT processing experience dimensional changes, as described in further detail in Section 7.2. When samples are first put under load at the onset of HPHT processing, the surrounding pressure-transmitting medium deforms to create a near-isostatic state of stress. If there are any imbalances between direct anvil-applied and developed lateral pressures during processing, samples might also deform until the stress conditions equilibrate. Localized and sluggish nucleation and growth events can lead to a complicated state of stress that exacerbates the potential for unpredictable structural developments, as described in Section 7.3.

Samples undergoing phase transformations that result in negative volumetric changes will decrease in height during HPHT processing. A slight but always-present radial expansion is believed to be due to initial sample deformation at the onset of loading. Samples undergoing transformations that involve volumetric expansion will typically only expand in the radial direction. This confirms that, although the applied pressure and state of stress is near-isostatic during processing, the pressure-transmitting medium will yield in response to volumetric changes during processing.

If the pressure-transmitting medium cannot respond quickly enough to a sample's rapid radial expansion, considerable internal stresses may develop within the sample, only to be released upon unloading or removal from its

encapsulating crucible. In the most extreme cases, this leads to fracturing and even disintegration upon sample unloading.

4.2 Analytical Techniques

Samples processed at DMI are characterized at Rutgers' Center for Nanomaterials Research (Rutgers' CNR). XRD analysis is used for phase identification and to estimate grain size. SEM observation of fractured surfaces provides confirmation of grain size and insight on grain morphology. TEM micrographs and diffraction patterns enable phase and defect structures to be determined, and confirm the grain size of converted nano-structured materials. Raman spectroscopy is used for localized phase identification and to examine nucleation and growth patterns in partially transformed samples that feature mixed phase structures. Micro-hardness and nano-indentation techniques are used for mechanical properties measurements.

4.2.1 X-Ray Diffraction

Siemens D500 and X'Pert X-Ray diffractometers are used for phase identification and grain size determinations. The X-ray source in both instances is Cu K α , 1.54Å radiation.

A set of custom Al- sample holders with different depths were machined to hold powders and bulk samples (Appendix E). Powders were compacted and leveled using a thick glass slide. Small quantities of powder were analyzed by mixing with drops of high-purity ethanol to create a slurry that is then deposited onto a glass slide and allowed to dry. Alternatively, vacuum grease or double-sided tape was used to fix small quantities of powder, if background scans revealed no interfering peaks.

Firm poster-putty, a reshapable and reusable clay, is used to center and support bulk samples within a sample holder. Most clay putties give amorphous or crystalline peaks, making it necessary to collect background XRD spectra for subtraction. For best results, minimal putty is used, and the mounted samples are leveled using a thick glass slide. Scans often produce aluminum peaks due to the exposed surfaces of the sample holder.

X-Ray spectra are typically collected for a 2θ range of $10-70^\circ$. Step size and dwell duration are varied to produce sufficient resolution and signal to noise ratio. For quicker scans, a step size of 0.05 and dwell time of 1 second is used. For higher quality scans, a step size of 0.3 and dwell time of >2 seconds is used, especially when analyzing bulk samples or cross sections, due to their greatly reduced sampling area.

$$\tau = \frac{K\lambda}{\beta \cos\theta} \quad (4.1)$$

The Scherrer equation⁷⁵, Eq 4.1, is used for approximation of crystallite size, τ . The shape factor, K , has a typical value of 0.9; θ represents the Bragg angle; λ is the x-ray wavelength, 1.54\AA ; and β is the line broadening as measured at full width at half maximum (FWHM). The accuracy of the Scherrer equation is limited to nano-scale materials with grain sizes up to 100-200nm depending on several factors. It is also important to keep in mind that peak broadening can be influenced by factors other than grain-size, such as instrumentation and scan settings, lattice distortions, and grain stress and relaxation. Using the Scherrer equation can potentially falsely identify micro-scale

materials as nano-scale, requiring additional analysis to confirm crystallite size measurements. X-ray diffraction analysis software, such as MDI Jade, can automatically output grain size estimations if given user-input peak boundaries.

It is frequently desirable to collect multiple XRD spectra along a depth profile to determine whether a sample's surface phases are modified or representative of the interior structure. To do this, a 600-grit silicon carbide abrasive disc is used to gently remove the top layer of carbon that is transferred to a sample during HPHT processing. After an initial XRD diffraction scan, a sample is then glided over the 600-grit polishing disc a number of times. Sample thickness is measured with a high-precision thickness gauge or micrometer with 0.001mm accuracy. After a layer of set thickness is removed, usually 10 μ m, XRD analysis is repeated. This method of obtaining compositional analysis along a depth profile is less desirable than other methods, such as Raman spectroscopy (Section 4.2.5), because each removed layer is then no longer available for imaging or additional analysis.

4.2.2 Optical Microscopy

Optical microscopy is occasionally utilized to examine the crystalline nature of transparent samples. For instance, bright-field and back illumination can often reveal morphological variations in a transformed sample, without the need for fracturing. In such a case, examination of a sample that features a distinct core-shell structure reveals a coarser-grained shell structure with greater visual spectrum transparency.

An inverted-stage optical microscope is also used at times to visually examine the quality of a polished surface. Since a high-quality polish is needed for reliable hardness testing, it is paramount to check the quality of a sample's surface between polishing steps, and after final surface preparation. The inverted stage simplified this process as it allows epoxy-mounted samples to rest with polished surfaces parallel to the stage and focal plane.

4.2.3 Nano-Indentation

Nano-indentation methods are used to measure hardness variation across micro-scale distances and features. Measurements are done with a Hysitron Triboindenter equipped with a diamond Berkovich tip. An electrostatic transducer applies the test loads. The indenter is calibrated with a fused silica standard ($E = 68.11\text{ GPa}$, $H = 7.77\text{ GPa}$) to identify the tip function, and indents are performed in open air before each measurement to account for any position shifting prompted by errant electrostatic forces. Before measurements can be taken, it is necessary to map the boundaries of the sample using software controls and the built-in optical microscope for guidance. Indents are measured using the following settings: load control, open-loop indent, trapezoidal or triangular load function, loading rate of $200\text{ }\mu\text{N/sec}$, maximum load $1000\mu\text{N}$.

4.2.4 Micro-Hardness

Micro hardness measurements are taken using a Leco micro-hardness tester with built-in optical microscope and micrometer stage. A diamond Vickers tip was used, with applied loads of $200\text{g} - 1000\text{g}$. Indent measurements are

taken using the built-in microscope and occasionally double-checked using alternative optical or SEM imaging methods. Calibration is done by using a metallic test-block to ensure consistent and repeatable values were obtained. If a hardness profile is desired, the micrometer stage is typically adjusted to a minimum distance of 3 times the size of the indent. That is, if an indent is 50 μm in diameter, the next indent in the series will usually be placed a minimum of 150 μm away. This is done to ensure that micro-cracking from one indent does not affect the hardness measurements of the next indent in a line profile series.

4.2.5 Raman Spectroscopy

Raman spectroscopy uses monochromatic (laser) light to determine the vibrational modes of a material. Interaction between the laser light and vibrational excitation of the sample material results in elastic scattering and minor inelastic scattering where the energy of the incident photons will be shifted up or down⁷⁶. Thus, by the shift in wavelength, information about the vibrational modes of the system is obtained. Raman spectroscopy is sensitive to vibrational variations such as bond length, arrangement, and strength. Because of this, Raman spectroscopy can be used to differentiate between different material phases, such as the distinct polymorphs of Y_2O_3 .

A Renishaw Raman Microscope was used. Three laser sources are available – 785nm, 633nm, 514nm, with 1mm spot size and 30 μm , 10 μm , 1 μm penetration depths in Si, respectively. Reference spectra are obtained for c- Y_2O_3 and m- Y_2O_3 using all three lasers. There are no significant differences between

spectra, indicating that there are no resonance interactions with the three laser wavelengths.

Most Raman spectra are collected using a 633nm laser at the following settings: 50% laser intensity, 1200 or 1800 l/mm grating, extended range spectral acquisition, 20x or 50x magnifications, and 10-second exposure. The Raman microscope is calibrated to internal Si standard (peak shift at 510-520 cm^{-1}) before each set of measurements.

4.2.6 SEM Imaging

A Zeiss-Gemini field emission scanning electron microscope (FESEM) is used for sample imaging and EDS chemical analysis. Imaging is done primarily via an Everhart-Thornley secondary electronic detector, and an in-lens detector. The ET-detector is used for topographical and compositional contrast, and the in-lens detector is used when greater compositional contrast is desired.

The FESEM is primarily operated at 3KV, as cubic and monoclinic Y_2O_3 materials are prone to charging. In addition to minimizing charging effects, lower operating voltages allow for easier identification of carbon-rich decoration. This is because imaging done at higher electron beam voltages, such as 5KV, result in deeper sample penetration and interaction volumes, reducing the proportion of secondary electron emission and elemental contrast from surface phases, as demonstrated in Figure 4.5. The aperture is most often set to 30 μm , and working distance ranges from 5-10mm.

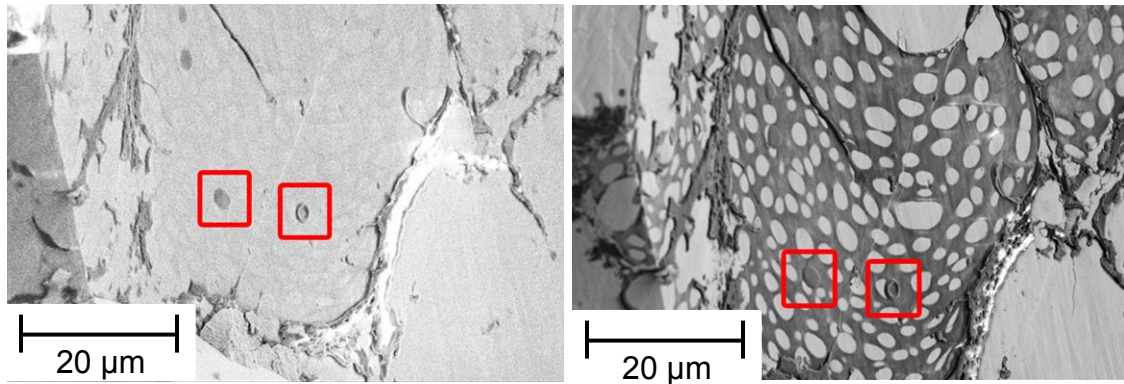


Figure 4.5 FESEM images of same area, showing carbon decoration on a monoclinic- Y_2O_3 grain boundary, taken at 5.0 KV (left) and 2.0 KV (right).

Bulk samples are prepared for SEM examination by light rinsing with ethanol. Samples that have previously been mounted for hardness measurements or polishing are ultrasonically cleaned in an acetone bath for 15 minutes and then an ethanol bath for 15 minutes. Clean samples are then fractured to expose their internal structure before mounting aluminum SEM studs. Conductive carbon tape, sourced from SPI Supplies, is used to secure samples to studs.

4.2.7 EDS Analysis

Energy-dispersive x-ray spectroscopy is used to determine the chemical composition of a sampled area. The incident electron beam excites the sampled area, leading to the ejection of inner energy shell electrons. A high-energy outer shell electron then moves to fill in the electron hole, and the difference in energy is released via characteristic x-rays that are collected by a liquid-nitrogen-cooled detector.

EDS analysis is used to determine the elemental makeup of individual grains, interfaces, and features, and across wider areas to obtain average intensity. As stated by Zeiss representatives, the x-ray detector is optimally positioned to collect x-rays from samples positioned at a working distance of 8.5mm. In order to obtain a sufficiently high collection rate and characteristic energy range, the operating voltage is increased to 5.0KV. In many occasions, a 60µm aperture is used. After each series of EDS characterization, imaging is repeated to ensure that excessive charging did not cause the beam to shift or drift during scans.

4.2.8 TEM Analysis

Transmission electron microscopy is utilized to obtain high-resolution images and diffraction patterns of nano-structured samples. In bright field and dark field imaging modes, information about crystallite size, orientation, and grain boundary phases is obtained. Selected area diffraction is used for high-accuracy phase identification and for additional confirmation regarding crystallite size.

Samples are prepared for TEM analysis by lightly crushing with an agate pestle and mortar partially filled with high-purity ethanol. A pipette is used to separate the finer suspended particles from the coarse aggregates at the bottom of the mortar. Droplets of the suspension are then deposited over a TEM grid. 200 mesh copper TEM grids with holey or lacey carbon films are sourced from SPI Supplies.

4.2.9 XPS Analysis

X-ray photoelectron spectroscopy is a technique that can provide the elemental composition of a material. XPS is most commonly used to analyze the surface chemistry of materials along a depth profile. This technique is used in our study to determine the chemical composition along grain boundaries in fractured surfaces, and ion beam etching was used to remove surface layers to provide a depth profile.

4.2.10 Archimedes Density

The density of each received and processing sample is calculated at DMI by weighing each sample and recording their dimensions. Density measurements are obtained via Archimedes method at Rutgers.

$$\rho = \frac{m_d}{m_d - m_s} \quad (4.2)$$

Archimedes density measurements require a high-precision electronic balance, a small tray that bridges over the weighing plate, a beaker of water, supports that attach to the weighing plate and reach up and over the beaker, and a hanger with dry-weighing tray and spring-bowl that submerges below the beaker water line. After the balance is tared, samples are placed in the dry tray and then the submerged spring-tray to obtain dry and immersed mass measurements. Samples are then dried and measurements are repeated another three or four times before being averaged. The density of water is measured after each experiment, and small aluminum spheres are used for additional calibration.

The density is calculated from the dry mass divided by the difference between dry mass and apparent submerged mass, Equation 4.2.

4.2.11 Sample Fracturing

In order to examine the microstructure of as-received and processed samples, it is necessary to fracture them. Fracturing is done in one of two ways – by propagating a crack through the bulk of the sample or by manually applying flexural or torsional forces until fracture occurs.

Fracturing a sample via crack propagation is achieved by scoring with a diamond scribe and then using a small hammer and cold chisel to advance the crack tip. Alternatively, diamond indentation with a very high load can be used to fracture thinner samples.

Flexure or torsion fracturing involves bending or twisting a sample until it fails. This is done inside a gallon-sized zip-closed bag by gripping a sample on opposite sides with two non-serrated precision pliers and bending until the sample fractures. The pliers are faced with disposable sterile liners to minimize potential contamination. A twisting motion may help when tougher samples prove to be too difficult to fracture via bending alone.

An alternative option for fracturing high-strength samples is to first use a diamond saw to reduce the sample's effective thickness. However, sawing through a sample greatly reduces the surface area of a fracture surface that can be examined and analyzed. In addition, a sample must be prepared for diamond

sawing by mounting it to a glass or aluminum slide with a low-temperature crystalline wax adhesive. Removing adhesive residue requires ultrasonic cleaning in acetone and then ethanol. Excessive handling and manipulation of delicate as-sawn samples can potentially lead to premature fracturing and unintended damage or contamination.

4.2.12 Sample Polishing and Surface Preparation

Samples must often be polished as preparation for analysis or characterization techniques. To facilitate polishing and to achieve better results, samples are first mounted in epoxy. *Sampl-Kwick*, a fast-curing two-part epoxy, is sourced from Buehler. One-inch diameter molds are swabbed with a release agent before placing samples that are to be mounted inside. The epoxy is mixed and then poured into the molds. A slower-curing epoxy is used if high shrinkage associated with the quicker curing epoxy is an issue.

Polishing is done on a speed-controlled 8-inch polishing wheel that features a water spout for lubrication and debris removal. Coarse polishing is done in several steps using paper-backed silicon carbide abrasive discs in several grit sizes: 320, 400, 600, 800, and 1200. Finer polishing requires the use of diamond paste in 6 μ m, 3 μ m, 1 μ m, and 0.25 μ m sizes, medium-nap polishing pads (Buehler Texmet 1000), final-step polishing pads (Buehler Microcloth), and a light oil lubricant. Mechano-chemical finishing is done with 0.02 μ m colloidal silica or a proprietary Buehler formula optimized for etching ceramics.

Samples are carefully rinsed and dried, preferably with dry nitrogen, after each polishing step. After the final polishing step, samples are removed from their brittle epoxy mount using a small hammer and chisel. In some cases, such as for hardness testing, it might be convenient to keep polished samples embedded in epoxy.

5 CUBIC Y_2O_3 PHYSICAL AND CHEMICAL CHARACTERIZATION

5.1 As-Received Samples

Two batches of disc-shaped samples (5 mm diameter x 3 mm height) of fully-densified optical-grade polycrystalline c- Y_2O_3 were obtained from Raytheon IDS. Core drilling is used to extract the samples from much larger pieces, fabricated by sinter-HIP technology. High-purity Y_2O_3 powder is sourced from Baikowski Group. Most of the HPHT processing discussed in the following sections is carried out on as-received samples. In a few tests, however, thinner samples are used, primarily in order to gain a better understanding of grain size changes accompanying surface modification. The thinner samples are obtained by silicon carbide and diamond polishing, making sure that opposite faces remained parallel; otherwise, non-uniform stress distributions develop under high pressure, which can lead to cracking.

The initial batch of samples had coarse-grained microstructure with 300 μm grain size. Most critical experiments are performed using samples from the second batch of discs, with 1.5 μm average grain size. As-received discs are transparent and with optically-flat-polished faces.

5.2 SEM Imaging of Fracture Surface Microstructure

SEM examination of fractured samples from each batch shows an average grain size of $\sim 300\text{ }\mu\text{m}$ in the first batch, and $\sim 1.5\text{ }\mu\text{m}$ in the second batch, Figure 5.1, in agreement with the samples' source (Raytheon). Whereas the fracture behavior of the $300\text{ }\mu\text{m}$ grain size material is dominantly intergranular, the $1.5\text{ }\mu\text{m}$ grain size material fracture behavior is mostly intragranular.

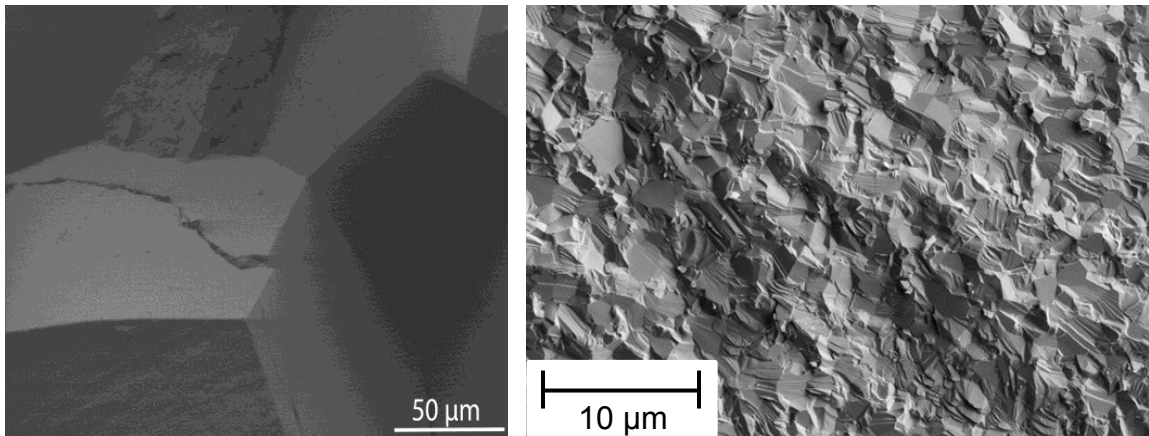


Figure 5.1 SEM images of fractured samples from $300\text{ }\mu\text{m}$ grain cubic- Y_2O_3 material (left), and $1.5\text{ }\mu\text{m}$ grain starting material (right).

5.3 EDS Characterization

EDS analysis of an intergranular 300- μm grain sample fracture surface reveals the presence of boron and carbon, which are also detected in the fractured surface of the 1.5 μm grain sample, Figure 5.2. This shows that both coarse and fine-grained materials have comparable levels of impurities, possibly due to residue from a sintering aid.

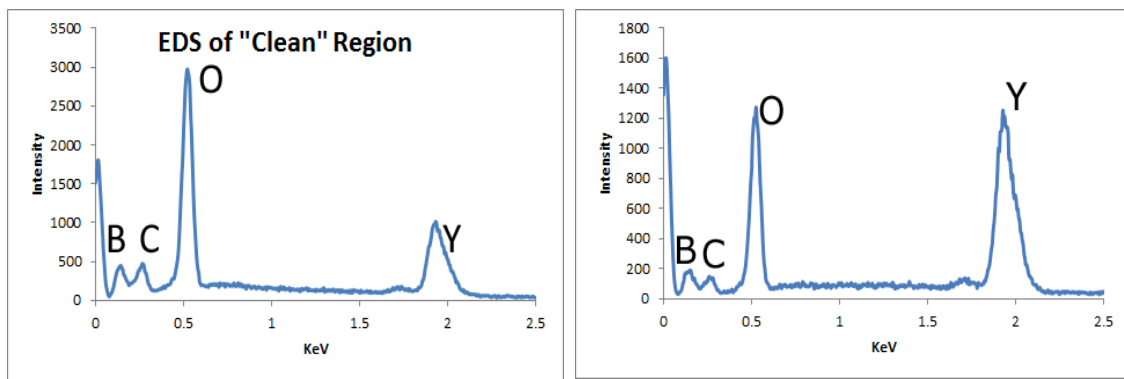


Figure 5.2 EDS analysis of as-received 300- μm grain (left) and 1.5 μm grain (right) samples.

5.4 X-ray Diffraction

XRD analysis of the as-received 1.5 μm -grained material gives a characteristic pattern for pure polycrystalline cubic Y_2O_3 . No other polymorphs or intermediate phases are detected.

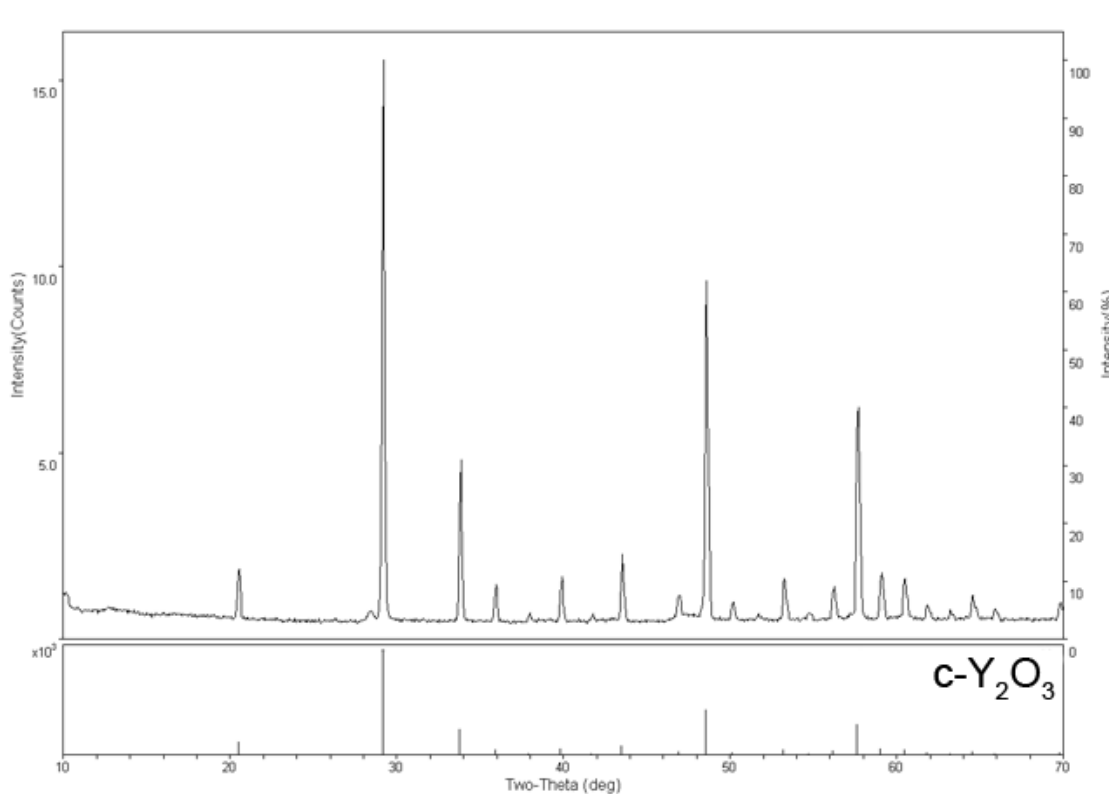


Figure 5.3 X-ray diffraction spectra of as-received Y_2O_3

5.5 Raman Spectroscopy

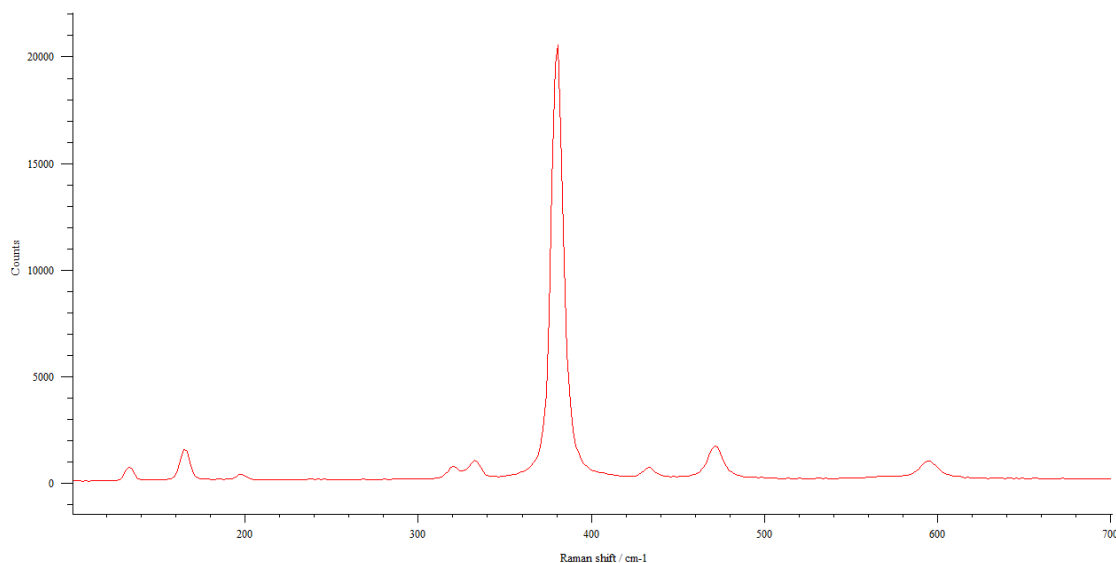


Figure 5.4 Raman pattern for as-received cubic Y_2O_3 .

A characteristic Raman pattern for cubic- Y_2O_3 is shown in Figure 5.4, with all visible peaks listed in Table 5-1. A 633nm laser source is used.

Table 5-1 Raman shift for as-received cubic Y_2O_3

(cm^{-1})	133	165	197	320	333	380	434	472	595
---------------	-----	-----	-----	-----	-----	-----	-----	-----	-----

5.6 Density and Hardness

Initial density was measured using Archimedes method to be 5.02 g/cm^3 , which is agreement with theoretical values for fully-densified cubic- Y_2O_3 . Vickers hardness was measured as $6.8 \pm 0.13 \text{ GPa}$.

6 MONOCLINIC Y_2O_3 PHYSICAL AND CHEMICAL CHARACTERIZATION

6.1 Initial Observations

Complete cubic-to-monoclinic conversion occurs rapidly when a cubic Y_2O_3 sample undergoes treatment at 8.0 GPa/1000°C/1-15 min. It is concluded that, due to the nature of the cubic-to-monoclinic phase transition and speed of transformation, the mechanism is a displacive or shear transformation. Sample surfaces are visibly textured and darkened due to interaction with the graphite crucible. The immediate interior region at surfaces and edges is also often dark in appearance, an effect attributed to an oxygen-deficient non-stoichiometric composition.

Monoclinic Y_2O_3 samples display a reduction in size (Section 7.2) due to the decrease in molar volume associated with the cubic-to-monoclinic Y_2O_3 transition. It is difficult to fracture samples that have been transformed to the monoclinic phase at high processing pressures. The interior of a fractured monoclinic Y_2O_3 sample is an opaque light-medium shade of pale gray. White spots will often be observed in fracture surfaces, possibly indicative of areas of higher stress. SEM imaging does not reveal any distinction between pale gray and white-spotted regions.

6.2 X-ray Diffraction

XRD spectra for samples processed at 8.0 GPa/1000°C/15 min identify as monoclinic Y_2O_3 , Figure 6.1. The peaks often appear shifted, indicating that the structure is internally stressed. An absence of peaks corresponding to the cubic phase indicate that *complete phase transformation* has occurred.

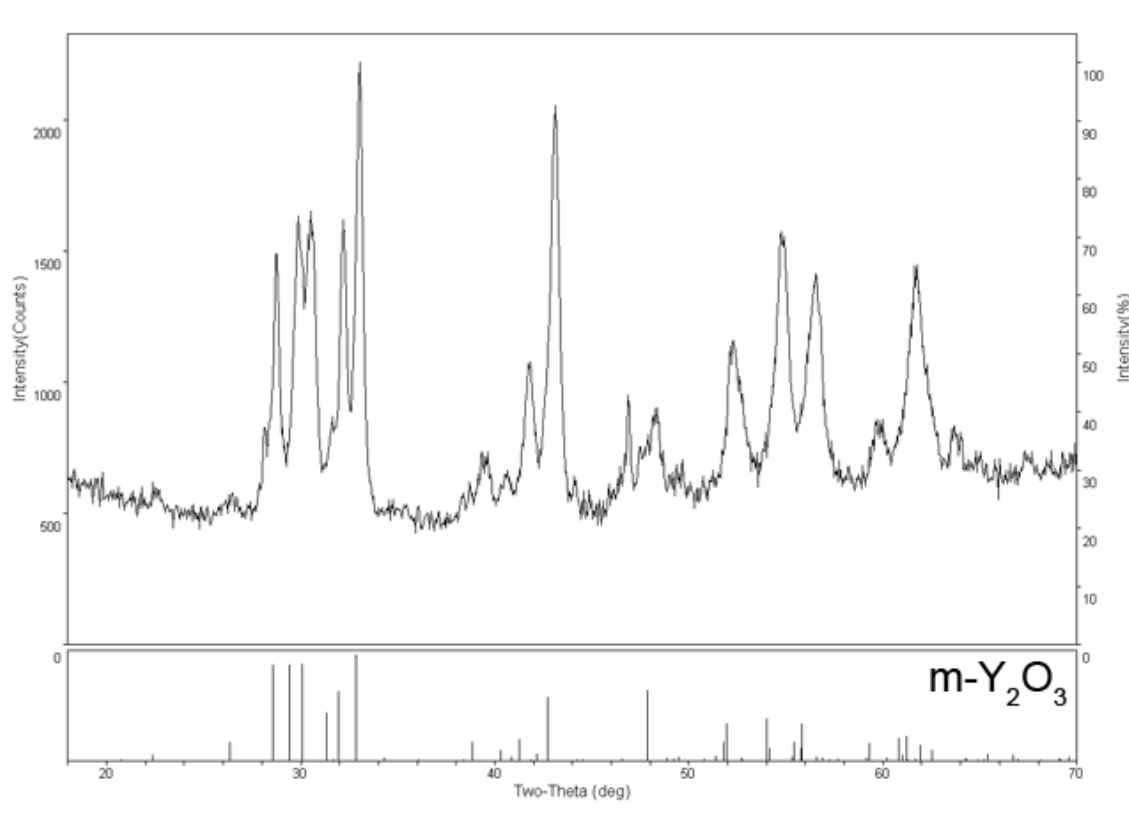


Figure 6.1 Characteristic XRD pattern for as-processed monoclinic Y_2O_3 .

6.3 SEM Imaging

Examination of the fracture surface of a monoclinic Y_2O_3 sample, transformed from the cubic phase at 8.0 GPa/1000°C/15 min, reveals a mostly transgranular morphology. At the surface and throughout the interior, isolated grain boundary facets are surrounded by a transgranular matrix. Some cracking is visible, and is believed to originate during fracturing.

Because the cubic-to-monoclinic Y_2O_3 transformation results in a nano-grain product, the faceted features, which correspond to prior cubic grain boundaries, falsely represent the true granular structure of the material. The nano-grain monoclinic grains, although not visible via SEM imaging techniques, are present within the faceted regions.

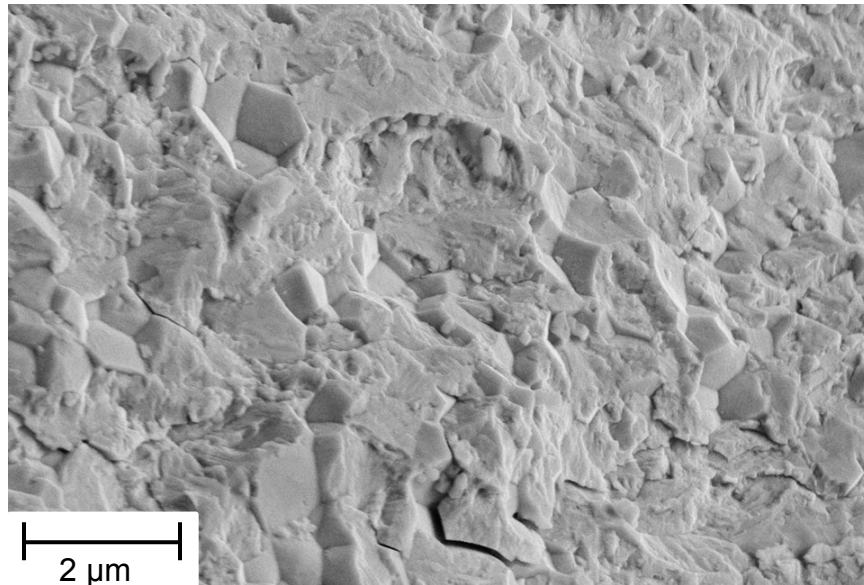


Figure 6.2 SEM image of monoclinic- Y_2O_3 fracture surface.

6.4 EDS Chemical Analysis

EDS analysis shows that, as with the as-received cubic material, there are boron and carbon impurities. EDS spectra collected from the interior of fractured monoclinic Y_2O_3 samples transformed under high pressure show no measurable increase in carbon concentration.

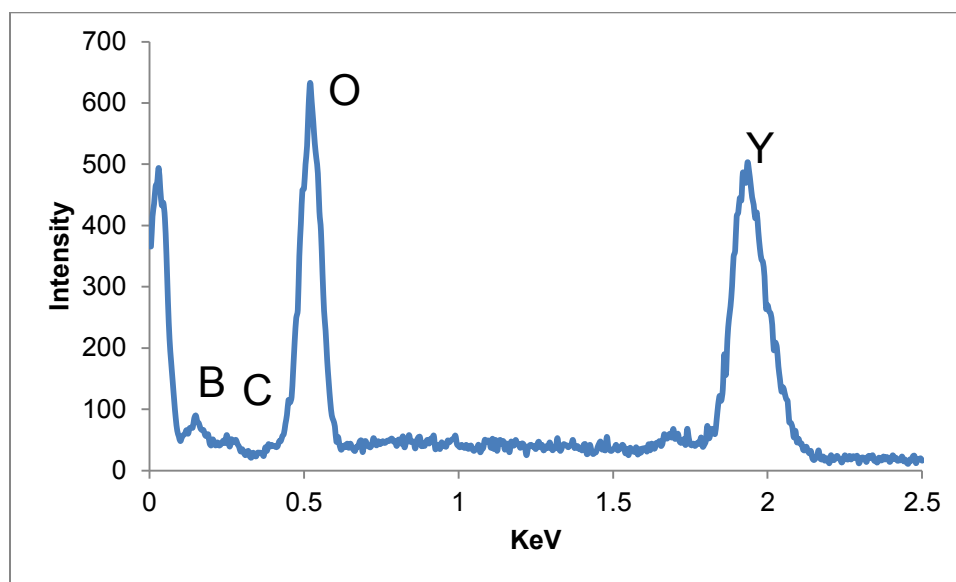


Figure 6.3 EDS analysis of shear-transformed monoclinic Y_2O_3 .

6.5 TEM Analysis

A sample processed at 8.0 GPa/1000°C/240 mins is crushed and prepared for TEM analysis. Grains are gently scraped off and collected from the sample surface by using a precision diamond file. Examination of the resulting bright field images and selected area diffraction patterns confirms the exclusive presence of the monoclinic phase. The micrographs and diffraction patterns (Figure 6.4) also show that grains originating from closer to the samples' outer edges (C, D) are larger than those taken from deep within the sample's interior (A, B).

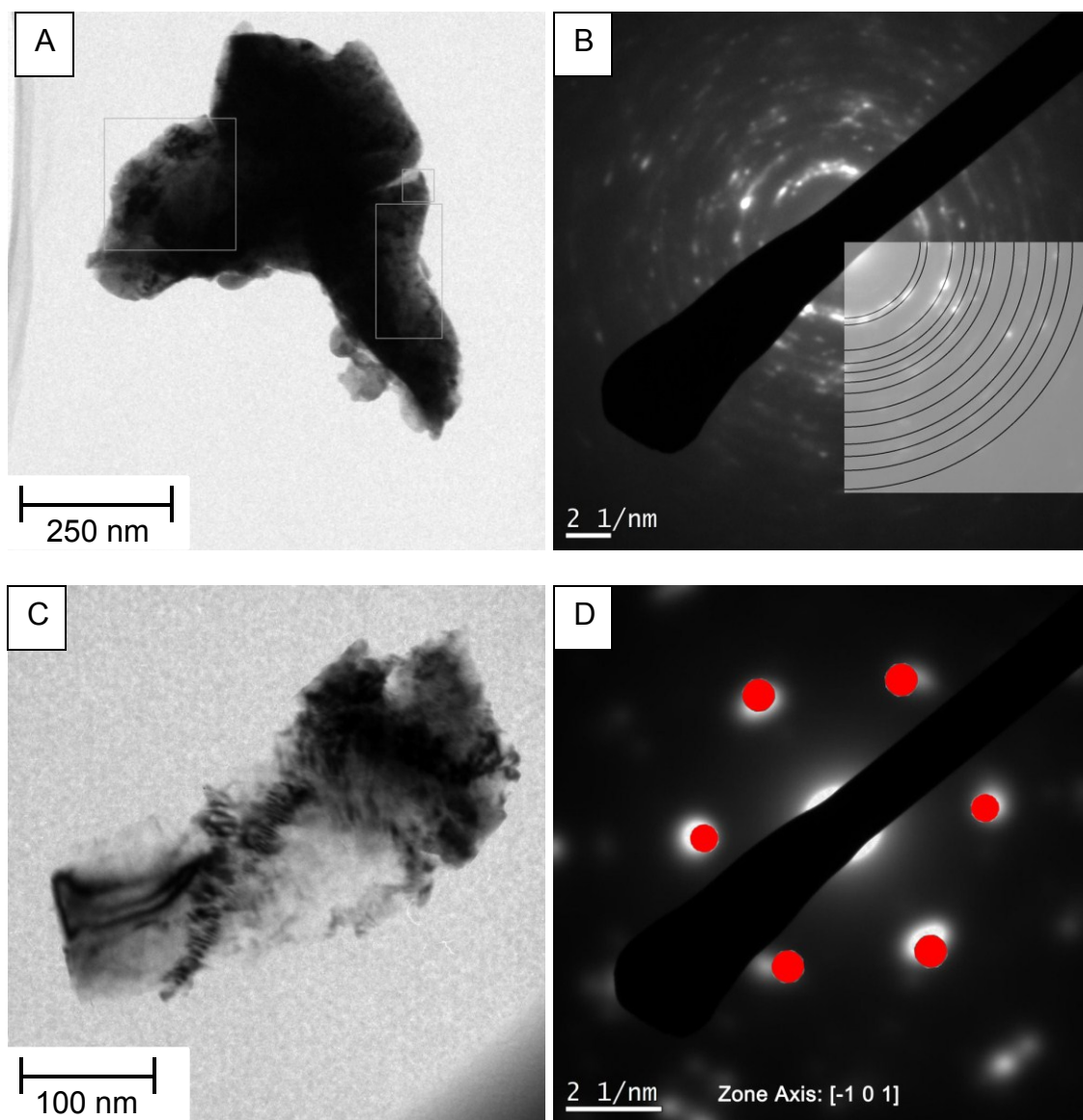


Figure 6.4 TEM diffraction patterns of grains collected from different regions of a transformed monoclinic Y_2O_3 sample, showing the presence of polycrystalline (A, B) and single-crystal (C, D) grains.

6.6 Raman Spectroscopy

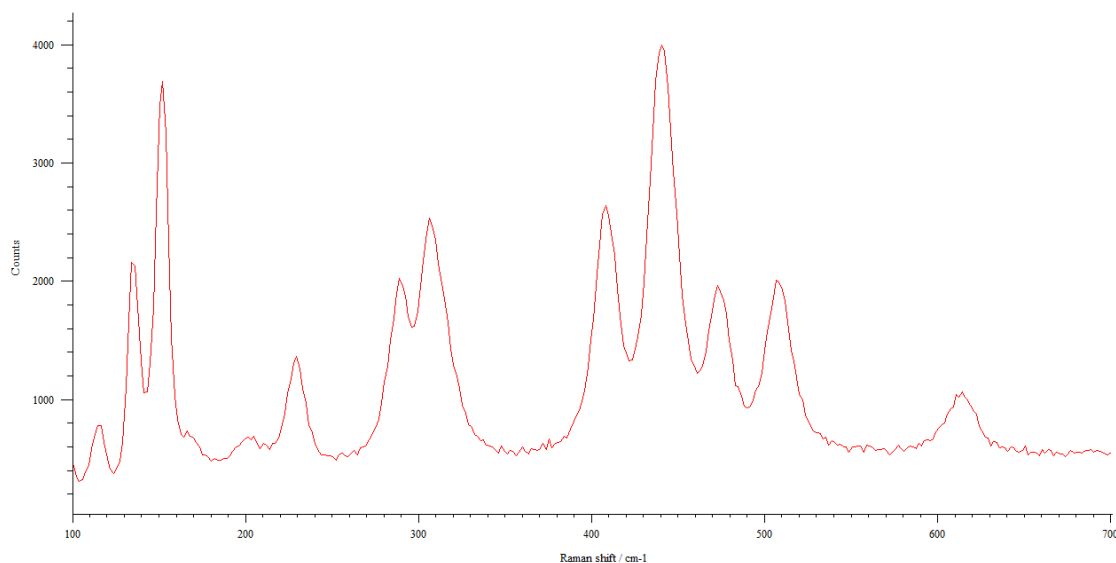


Figure 6.5 Raman pattern for monoclinic Y_2O_3 .

The Raman shift for monoclinic Y_2O_3 is significantly different than for the cubic phase (Section 5.5). This proves to be useful when characterizing regions of partial cubic-to-monoclinic or monoclinic-to-cubic transformation (Section 7.4.3).

Table 6-1 Raman shift peak list for transformed monoclinic Y_2O_3

(cm^{-1})	114	135	152	229	289	308	408	441	475	509	615
---------------	-----	-----	-----	-----	-----	-----	-----	-----	-----	-----	-----

6.7 Density and Hardness

The density of the monoclinic phase is measured using Archimedes method to be $5.35 \pm 0.07 \text{ g/cm}^3$, as compared to 5.03 g/cm^3 as for the cubic phase. Vickers hardness is measured to be 7.63 GPa for a sample processed at high pressure. Examination of fracture surfaces demonstrates that interior grains are much stronger due to conversion to the monoclinic phase, as compared to the starting material ($6.8 \pm 0.13 \text{ GPa}$).

The increase in density corresponds to a ~6% decrease in volume. The presence of carbon at the sample surface affects density measurements by a significant amount.

7 REVERSIBLE PHASE TRANSFORMATION

7.1 Overview

As detailed in Chapter 2, high-pressure phase transformations in Y_2O_3 and other rare earth sesquioxide phases are well documented in the literature. For Y_2O_3 , it has been reported that a pressure-induced transformation from cubic- to-monoclinic occurs at $\sim 2.5 \text{ GPa}/1000^\circ\text{C}$ ³³, but there is no consensus with respect to the reversibility of the transformation process^{15,33,39}.

In this investigation, preliminary experiments confirmed that a cubic-to-monoclinic transformation in Y_2O_3 occurs at $\sim 2.5 \text{ GPa}/1000^\circ\text{C}$, in agreement with results obtained using a diamond-anvil press. However, as noted earlier, much larger sample sizes can be produced by HPHT processing, thus enabling changes in density, hardness, and optical properties to be determined. Longer processing times (holding times) are also attainable, thereby permitting time-dependent structural changes to be studied. A complicating effect is sample/heater interaction, which is discussed in Chapter 8.

7.1.1 Prior Research

In a recent publication¹⁰, we described a pressure-induced *reversible-phase transformation* process to convert polycrystalline cubic- Y_2O_3 directly into the nanocrystalline state. Briefly, when cubic- Y_2O_3 is subjected to $8.0 \text{ GPa}/1000^\circ\text{C}/15 \text{ min}$, the cubic phase transforms into monoclinic phase. Upon re-processing at $1.0 \text{ GPa}/1000^\circ\text{C}/15 \text{ min}$, the material reverts back to the cubic

state. This is illustrated in Figure 7.1 for a starting material of coarse-grained ($\sim 300\text{ }\mu\text{m}$) c- Y_2O_3 . As indicated, the *forward-phase transformation* from cubic-to-monoclinic yields a reduction in grain size to $\sim 100\text{ nm}$, which is retained upon *reverse-phase transformation* from monoclinic-to-cubic. Figure 7.1 (a) shows characteristic peaks for c- Y_2O_3 , but their relative intensities do not match that of a standard powder diffraction pattern. This is because only a few surface grains of the coarse-grained material are in favorable orientations for diffraction. On the other hand, Figure 7.1 (c) shows all the characteristics of a powder pattern, indicating that the final nano-grained c- Y_2O_3 has no preferred orientation. It is concluded, therefore, that the effect is due to random nucleation and limited growth of c- Y_2O_3 nanoparticles within the intermediate nano-grained m- Y_2O_3 matrix.

TEM observations, Figure 7.2, confirm that the reversibly-transformed material has a grain size $\sim 100\text{ nm}$ ¹⁰. Figure 7.2 (a) is a dark-field image and electron diffraction pattern of the same area, showing randomly-oriented nanograins of c- Y_2O_3 in the reversibly-transformed material. The spotty-ring pattern, while displaying all major reflections for c- Y_2O_3 , also shows a weak (310) ring for m- Y_2O_3 ; a rough estimate of the retained m- Y_2O_3 phase is 1-3 %. In some areas of the sample, there is evidence for a very thin transition layer between well-crystallized nano-grains of c- Y_2O_3 , arrows in Figure 7.2 (b), where the reverse transformation is incomplete.

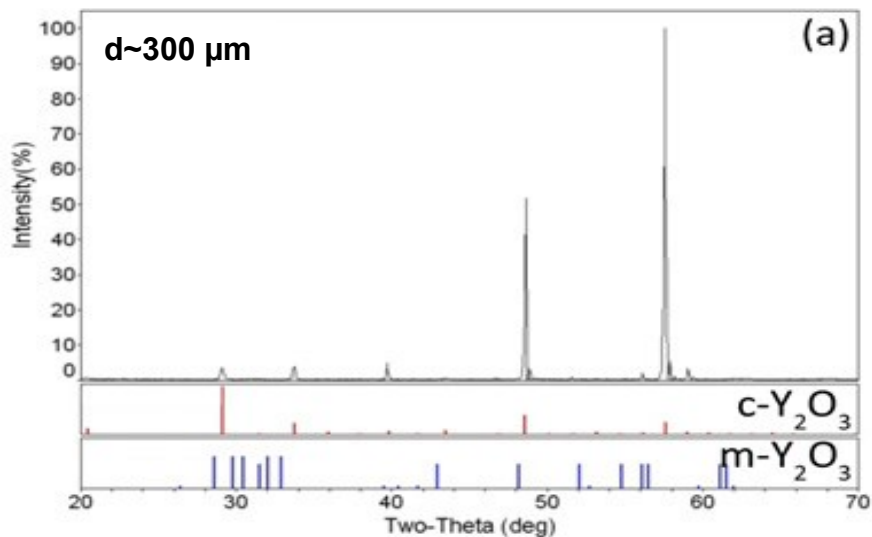
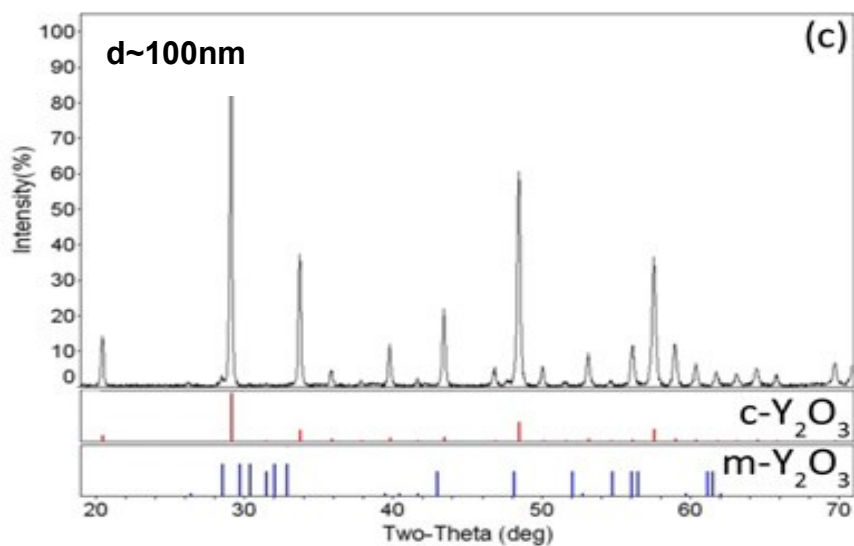
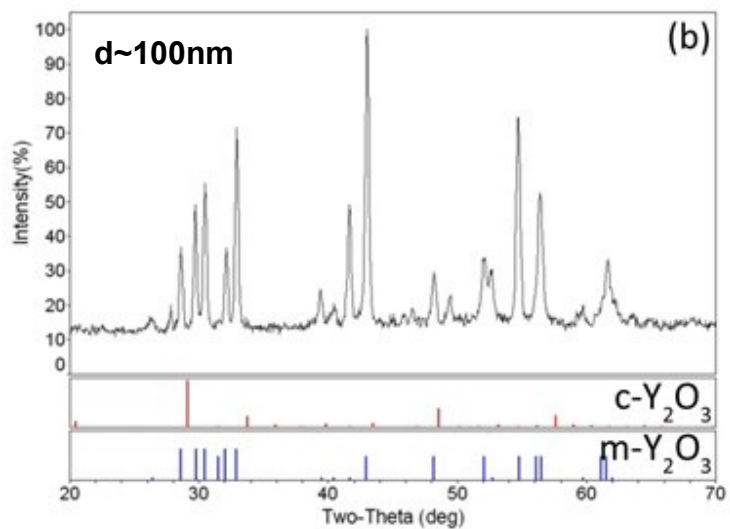


Figure 7.1 XRD patterns for (a) as-received cubic Y_2O_3 (~300 μm GS); (b) forward-transformed monoclinic Y_2O_3 ; and (c) reverse-transformed cubic Y_2O_3 .¹⁰



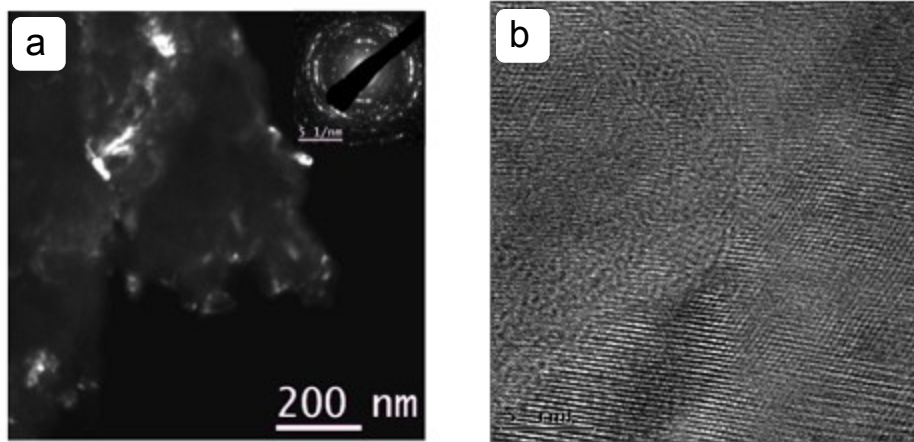


Figure 7.2 TEM images of coarse-grained (300 μm) material, after reversible transformation to nano-grained $\text{c-Y}_2\text{O}_3$: (a) dark-field image, and (b) lattice image. The inset in (a) is a diffraction pattern of the imaged region, showing a weak (310) ring from retained monoclinic phase.¹⁰

A typical fractured sample of coarse-grained material, Figure 7.3 (a), shows well-defined *intergranular fracture*. EDS analysis reveals segregation of carbon and boron at the grain boundaries, thus explaining their susceptibility to intergranular fracture. In contrast, fracture surfaces of forward- and reverse-transformed samples display more complex fracture modes. Figure 7.3 (b) shows intergranular fracture on a scale consistent with a nano-grained structure, whereas Figure 7.3 (c) shows faceted regions on a *scale that does not reflect a nano-grained structure*. A possible explanation is that the material retains some *memory* of its original coarse-grained structure, such that there are regions where the fracture path follows the original still-segregated and weakened grain boundaries. Fracture surfaces of forward- and reverse-transformed materials, therefore, are not reliable indicators of grain size, although they are for the starting materials.

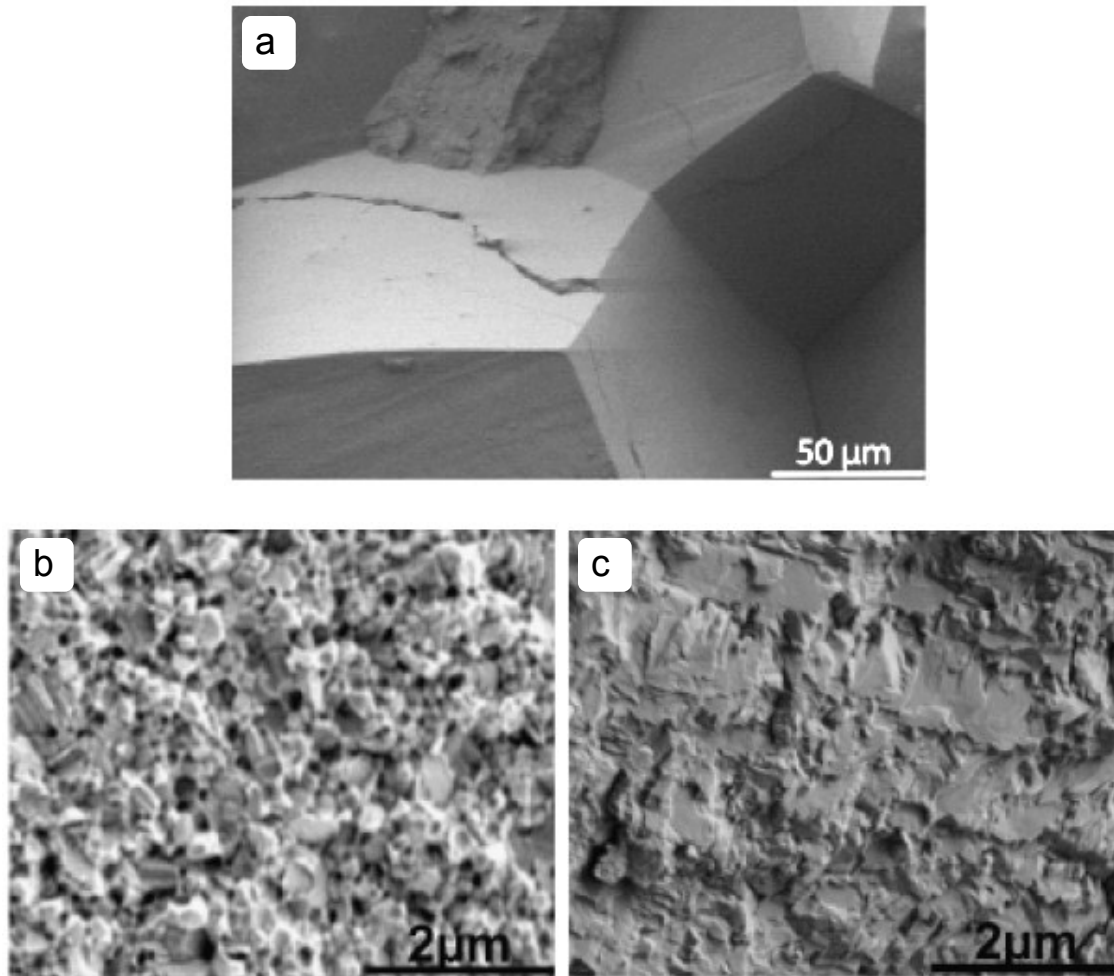


Figure 7.3 SEM images of fracture surfaces: (a) initial coarse-grained Y_2O_3 (300 μm), (b) after forward transformation to $m-Y_2O_3$, and (c) after reverse transformation to $c-Y_2O_3$.¹⁰

7.1.2 Current Research

In what follows, new results obtained for high quality (optical grade) fine-grained ($\sim 1.5 \mu m$) polycrystalline Y_2O_3 are described, highlighting the major effects of varying HPHT-processing parameters on grain size, morphology and hardness for both forward- and reverse-transformed materials. As will be shown, significant changes in grain size and morphology occur when the applied pressure is near the critical transformation pressure (~ 2.5 GPa). *The observed*

structural changes are consistent with a pressure-assisted nucleation and growth mechanism (Section 7.3.3).

The general behavior of fine-grained material, Figure 7.4, is similar to that of coarse-grained material, except that the final grain size of the c-Y₂O₃ is <50 nm. It is noteworthy that XRD pattern for forward-transformed m-Y₂O₃, Figure 7.4 (b), displays peak broadening and shifting, indicative of an internally-stressed nano-grained structure. Incomplete transformation to nano-grained m-Y₂O₃ may be responsible, since the misfit between m-Y₂O₃ and retained c-Y₂O₃ is large, and therefore could introduce large interphase-interface stresses. Upon close examination, there are no peaks that can be clearly identified with c-Y₂O₃, so that the volume fraction of untransformed c-Y₂O₃ phase is not large.

TEM observations, Figure 7.5, confirm the presence of reversibly-transformed c-Y₂O₃. A dark-field image and electron diffraction pattern of the same area, Figure 7.5 (a), shows a ring pattern with a few spots, indicating the presence of a few larger crystallites in an otherwise nano-grained matrix. A lattice image of the same region of the thin foil, Figure 7.5 (b), shows a good match with known lattice parameters of the c-Y₂O₃ phase, and a grain size <50 nm.

A similar reversible-transformation behavior is also observed in HPHT-processed Y₂O₃ powder (particle size <10 μm), although undesirable processing effects, as described in Section 8, are greatly exaggerated until densification occurs under pressure. Additionally, high internal stresses are developed during HPHT processing, leading to spontaneous fracturing during sample removal.

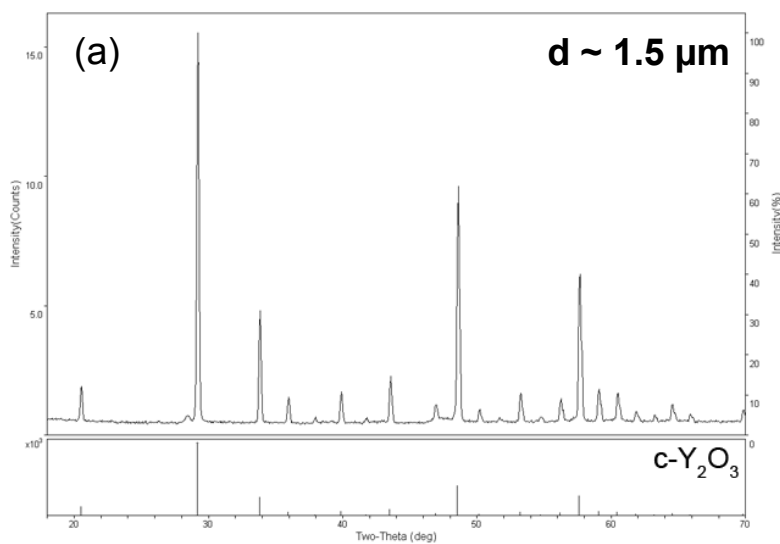
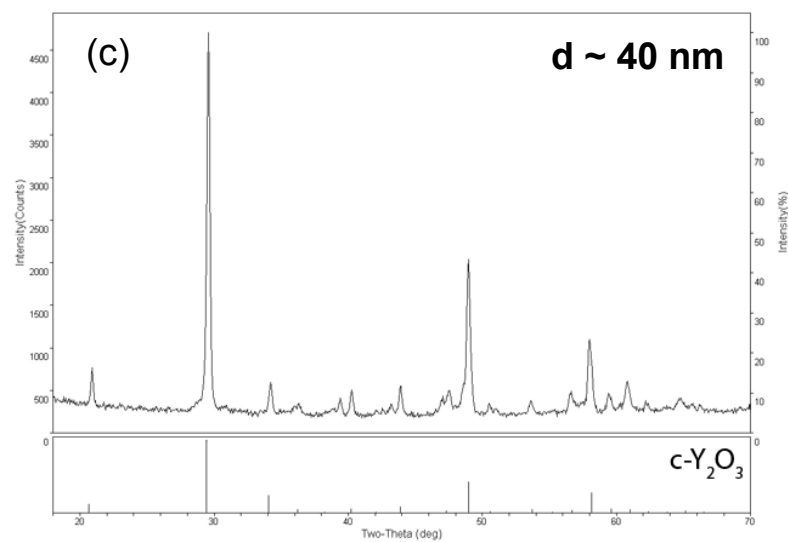
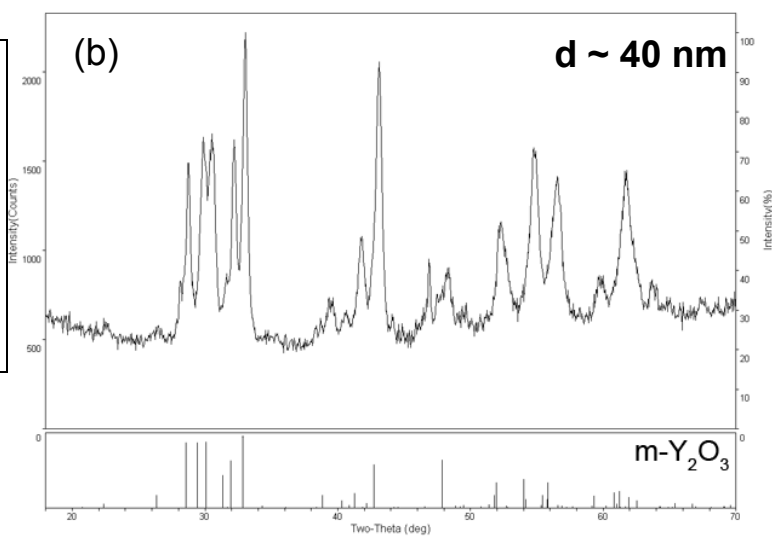


Figure 7.4 XRD patterns for (a) as-received cubic Y_2O_3 ($\sim 1.5 \mu\text{m}$ GS); (b) forward-transformed monoclinic Y_2O_3 ; and (c) reverse-transformed cubic Y_2O_3 .



Essentially the same behavior, therefore, is observed for coarse- and fine-grained materials, and for fine powder. In the case of powder, such a forward phase transformation, involving an increase in density, also facilitates powder densification during sintering, as discussed in previous publications on TiO_2 and Al_2O_3 ^{4,6}, and referred to as *transformation-assisted consolidation*.

Another favorable effect in powder densification, uncovered in preliminary experiments, is a significant increase in green density with pressure up to about 2.0 GPa. A high “green density” facilitates densification in pressure-less sintering, hot-isostatic pressing, and field-assisted sintering, all of which are of commercial interest.

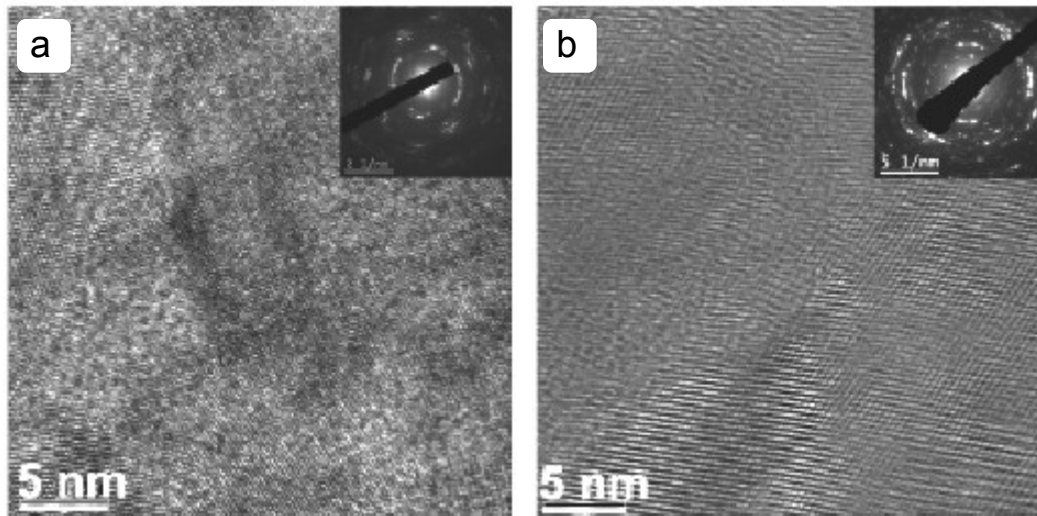


Figure 7.5 TEM images of fine-grained ($1.5\ \mu\text{m}$) material: (a) after forward transformation to $m\text{-Y}_2\text{O}_3$, and (b) after reverse transformation to $c\text{-Y}_2\text{O}_3$.¹⁰

In contrast to the intergranular fracture of coarse-grained ($300\ \mu\text{m}$) material, fine-grained ($1.5\ \mu\text{m}$) material displays mostly transgranular fracture, Figure 7.6 (a), apparently reflecting the higher purity of the fine-grained material,

thus reducing embrittlement by impurity-segregation at grain boundaries. On the other hand, fractured samples of forward- and reverse-transformed materials show more complex fracture modes, Figures 7.6 (b) and (c), which are difficult to interpret. In particular, we note the micron-scale facets in the fracture surface of the reversibly-transformed nano-grained c- Y_2O_3 , Figure 7.6 (c), which does not bear any relationship to the underlying nano-grained structure, as determined by XRD and TEM. As noted above, therefore, fracture surfaces of reversibly-transformed materials are not reliable indicators of grain size, but they still provide evidence for grain size in the starting materials.

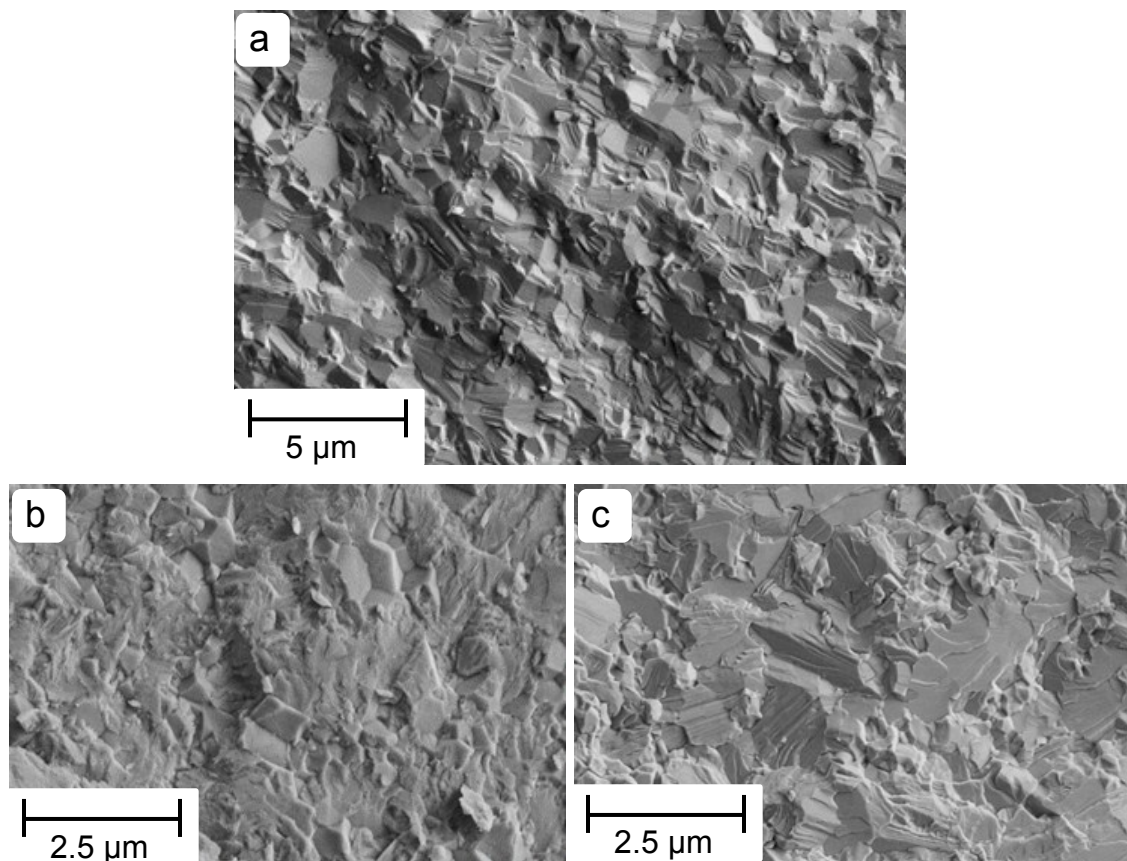


Figure 7.6 SEM images of fracture surfaces: (a) initial fine-grained Y_2O_3 (1.5 μm), (b) after forward transformation to $m\text{-Y}_2\text{O}_3$, and (c) after reverse transformation to $c\text{-Y}_2\text{O}_3$.

7.2 Changes in Sample Dimensions

When a phase transformation occurs in Y_2O_3 due to HPHT processing, it is readily detected by a change in sample volume. The forward transformation from cubic-to-monoclinic Y_2O_3 involves a decrease in sample volume of about 6%, whereas the reverse transformation from monoclinic-to-cubic Y_2O_3 involves an increase in sample volume of about 6%. Estimated densities of the two phases based on sample-dimensional changes are in agreement with more accurate measurements obtained by Archimedes method. In the latter case, measured densities for c- Y_2O_3 and m- Y_2O_3 are 5.02 g/cm^3 and 5.35 g/cm^3 , respectively.

Typical changes in dimensions of a disc-shaped sample when subjected to a reversible-phase transformation are shown in Figure 7.7. In a *forward transformation* at $8.0 \text{ GPa}/1000^\circ\text{C}/15 \text{ min}$, the sample dimensions change from $4.75 \text{ mm dia.} \times 3.20 \text{ mm}$ to about $4.82 \text{ mm dia.} \times 2.89 \text{ mm}$, Figure 7.7 (a) and (b), representing about 6-7% reduction in volume. On the other hand, in a *reverse transformation* at $1.0 \text{ GPa}/1000^\circ\text{C}/15 \text{ min}$, the same sample experiences volume restoration solely by increasing sample diameter, Figure 7.7 (b) and (c). Such behavior is repeatable from one experiment to the next, even for samples that undergo partial phase transformation, and irrespective of whether the initial grain size is coarse or fine. Repeating the reversible phase transformation leads to compounded dimensional changes, Figure 7.8.

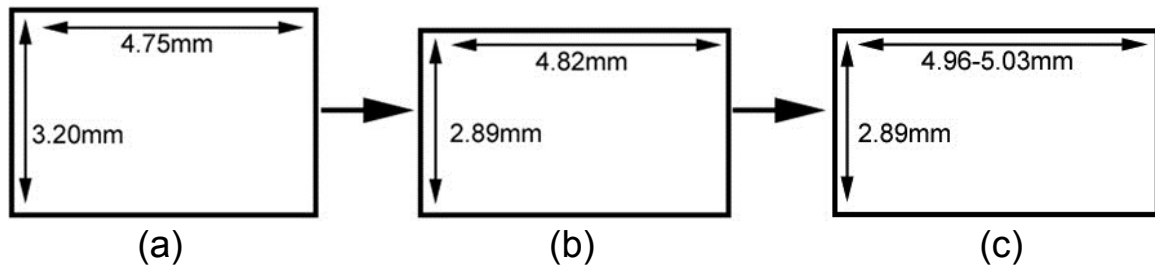


Figure 7.7 Diagram showing changes in sample dimensions due to a reversible-phase transformation: (a) as-received 1.5 μm grained starting material; (b) after forward transformation from $c\text{-Y}_2\text{O}_3$ to $m\text{-Y}_2\text{O}_3$ at 8.0 GPa/1000°C/15 min; and (c) after reverse transformation from $m\text{-Y}_2\text{O}_3$ to $c\text{-Y}_2\text{O}_3$ at 1.0 GPa/1000C/15 min.

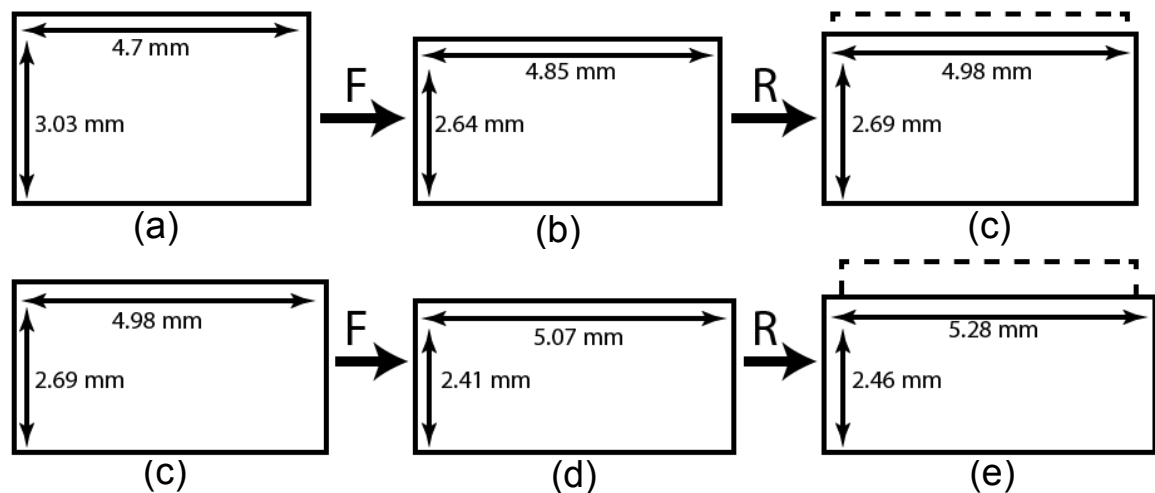


Figure 7.8 Diagram showing changes in sample dimensions due to repeated reversible-phase transformations: (a) as-received 300 μm grained starting material; (b) after forward transformation from $c\text{-Y}_2\text{O}_3$ to $m\text{-Y}_2\text{O}_3$ at 8.0 GPa/1000°C/15 min; (c) after reverse transformation from $m\text{-Y}_2\text{O}_3$ to $c\text{-Y}_2\text{O}_3$ at 1.0 GPa/1000C/15 min; (d) after a second forward transformation from $c\text{-Y}_2\text{O}_3$ to $m\text{-Y}_2\text{O}_3$ at 8.0 GPa/1000°C/15 min; (e) after a second reverse transformation from $m\text{-Y}_2\text{O}_3$ to $c\text{-Y}_2\text{O}_3$ at 1.0 GPa/1000C/15 min.

The observed dimensional changes are believed to be due to interaction of the applied force with the disc-shaped sample and its container, generating a quasi-isostatic pressure in the working volume, with the major force component parallel to the disc axis. Under these conditions, the decrease in sample volume

accompanying the forward cubic-to-monoclinic transformation occurs primarily by a reduction in sample height. The relatively small expansion in the radial direction is attributed to the slight bulging of the sample as it experiences shrinkage in the axial direction. On the other hand, the increase in sample volume accompanying the reverse monoclinic-to-cubic transformation is accommodated by an increase in its diameter, with no change in height. For both forward and reverse transformations, changes in sample dimensions must involve plastic flow of the graphite heater and its deformable-ceramic container.

In a typical two-step HPHT operation, Section 4.1.2, rapid application of the selected pressure is followed by relatively slow heating to the selected temperature. The phase transformation, therefore, is probably initiated before reaching the operating temperature, possibly affecting the final grain structure. To clarify the picture, one sample was first heated at 1.0 GPa to establish thermal equilibrium, while still in the cubic state, and then pressure is rapidly increased to 8.0 GPa to transform the material to the monoclinic state, i.e. the reverse of standard practice. Changes in sample dimensions using this modified procedure are similar to those shown in Figure 7.7.

7.3 Cubic-to-Monoclinic (Forward) Transformation

As discussed above, polycrystalline Y_2O_3 subjected to 8.0 GPa/1000°C/15 min is rapidly converted from its initial micro-grained cubic state into the nano-grained monoclinic state. Here, we describe the effects of varying pressure and holding time at 1000°C. As will be shown, significant changes in grain size and morphology are observed, particularly under pressures just above and below the critical phase transformation pressure (~2.5 GPa).

For example, Figure 7.9 shows major differences in grain size and morphology of Y_2O_3 upon annealing under pressure at 1000°C/240 min. At 1.0 GPa (below the critical transformation pressure), Figure 7.9 (a), the original equiaxed-grained c- Y_2O_3 structure is preserved, but coarsened by a factor of about 20. At 3.0 GPa (above the critical transformation pressure), a columnar-grained m- Y_2O_3 structure is formed, which displays coarsening to an extraordinary degree (about a factor of 1000). In this particular sample, the long holding time is sufficient to generate a columnar-grained structure that extends from top to bottom of the sample, Figure 7.9 (b); i.e. the transformation to columnar-grained m- Y_2O_3 is complete. As shown below, columnar grains are nucleated most frequently at the sample surface, and then propagate into the interior, eventually encompassing the entire sample volume, apparently driven by the pressure-induced monoclinic-to-cubic phase transformation at the columnar-grain tips.

The columnar-grained structure in transformed m- Y_2O_3 varies from one region of the sample to the next. In general, they are aligned parallel to the

applied force in the mid-sections of top and bottom surfaces of a transformed sample, Figure 7.9 (b), whereas at its corners and sides they are irregularly shaped. Apparently, this reflects a non-uniform distribution of pressure exerted on the disc-shaped sample, particularly when the phase transformation occurs, since it is accompanied by a major change in sample volume (density) that is concentrated at the columnar-grain tips. Thus, columnar-growth morphologies can be modified, which explains the curved and otherwise distorted columnar-grained structures observed near sample corners. Figure 7.10 shows the onset of $m\text{-Y}_2\text{O}_3$ nucleation and growth at the corners and edges of samples processed at 3.0 GPa/1000°C/15 and 60 mins.

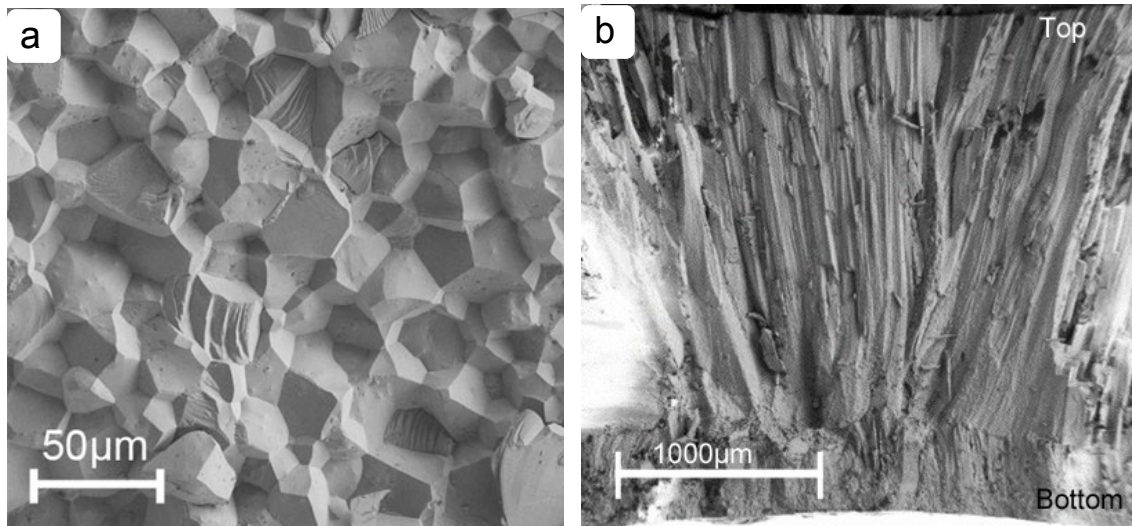


Figure 7.9 SEM images of fracture surfaces of samples processed at 1.0 and 3.0 GPa/1000°C/240 minutes, showing (a) equiaxed grains at 1.0 GPa in untransformed $c\text{-Y}_2\text{O}_3$, and (b) columnar grains at 3.0 GPa in transformed $m\text{-Y}_2\text{O}_3$.

Since the selected 1000°C processing temperature is $<0.5 T_m$, where T_m is the absolute melting temperature of Y_2O_3 , such rapid grain coarsening is surprising. Possible mechanisms are: (1) enhanced grain-boundary mobility due

to impurity segregation at grain boundaries (e.g. inward diffusion of carbon atoms from the graphite heater); and (2) pressure-induced grain boundary migration driven by modulus misfit between neighboring grains. Possibly both mechanisms operate in varying degrees, as discussed in Section 7.3.3.

No changes in grain size and morphology are observed in c- Y_2O_3 upon annealing in ambient-pressure air at 1000°C. Hence, the observed changes in grain size and morphology described above must be attributed to the influence of pressure on grain-boundary mobility, particularly at pressures near the critical transformation pressure.

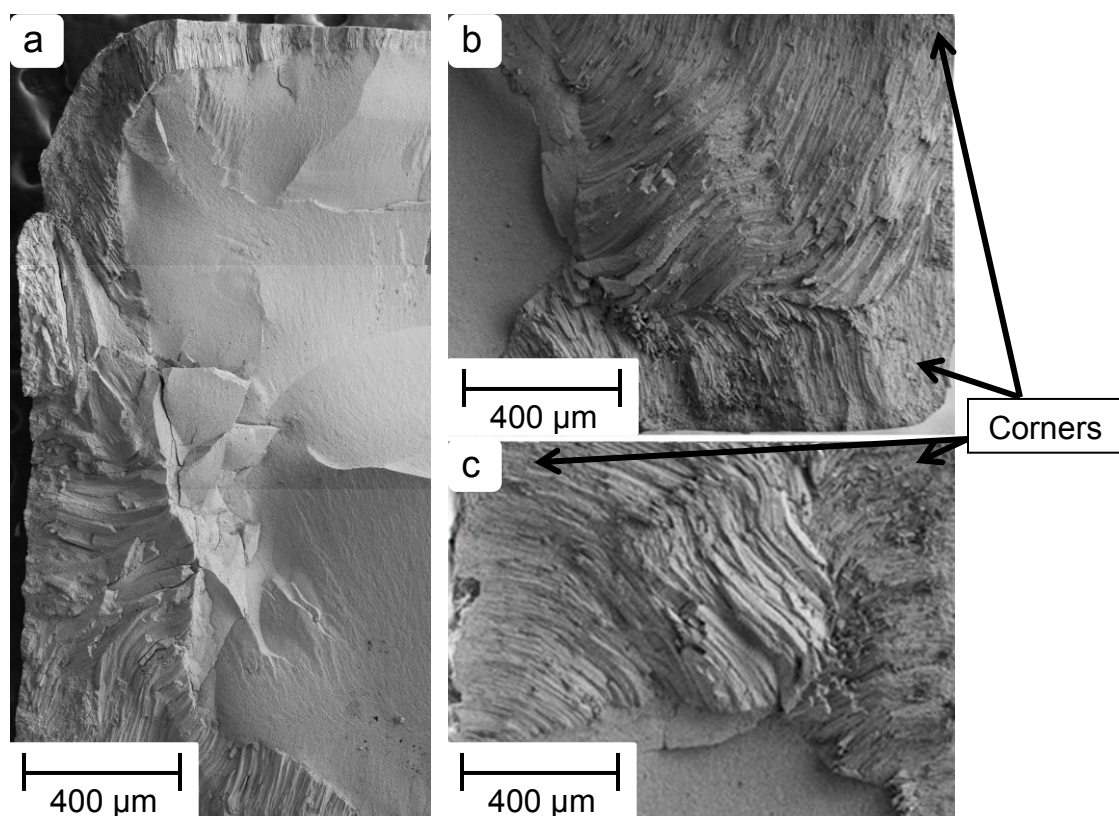


Figure 7.10 SEM image showing the onset of cubic-to-monoclinic conversion at the corners of samples processed at (a) 3.0 GPa/1000°C/15 mins; (b,c) 3.0 GPa/1000°C/60 mins.

7.3.1 Influence of Pressure

To determine the critical (minimum) pressure required to transform c-Y₂O₃ into m-Y₂O₃, several tests were performed at 1000°C for 15 min. Figure 7.11 shows XRD patterns for samples processed at 1.0, 2.5, and 3.0 GPa. The cubic-to-monoclinic phase transformation occurs at between 2.5 and 3.0 GPa, in agreement with the literature⁴⁰. However, as shown in Section 7.3.2, upon increasing holding time to 240 min at 2.5 GPa/1000°C, there is evidence for surface-localized transformation to m-Y₂O₃ in otherwise untransformed c-Y₂O₃. Hence, it is concluded that the critical c-to-m Y₂O₃ transformation pressure at 1000°C for practical holding times, is ~2.5 GPa.

Table 7-1 compares grain sizes of Y₂O₃ samples processed at various pressures at 1000°C/240 minutes. The average grain size of *transformed m-Y₂O₃* decreases from more than 1.0 μ m to less than 100 nm in the 3.0-8.0 GPa range. The largest variation in grain size is observed when comparing near-surface and interior regions of the sample. Table 7-1 also shows changes in hardness with HPHT-processing pressure, which will be discussed in Chapter 9.

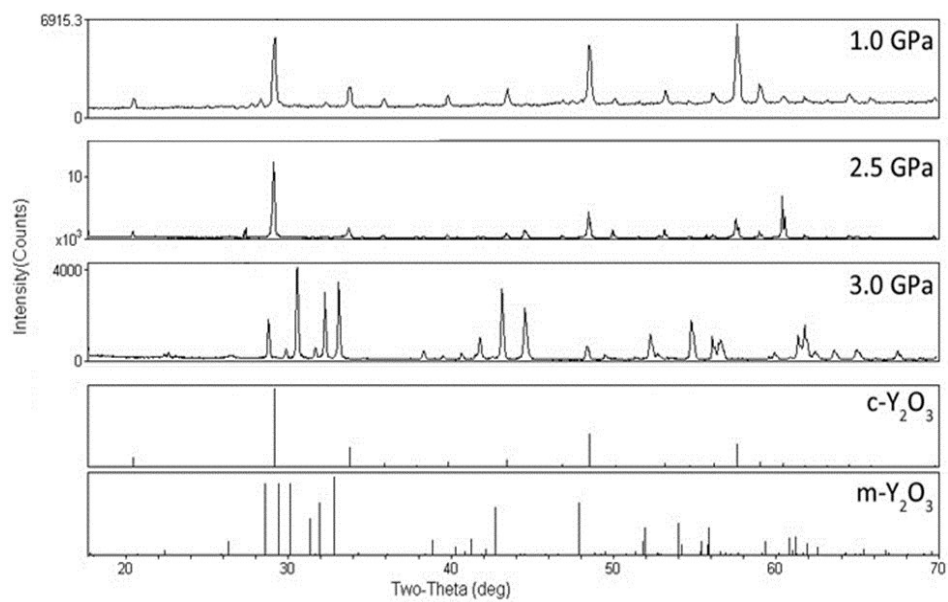


Figure 7.11 XRD spectra for samples processed at 1.0, 2.0, and 3.0 GPa/1000°C/15 min.

Table 7-1 Density and grain size of Y_2O_3 samples after processing at 1.0-8.0 GPa/1000°C/240 min.

Pressure (GPa)	Density (g/cm ³)	Phase	Grain Size (μm)
Ambient	5.02	Cubic	1.5
1.0	4.89	Cubic	1.5-30
2.5	4.92	Cubic	40-60
3.0	5.27	Monoclinic	*20-1500+
4.0	5.35	Monoclinic	10 - 100
5.0	5.33	Monoclinic	0.05-4
6.5	5.41	Monoclinic	0.05-0.5
8.0	5.33	Monoclinic	0.05

*Smaller grains are located near the surface, with interior grains >1mm in length.

7.3.2 Incomplete Phase Transformation

SEM examination of a fractured sample, Figure 7.12, after HPHT processing at 2.5 GPa/1000°C/240 min, indicates that the c- to m- Y_2O_3 transformation is surface initiated. Confirmation is provided by depth-profile XRD analysis, i.e. by taking XRD patterns after removing successive layers of material by polishing. *The as-processed sample*, Figure 7.13 (a), shows characteristic XRD peaks for the m- Y_2O_3 phase. After polishing to a depth of 30 μm , peaks matching c- Y_2O_3 appear, Figure 7.13 (b), with the m- Y_2O_3 peaks reduced in intensity. At a depth of about 80 μm , Figure 7.13 (c), only c- Y_2O_3 peaks are present.

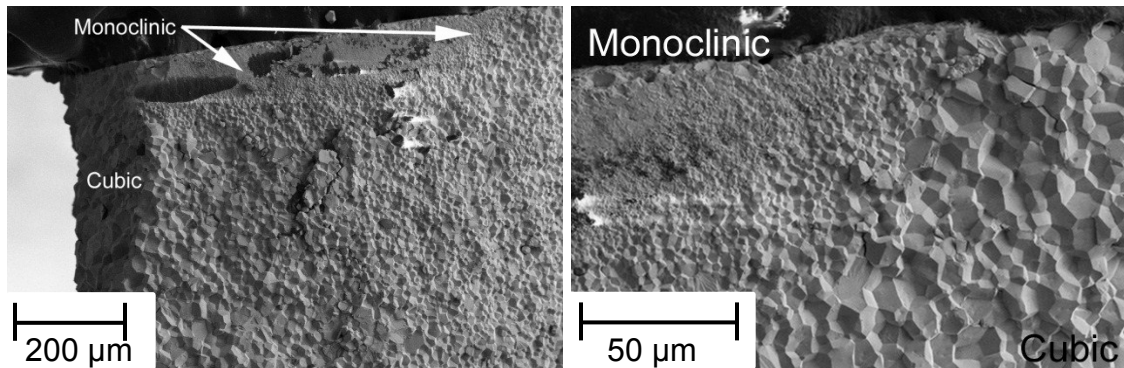


Figure 7.12 SEM images of the fracture surface of a sample processed at 2.5 GPa/1000°C/240 min, showing a thin surface layer of transformed m- Y_2O_3 phase, and an interior of untransformed c- Y_2O_3 phase.

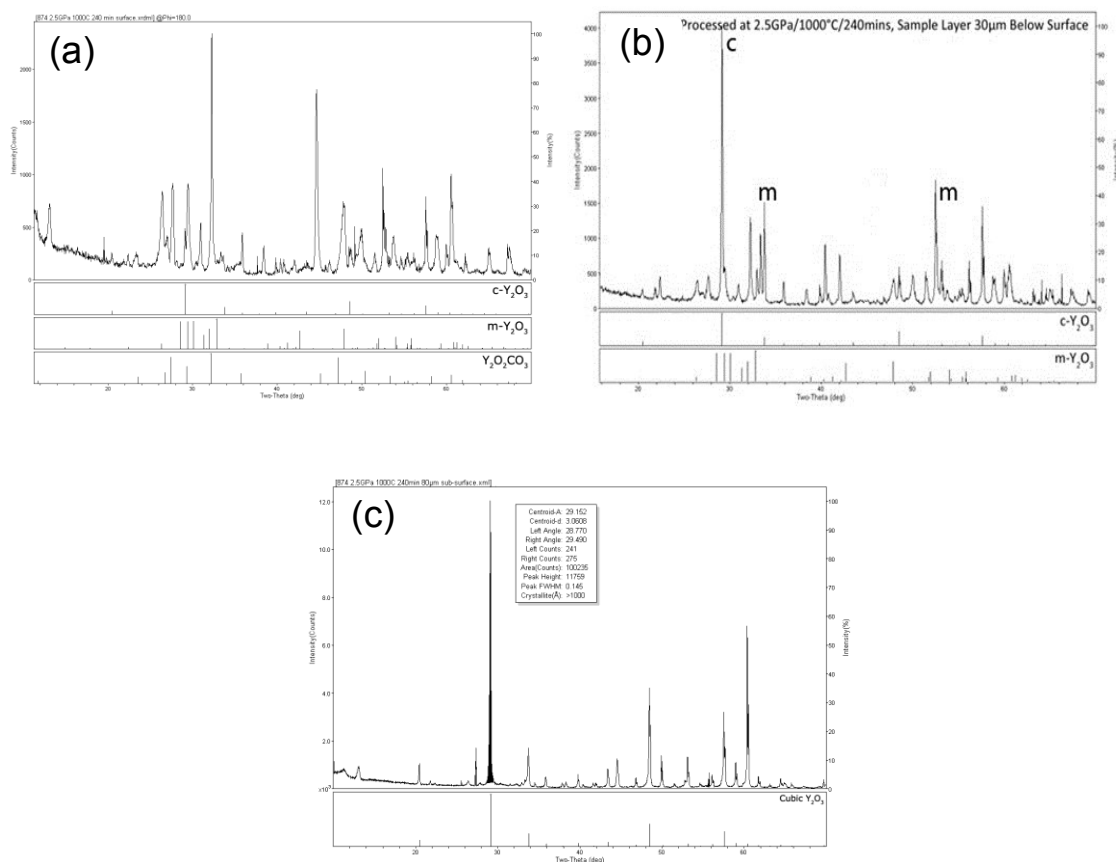


Figure 7.13 XRD analysis of sample processed at 2.5 GPa/1000°C/240 min: (a) m-Y₂O₃ surface layer; (b) appearance of c-Y₂O₃ at 30-μm depth below the surface; and (c) c-Y₂O₃ at 80-μm depth below the surface.

In Figure 7.12, the grain size of the untransformed c-Y₂O₃ is about 20 μm, which is at the lower end of the grain-size range presented in Table 7-1. Even so, this value is still an order of magnitude larger than the 1.5-μm grain size of the starting material. Density measurements show no detectable increase in sample density, apparently because the volume fraction of the higher density m-Y₂O₃ phase is small.

It is noteworthy that the surface-localized m-Y₂O₃ phase formed at 2.5 GPa has a fine equiaxed grain structure, in marked contrast to the coarse columnar-grain structure observed in a sample completely transformed at 3.0

GPa, Figure 7.9 (b). The significant difference in grain size and growth behavior at 2.5 GPa compared to what is observed at 3.0 GPa is attributed to a relaxation of loading and stress that results from the decrease in volume associated with the localized c-Y₂O₃ to m-Y₂O₃ transformation.

Sample distortion is another feature of an incompletely transformed sample. Typically, the sample retains its original diameter in one direction, but is elongated in a perpendicular direction. This distortional effect may be ascribed to different degrees of surface-localized phase transformation in different regions of the sample.

The observed cubic-to-monoclinic phase transformation at ~2.5 GPa in bulk polycrystalline c-Y₂O₃ is in agreement with previous work on *powders and very small samples* (Section 2.5). However, this is the first such study on relatively large-sized samples, thereby enabling observations on partial versus complete phase transformations, and associated transformation mechanisms. Moreover, the availability of larger samples has allowed measurements of changes in hardness under varying processing conditions. Other properties measurements will be made in future work, using optimally-processed based on the findings of this investigation.

7.3.3 Transformation Mechanism

Complete transformation from cubic-to-monoclinic Y₂O₃ is observed for holding time <5 sec at 8.0 GPa/1000°C. Since there is no detectable incubation period, this suggests a displacive transformation, where atomic positions are shifted in a *diffusionless process*. On the other hand, under lower pressures,

approaching the critical transformation pressure, the phase transformation is initiated at the surface and propagates into the interior, clearly indicating a *diffusion-controlled process*. Figure 7.14 shows striking examples of an incomplete phase transformation, after 15 min holding time at 3.0 GPa, where a coarse-grained columnar-grained monoclinic structure, initiated at the sample surface, is shown at an intermediate stage in its growth into the interior. Another example for the same sample, Figure 7.15, shows a progressive change in grain structure with increasing distance from the surface, where nucleation and growth is initiated. Near the surface, the grain structure is not well organized, but with increasing distance from the surface, a well-developed columnar-grained structure emerges, accompanied by some grain coarsening.

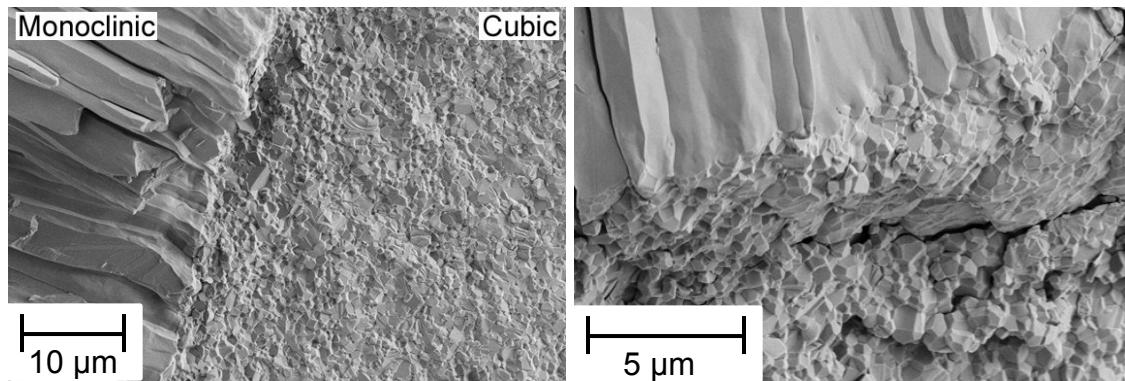


Figure 7.14 SEM images of a fine-grained sample, after processing at 3.0 GPa/1000°C/15 min, showing growth of columnar-grained $m\text{-Y}_2\text{O}_3$ into untransformed equiaxed-grained $c\text{-Y}_2\text{O}_3$.

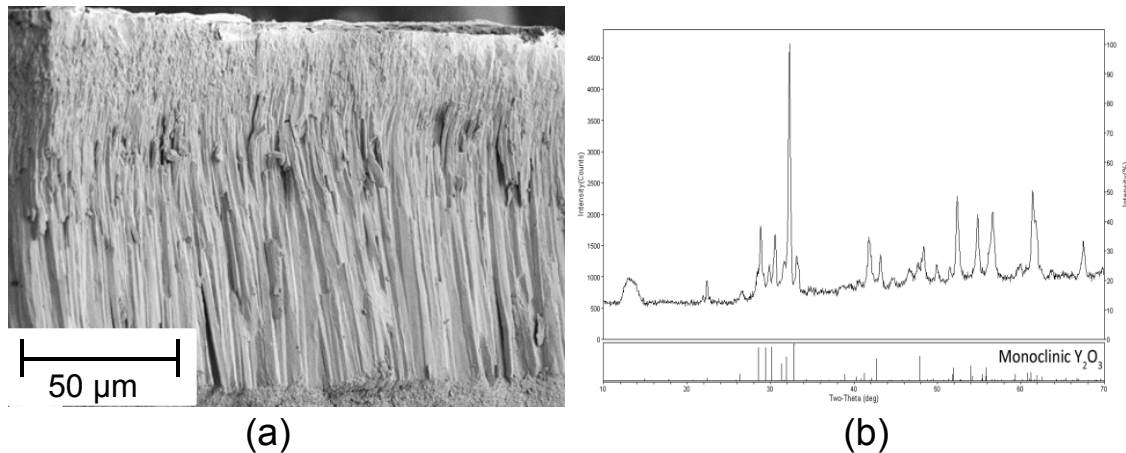


Figure 7.15 (a) SEM image of a fine-grained sample, after processing at 3.0 GPa/1000°C/60 min, showing a progressive change in grain size and morphology with increasing distance from the surface. Columnar-grained $m\text{-Y}_2\text{O}_3$ evidently grows at the expense of the initial fine-grained $c\text{-Y}_2\text{O}_3$, with a clear texturing effect evident via XRD analysis (b).

This is explained in terms of competitive growth between neighboring grains as they propagate into the interior, such that only the fastest-growing grains prevail, crowding out less favorably oriented grains. Thus, a coarse columnar-grained $m\text{-Y}_2\text{O}_3$ structure is realized that has a well-defined (302) texture, Figure 7.15 (b).

Figure 7.9 (b) shows that increasing the holding time to 240 min at 3.0 GPa/1000°C results in complete conversion to coarse columnar-grained $m\text{-Y}_2\text{O}_3$; in other words, the cubic-to-monoclinic phase transformation is complete. Such behavior is typical of samples processed at pressures <5 GPa, but the holding time to complete the transformation process decreases with increasing pressure in the 2.5 -5.0 GPa range.

How can these two apparently distinct phase-transformation mechanisms be reconciled? One possibility is that the pressure-induced phase transformation

is *pseudo-martensitic*, as discussed in literature⁷⁷, for a stress-dependent olivine-spinel transformation in fayalite which could not be explained in terms of a pure diffusional or diffusionless mechanism. The authors conclude that a hybrid transformation mechanism is involved, where cation rearrangement is not synchronized with anion displacements.

Another possibility is that the c- to m-Y₂O₃ transformation under all conditions is diffusion-controlled, involving nucleation and growth of the monoclinic phase in the host cubic phase. At 3.0 GPa, which is just above the critical phase transformation pressure, nucleation rate is low and growth rate high, thus enabling a coarse columnar-grained m-Y₂O₃ structure to be developed. Under the highest pressure of 8.0 GPa, nucleation rate is high and growth rate low, hence the appearance of an equiaxed nano-grained structure. This model is consistent with the progressive reduction in grain size with increasing pressure in the 3.0-8.0 GPa range, Table 7-1.

We conclude, therefore, that the observed cubic-to-monoclinic transformation in polycrystalline Y₂O₃ is best understood in terms of a nucleation and growth mechanism, with structural consequences that depend on the applied pressure. At 3.0 GPa/1000°C the forward phase transformation is sluggish, yielding a micro-grained columnar structure, whereas at 8.0 GPa/1000°C the transformation is fast, resulting in a nano-grained equiaxed structure. At intermediate pressures, the grain structures display some of the features of these two extreme processing conditions, as will now be shown.

At 4.0 GPa/1000°C, Figure 7.16 (a), heterogeneous nucleation and growth of m-Y₂O₃ columnar grains occurs at the sample surface, while homogeneous nucleation and growth of m-Y₂O₃ grains occurs in the sample interior, with many of the grains having an elongated or elliptical shape, and with their major axis parallel to that of the surface-localized columnar grains. This is explicable in terms of a higher nucleation rate of m-Y₂O₃ grains in the sample interior (homogeneous nucleation), relative to that at 3.0 GPa where no such interior nucleation occurs. Thus, the head start in the growth of surface-nucleated columnar grains (heterogeneous nucleation) does not dominate the entire m-Y₂O₃ transformation process, as it does at 3.0 GPa. At 5.0 GPa/1000°C, Figure 7.16 (b), the nucleation rate in the sample interior is higher, such that much less growth occurs, resulting in a finer and less elongated m-Y₂O₃ grain structure relative to that at 4.0 GPa. The grain structure at 6.5 GPa, Figure 7.16 (c), is even finer still and more equiaxed in the interior, more like that at 8.0 GPa, but with a columnar structure at the surface because of the reduced nucleation rate at the lower pressure.

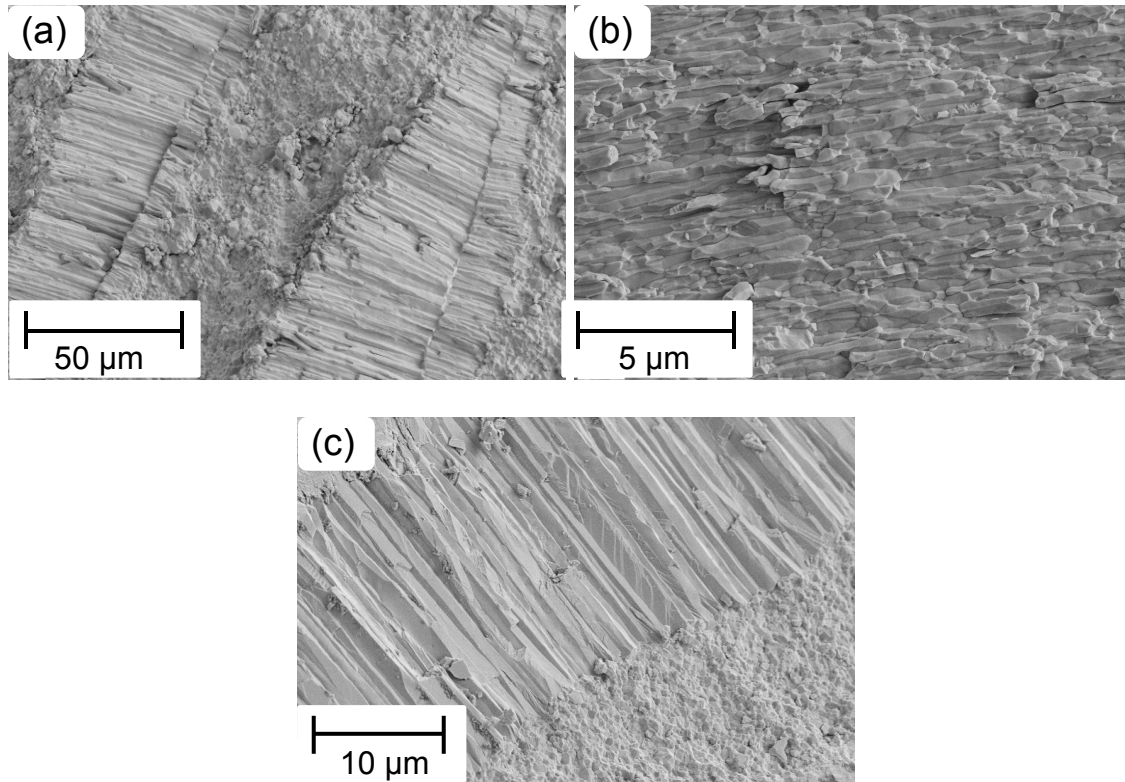


Figure 7.16 SEM images of elongated grains in samples transformed to the monoclinic state at (a) 4.0 GPa/1000°C/ 240 mins; (b) 5.0 GPa/1000°C/240 mins; (c) 6.5 GPa/1000°C/240 mins.

7.3.4 Crystal Growth

Figure 7.14 shows that processing (annealing under high pressure) fine-grained c-Y₂O₃ at 3.0 GPa/1000°C/15 min (just above the critical phase transformation pressure at 2.5 GPa) generates a coarse columnar-grained m-Y₂O₃ structure, which is initiated at the sample surface, and propagates uniformly into the sample interior. With a sufficiently long holding time, the entire sample is transformed into directionally-crystallized m-Y₂O₃, comprising columnar grains that have grown inwards from opposite directions, Figure 7.9 (b).

The driving force for such directional crystallization is believed to have two components: (1) reduction in total grain-boundary energy in transforming fine

equiaxed-grained c-Y₂O₃ into much coarser columnar-grained m-Y₂O₃; and (2) enhanced driving force for columnar-grain growth provided by a pressure-induced phase transformation at the tips of the growing columnar grains. The latter is believed to be the principal rate-controlling mechanism driving the columnar-grained interface forward.

This behavior suggests a method to grow large columnar-grained structures by restricting grain nucleation to a few favorable surface sites. This may be done, for example, by introducing a few indentations into the sample surface, such that the resulting stress concentrations induce early nucleation of new recrystallized grains, providing them with a head start in subsequent competitive growth into the sample interior. It may also be possible to grow a *single crystal (monocrystal)* of m-Y₂O₃ under appropriate HPHT-processing conditions, as discussed in Chapter 10.

7.3.5 Conclusions

- Processing at 8.0 GPa/1000°C drives a very rapid cubic-to-monoclinic phase transformation, resulting in an equiaxed nano-grained structure. The transformation mechanism involves prolific nucleation of nanoparticles of the monoclinic phase within the initial coarse-grained cubic phase, accompanied by minimal grain growth.
- Processing at 5.0-6.5 GPa/1000°C yields a monoclinic structure, but with the sample *interior* composed of *equiaxed* and *slightly elongated* nano-grains, and its surface composed of *columnar* micro-grains. The coarse columnar-grained structure (each grain typically 5 μm in width x 10-30 μm in length) is susceptible to *intergranular fracture*.
- Processing at 3.0 GPa/1000°C generates a monoclinic structure, but the resulting columnar-grained structure is extremely coarse (typically of mm-dimensions), and highly susceptible to intergranular fracture. As discussed in Chapter 8, segregation of impurities, such as carbon from the graphite heater, may be a contributing factor to embrittlement of the columnar-grain boundaries.
- Processing in the 3.0-8.0 GPa range involves a significant decrease in monoclinic grain size, and a striking change in grain morphology and scale, as indicated above. In all cases, it is concluded that the cubic-to-monoclinic transformation occurs via a diffusion-controlled nucleation and growth process.

- At 3.0 GPa, *nucleation rate* is *low* and *growth rate* *high*, thus forming a very coarse columnar-grained structure, typically initiating at the surface of a sample and propagating into its interior. At 8.0 GPa, *nucleation rate* is *high* and *growth rate* *low*, hence the appearance of an equiaxed nano-grained structure. With increasing pressure in the 3.0-8.0 GPa, there is a progressive change in grain structure from coarse columnar grains to fine equiaxed grains, culminating at 8.0 GPa in the appearance of a *uniform* nano-grained structure throughout the sample.
- XRD analysis of a typical columnar-grained structure reveals that all the grains share a common cube axis in the longitudinal direction, but are rotated with respect to one another in the transverse direction. As noted above, the smooth faceted surfaces of the columnar grains are prone to fracture.
- Annealing fine-grained c-Y₂O₃ at 1.0-2.5 GPa/1000°C causes coarsening of its equiaxed-grain structure, even though the annealing temperature is $<0.5 T_m$, where T_m is the absolute melting point of the material. This behavior correlates with enrichment of grain boundaries of the material with carbon-rich species by grain-boundary diffusion. For example, an increase in holding time under HPHT-processing conditions results in an increase in depth of penetration along grain boundaries of carbon-containing species, and a corresponding increase in grain size. Thus, it appears that grain-boundary mobility is affected by grain-boundary segregation of carbon-rich species, although the mechanism is not clear.

- A possible mechanism is the formation of an incipient oxy-carbonate phase (possibly even a monolayer) that lowers the effective melting point of a grain boundary, thus promoting grain-boundary mobility. Another possible mechanism is an enhanced driving force for grain-boundary migration by modulus-mismatch stresses developed between neighboring grains under a near-isostatic pressure.
- The critical transformation pressure to induce a forward-phase transformation from cubic-to-monoclinic Y_2O_3 is ~ 2.5 GPa at 1000°C . Under a pressure just above the critical pressure, transformation to m- Y_2O_3 is initiated at the sample surface and then propagates into the sample interior, accompanied by *striking changes in grain size and morphology*.
- Annealing fine-grained c- Y_2O_3 at 3.0 GPa/ 1000°C generates a recrystallized grain structure, comprising a bundle of textured m- Y_2O_3 grains that propagates uniformly from sample surface to interior. The columnar-grained structure has a well-defined (302) texture, resulting from competitive growth between neighboring grains with increasing distance from the surface.
- The driving force for columnar-grain growth has two components: (1) reduction in total grain-boundary energy in transforming fine equiaxed-grained c- Y_2O_3 into much coarser columnar-grained m- Y_2O_3 ; and (2) transformation from c- Y_2O_3 phase to the higher density m- Y_2O_3 phase at the tips of the growing columnar grains. The latter is believed to be the principal rate-controlling mechanism driving the columnar-grained interface forward.

- Based on these considerations, low temperature growth of a single crystal of the high pressure m-Y₂O₃ phase seems feasible, as discussed in Chapter 10.

7.4 Monoclinic-to-Cubic (Reverse) Transformation

Polycrystalline Y_2O_3 , HPHT processed at 8.0 GPa/1000°C/15 min, is transformed from its initial *micro-grained* cubic state into the *nano-grained* monoclinic state, as discussed in Section 7.3. Here, we describe the effects of subjecting nano-grained monoclinic samples (all initially processed as above) to a reverse monoclinic-to-cubic transformation at 1.0 GPa/600-1000°C/15-240 min, i.e. *at the same pressure for varying temperature and holding time*.

For reference purposes, Table 7-2 summarizes data on changes in physical properties of polycrystalline Y_2O_3 (1.5 μm grain size), when subjected to a reversible-phase transformation. The final nano-grained c- Y_2O_3 displays an increase in hardness relative to that of the original coarse-grained c- Y_2O_3 . Another effect is a change in visible-light transmission displayed by the reversibly-transformed material. Transmission appears highest at sample edges and corners, corresponding to regions of exaggerated grain coarsening, and lowest in the interior where the nano-scale material is opaque and light grey in appearance. The poor transmission of the nano-scale material is attributed to scattering across the higher density of grain boundaries.

Table 7-2 Comparison of physical properties of reference samples

Processing conditions	Phase	Density (g/cm ³)	ΔV	Grain size (nm)	Hardness (GPa)
Starting material	c-Y ₂ O ₃	5.02	0	1.5 μ m	6.8
(Forward transformed) 8.0 GPa/1000°C/15 min	m-Y ₂ O ₃	5.35	-6%	40 nm	7.63
(Reverse transformed) 1.0 GPa/1000°C/15 min	c-Y ₂ O ₃	4.94	+6%	40 nm	7.46

7.4.1 Influence of Temperature and Holding Time

To determine the influence of temperature and holding time on the reverse transformation, all samples were first subjected to a forward transformation at 8.0 GPa/1000°C/15 mins, and then re-processed at 1.0 GPa/600-1000°C/15-240 min.

After re-processing at 1.0 GPa/1000°C/15 min, an increase in sample density, Table 7-3, supported by XRD, shows that the reverse monoclinic-to-cubic transformation is essentially complete, although TEM analysis indicates a small amount of residual monoclinic phase. In contrast, at lower transformation temperatures, much longer holding times are needed to complete the reverse phase transformation. Even at 700°C, however, it appears that complete transformation is achievable if given a sufficiently long holding time.

Table 7-3 Monoclinic-to-cubic Y_2O_3 transformation for samples processed at 1.0 GPa for varying temperature and holding time.

Temperature (°C)	Holding Time (min)	Density (g/cm ³)	Conversion to c- Y_2O_3 (%)
1000	15	4.94	100%
800	60	5.19	49%
700	60	5.33	6%
700	240	5.22	39%
600	240	5.34	3%

While uniform bulk transformation occurs at 1000°C, at lower temperatures inward growth from the sample surface is the characteristic transformational mode. The result is a *core-shell structure*, where the sample interior (core) is *untransformed-monoclinic* phase, and the sample surface (shell) is *transformed-cubic* phase. Due to the volume mismatch between transformed shell and untransformed core, circumferential hoop stresses (expansive in nature) are developed at the interphase interface, resulting in decohesion or fracture. The effect is illustrated in Figure 7.17 for a sample subjected to a reverse transformation at 1.0 GPa/800°C/60 min. A low magnification optical micrograph of a polished surface, Figure 7.17 (a), shows that the fracture path is at a fixed depth below the surface of the disc-shaped sample. An electron micrograph of the same sample after being fractured, Figure 7.17 (b), indicates that there is an abrupt change in structure upon crossing the fractured interface. In Figure 7.17 (a), the outer surface layer (shell) displays a more granular

appearance than the interior (core), and upon closer examination it is determined that the effect is due to grain pull-out during polishing.

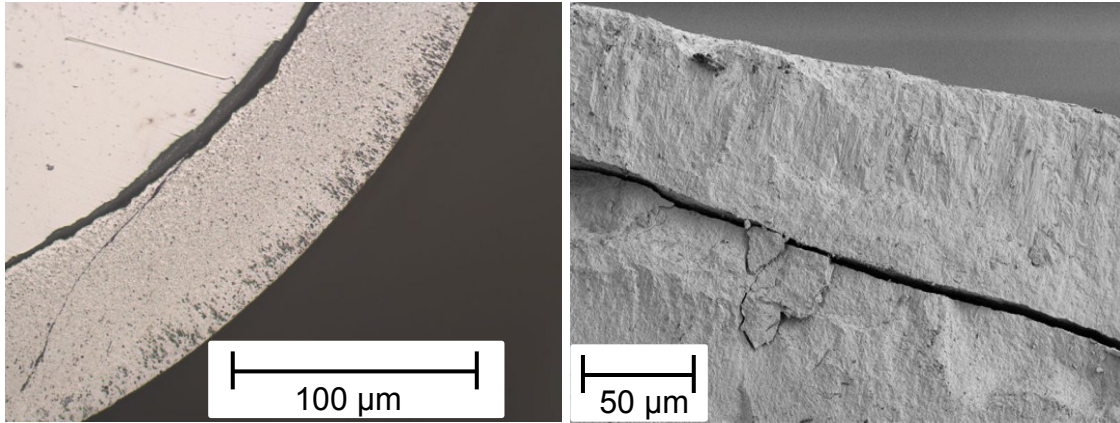


Figure 7.17 Optical micrographs of a partially transformed sample, showing decohesion between untransformed-monoclinic core and transformed-cubic shell: (a) polished mid-section showing fracture path along a curved interface of the sample ; and (b) fractured mid-section showing abrupt change in grain structure upon crossing the fractured interface.

The hoop stress developed between the transformed-cubic shell and the untransformed-monoclinic core tends to lift the shell off its core. However, it is unlikely that interface decohesion occurs under pressure, but upon unloading it seems unavoidable. This draws attention to the importance of performing the reverse transformation under pressure, since without it the sample disintegrates, as observed in a post-annealing experiment conducted at ambient pressure.

An incompletely-transformed sample tends to exhibit a uniform core-shell structure, as discussed above. However, more complex structural modifications occur in regions of stress concentration, such as at edges and corners of a sample. This effect is complicated by interactions between sample and graphitic-carbon heater, as discussed in Chapter 8.

7.4.2 Mixed-Phase Nanocomposite

Although the cubic phase is thermodynamically favored at ambient pressure and temperature, there exists a kinetic threshold below which the reverse monoclinic-to-cubic transformation does not occur, regardless of processing duration (holding time). For example, re-processing nano-grained m-Y₂O₃ at 800°C under a pressure of 1.0-2.0 GPa ensures a relatively slow phase-transformation rate, so that phase decomposition can be arrested at any stage without risking structural failure. The result is a mixed cubic/monoclinic nanocomposite structure, which may be described as a *mixed-phase nanocomposite*. Since the constituent phases have the same Y₂O₃ composition, this novel structure may also be described as a *self-nanocomposite*.

The concept of a mixed-phase nanocomposite has potentially important implications for other types of ceramic materials, particularly those that experience a temperature-dependent phase transformation under ambient-pressure conditions, such as ZrO₂ and partially-stabilized ZrO₂. For example, control of a reversible phase transformation in pure ZrO₂ (e.g. tetragonal-monoclinic-tetragonal) under pressure, including repeated cycling through the transformation temperature, should be possible, without causing sample disintegration, thereby forming a self-nanocomposite structure. Having created such a nanocomposite, a brief post-annealing treatment at a higher temperature under pressure should allow any internal stresses (e.g. interphase-interface stresses) to be relaxed via a creep-deformation mechanism, resulting in a

relatively stress-free self-nanocomposite structure. However, the introduction of thermal expansion misfit stresses during cool-down seems unavoidable.

A monoclinic Y_2O_3 sample processed at 1.0 GPa/700°C/240 min experiences about 39% conversion to the cubic phase. The interior structure appears milky-white in color, and is almost translucent. In contrast, as-received cubic Y_2O_3 samples are transparent and transformed monoclinic Y_2O_3 samples are opaque gray. Normally, a fully-transformed monoclinic Y_2O_3 structure appears gray and non-transparent due to crystalline anisotropy, and the presence of internal stresses introduced during processing. The milky-white appearance may be attributed to a mixed transparent cubic and opaque monoclinic Y_2O_3 nanocomposite structure, i.e. a mixed-phase nanocomposite structure.

Another recent Rutgers study^{78,79} has shown that the cubic, monoclinic, and hexagonal Y_2O_3 phases can co-exist in the presence of a fourth component, MgO, when micro-volumes of 0.5MgO-0.5 Y_2O_3 are treated in a diamond anvil cell at 7.0 GPa and 1000°C. The formation of this multi-phase nanocomposite is believed to be largely dependent on the dissolution of Y^{3+} ions in MgO, evident from 0.69% volumetric expansion of the MgO unit cell, which suppresses the reverse hexagonal-to-monoclinic and monoclinic-to-cubic Y_2O_3 phase transitions.

7.4.3 XRD vs. Raman Analysis

XRD analysis is an invaluable tool for general phase identification purposes, but the technique is of limited value in identifying near-surface phase distributions, since it can only provide information averaged over an entire

sample surface. Raman analysis provides a useful complementary technique, because it offers the ability to analyze phase changes with increasing depth in the sample, as well as identifying phases in discrete sample areas.

To compare the effectiveness of these two analytical techniques, a sample showing a surface layer of fully-transformed cubic phase, and an interior of partially-transformed cubic phase was examined. The starting material was prepared using a standard procedure: *complete* forward cubic-to-monoclinic transformation at 8.0 GPa/1000°C/15 min followed by *partial* reverse monoclinic-to-cubic transformation at 1.0 GPa/700°C/240 min. At such a low reverse-transformation temperature, a core-shell structure is developed. XRD analysis confirms that only cubic and monoclinic phases are present, but provides no detailed information on the distribution of phases with increasing depth in the sample. However, using standard Raman spectra for reference purposes, Figure 7.18, this is readily accomplished via line profile analysis conducted on a well-polished cross-section of sample, Figure 7.19.

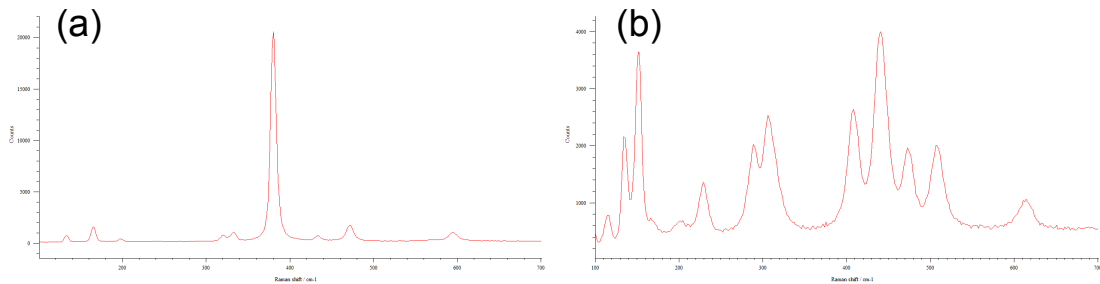


Figure 7.18 Raman spectra for: (a) cubic Y_2O_3 ; and (b) monoclinic Y_2O_3 . Full spectra are not shown, since there are no additional peaks.

A multi-sampling Raman line-map was taken across the mid-section of a polished sample of partially-transformed material. As shown in Figure 7.19, the

Raman spectra reveals a distinct trend in phase decomposition with increasing depth, starting with reverse transformed cubic- Y_2O_3 at the sample surface. The data shows that surface-nucleated cubic phase propagates inwards from the sample surface, while cubic nanoparticles nucleate and grow simultaneously, albeit at a slower rate, within the interior or bulk of the material. An interior region about 420- μm below the sample surface exhibits no further change in phase composition, indicating that a uniform mixture of the two phases throughout the bulk material has been attained, thus forming a novel *duplex-phase or self-nanocomposite structure*.

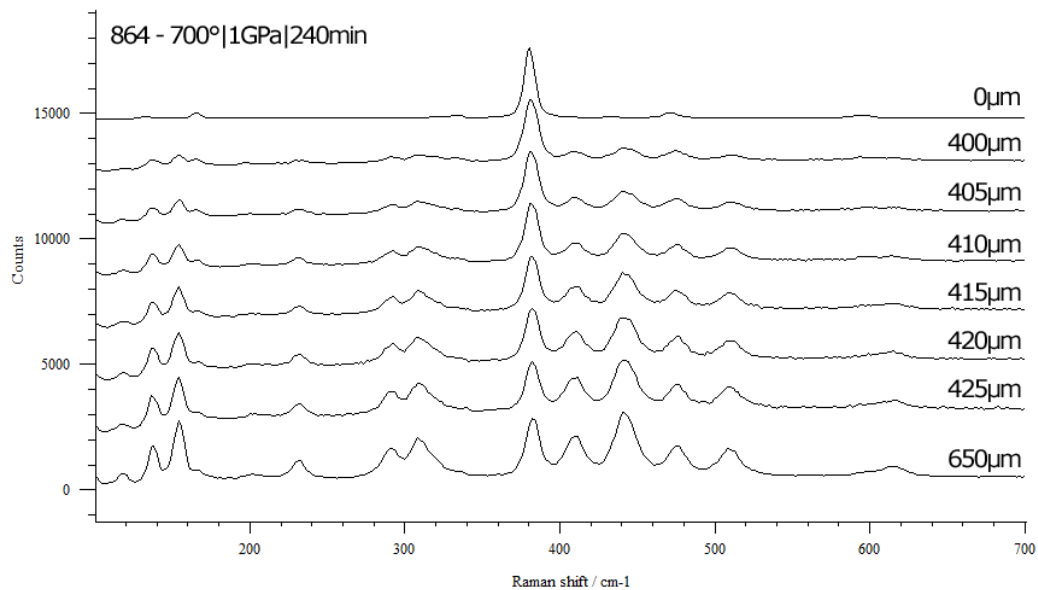


Figure 7.19 Line-profile Raman analysis (633-nm source) of a sample that had been partially transformed from monoclinic-to-cubic at 1.0 GPa/700°C/240 min.

In several samples, similar core-shell structures have been observed, but the distinguishing feature here is the ability to adjust the temperature for the reverse transformation to generate a completely uniform self-nanocomposite. Optimal processing parameters to achieve the finest possible nanocomposite

structure need to be determined, since this is a means to optimize mechanical and optical properties of the composite material. Hardness testing of the partially transformed cubic/monoclinic nanocomposite, Section 9.3, shows higher hardness compared to as-received and reversibly-transformed c-Y₂O₃ samples.

The possibility of a self-nanocomposite had been considered in early experiments, but deemed unlikely, since the volume change accompanying the phase decomposition would develop internal stresses that would be sufficient to break-up the sample upon unloading from high pressure. However, the results presented above show that this is not the case. A favorable factor may be the ultrafine-grain structure (~40 nm) of the nanocomposite allowing interphase-stress relaxation via grain-boundary sliding during HPHT processing.

7.4.4 Conclusions

- The main conclusion to be drawn from these observations is that the reverse monoclinic-to-cubic Y₂O₃ transformation at 1.0 GPa/700-1000°C is governed by nucleation and growth, with sluggish kinetics responsible for incomplete or partial transformation at the lower temperatures.
- Homogeneous nucleation and growth of the cubic phase occurs at 1.0 GPa/1000°C, resulting in a uniform equiaxed-grain structure.
- Heterogeneous nucleation and growth of the cubic phase occurs at 1.0 GPa/700-800°C, resulting in slightly elongated grains at the surfaces and equiaxed grains in the interior.

- Partially-transformed material, where a distinct core-shell structure (monoclinic-cubic) is developed, experiences fracture at the core-shell interface, due to internal stresses arising from shell expansion during the phase transformation. It is unlikely that the effect occurs during processing under pressure, but seems to be unavoidable upon unloading after processing.
- Fully-transformed material does not experience fracture upon unloading, since any residual stresses in the transformed-cubic phase are uniformly distributed throughout the material.
- Raman line-profile analysis is a useful tool to determine changes in phase decomposition with increasing depth in partially-transformed material.
- A novel mixed-phase or self-nanocomposite structure has been found in partially reverse-transformed Y_2O_3 , which could exert a strong influence on properties and performance.
- This new processing methodology has opened opportunities for processing nanocomposites of other technically-important ceramics, such as ZrO_2 and partially-stabilized ZrO_2 .

8 INTERACTIONS WITH CARBON HEATER

In Chapter 7, the major microstructural consequences of reversibly-transforming polycrystalline Y_2O_3 under HPHT conditions are described. In particular, an optimized procedure is presented for transforming polycrystalline c- Y_2O_3 directly into the nanostructured state, including single-phase (nanocrystalline) c- Y_2O_3 , and mixed-phase (nanocomposite) c- Y_2O_3 /m- Y_2O_3 . Here, we consider interactions between Y_2O_3 sample and its carbon heater, which are in intimate contact with one another at all stages in HPHT processing.

Samples of coarse-grained (300 μm) material are prone to *intergranular fracture*, both in as-received and HPHT-processed conditions, due to *weakening of grain boundaries* by impurity segregation. In contrast, samples of fine-grained (1.5 μm) material experience transgranular fracture, due to the high purity (optical grade) of the material, produced by sinter-HIP at Raytheon IDS. Even so, after HPHT processing, carbon segregation at grain boundaries has been observed, particularly in near-surface regions of the processed material due to sample/heater interaction; specifically, diffusion of carbon from the heater into the grain boundaries of the material.

In general, the tendency for a disc-shaped sample to undergo intergranular fracture during processing is exacerbated at its edges and corners, owing to the complex nature of internal stresses at these locations. On the other hand, mid-sections of a sample experience more uniform pressurization, so that observed phase transformations are reproducible from one sample to the next. Hence, observations made in the mid-section regions of HPHT-processed

samples became the primary focus of the research. In fact, it is from these observations that the main conclusions are drawn with respect to operative phase-transformation mechanisms and kinetics.

In what follows, two mechanisms of sample/heater interactions are considered: (1) *major carbon ingress into cracked grain boundaries by an infiltration mechanism; and (2) minor carbon ingress into uncracked grain boundaries by a diffusion mechanism.* As will be shown, vapor transport of carbon species from source (heater) to sink (sample) can account for most if not all of the observations. In a concluding section on crystal growth, *a temperature gradient-controlled recrystallization process* is described to grow single crystals of $m\text{-Y}_2\text{O}_3$, and other high-pressure phases.

8.1 Carbon Infiltration

When intergranular fracture occurs during HPHT processing, carbon from the heater *infiltrates into crack* openings to a remarkable extent. An example for a coarse-grained (300 μm) sample is shown in Figure 8.1, after a reversible transformation at 1000°C. The infiltrated carbon (dark contrast) decorates intergranular-fractured grain boundaries A and B, but not a transgranular-fractured grain boundary C.

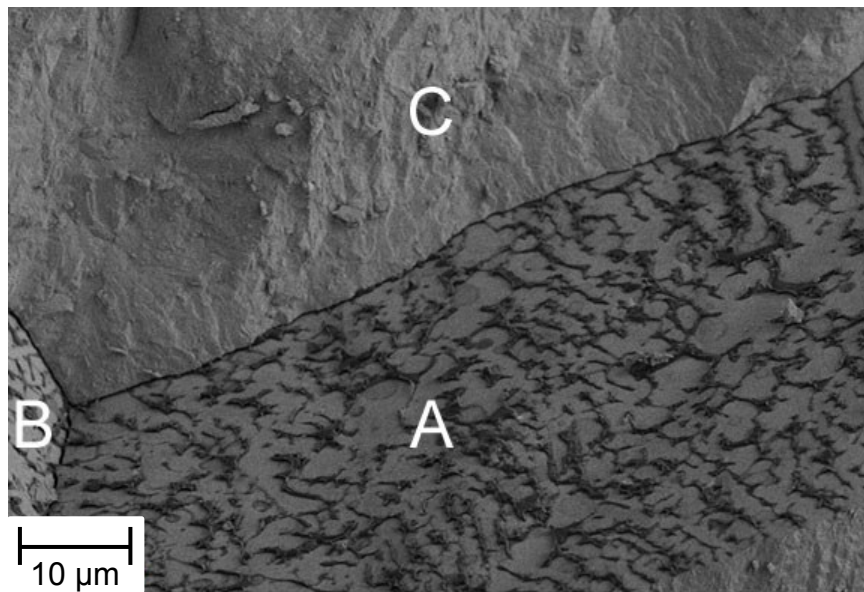
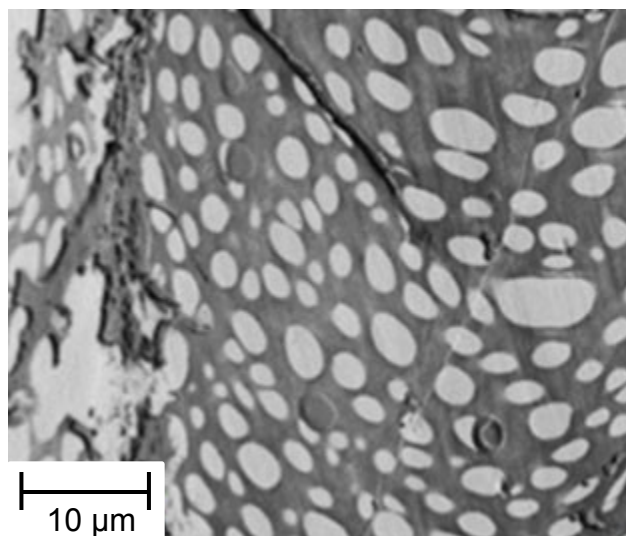


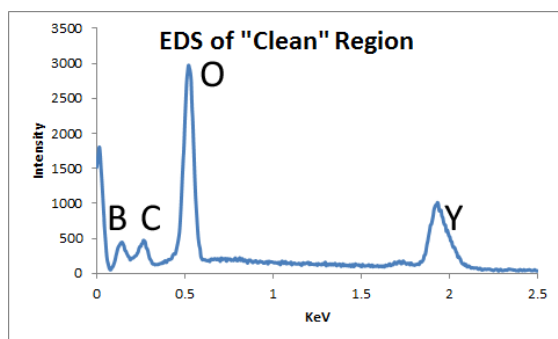
Figure 8.1 SEM micrograph of a fractured Y_2O_3 sample, after forward cubic-to-monoclinic transformation at 8.0 GPa/1000°C/15 min and partial reverse monoclinic-to-cubic transformation at 1.0 GPa/600°C/15 min, showing a lacy-carbon network at intergranular-fractured grains A and B, but not at a transgranular-fractured grain C.

Another example for the same sample, Figure 8.2, shows greater surface coverage with carbon, and a different morphology. High-resolution EDS analyses, Figures 8.2 (b) and (c), show that the dark-contrasting areas are

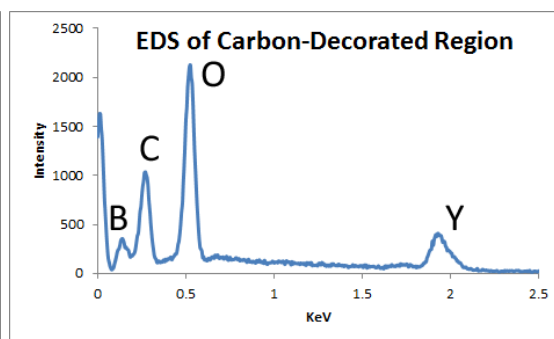
carbon rich, whereas the white-contrasting areas (globular in shape) are carbon poor.



(a)



(b)



(c)

Figure 8.2 (a) SEM micrograph of an intergranular grain boundary showing patchy decoration with carbon (dark contrast) in a coarse-grained (300 μm) sample converted to $m\text{-Y}_2\text{O}_3$ at 8.0 GPa/1000°C/15 min, and partially transformed back to $c\text{-Y}_2\text{O}_3$ at 1.0 GPa/600°C/15 min. (b) and (c) EDS spectra showing that dark-contrasting regions are carbon rich and white-contrasting regions are carbon poor.

Figure 8.3 shows additional micrographs taken at different locations of the same sample. When the crack-opening is relatively large, Figure 8.3(a), the infiltrated carbon forms a continuous film. In this particular case, the film shows

shrinkage cracks, indicating that thermal-expansion misfit stresses are responsible. On the other hand, when a crack-opening is very small, as at the tip of a propagating crack, Figure 8.3(b), the infiltrated carbon displays a dendritic-type morphology, which scales with decreasing thickness towards the crack tip. In this case, the actual crack-opening displacement is not measurable, but in another case where the carbon-decorated grain boundary is viewed end-on, the thickness is of nanometer dimensions. A few cases of grain-boundary cracking and carbon infiltration have also been observed in HPHT-processed fine-grained ($1.5\text{ }\mu\text{m}$) material, even though it is of high purity. This was most apparent in partially-transformed material that had developed a coarse columnar-grained structure.

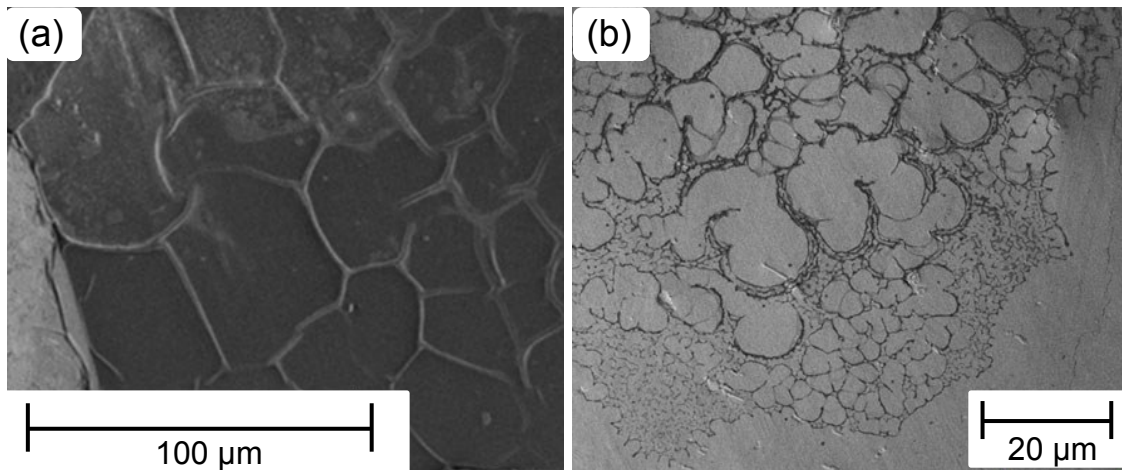


Figure 8.3 SEM micrographs showing different morphologies of infiltrated carbon: (a) complete coverage of a cracked grain boundary with a thin film of carbon; and (b) lacy network of carbon extending far into a crack tip. Sample forward-transformed to $m\text{-Y}_2\text{O}_3$ at 8.0 GPa/1000°C/15 min and partially reversed-transformed to $c\text{-Y}_2\text{O}_3$ at 1GPa/600°C/15 min.

With regard to the mechanism of carbon infiltration into cracked grain-boundaries, two possibilities are considered. Ultrafine-grained graphitic carbon displays exceptional plasticity and formability under HPHT-processing conditions, and, as noted in Section 4.1.1, it is this effect that ensures intimate contact between sample and heater during processing, even when a significant density change occurs during a phase transformation. In principle, therefore, graphitic-carbon from the heater could be forced under high pressure into a sufficiently large crack opening, facilitated by easy shear between its basal planes. However, it seems unlikely that such a mechanism can explain infiltration or penetration of a thin tapered-crack opening, such as at that at the tip of a propagating crack.

In general, gas-solid reactions are more effective than solid-solid reactions in promoting interactions between dissimilar materials. As an example, we need only cite experience in case-carburizing of steels, where the preferred method involves heating the material in a flowing gas stream of $\text{CH}_4 + \text{H}_2$ at 900°C . Carbon species formed via thermal decomposition of CH_4 react with the steel surface to form a very hard carburized layer. In the present situation, it is reasoned that contamination of the high-pressure cell with O_2 and H_2O cannot be avoided, since HPHT processing is carried out in an ambient-air environment. During processing, therefore, these contaminants react with the graphitic-carbon heater to form carbon-containing gases (e.g. CH_x , CO , CO_2), which under pressure can infiltrate (penetrate) any crack openings in the sample, depositing carbon via a vapor-deposition mechanism.

To test the proposed carbon-infiltration mechanism, two optically-flat samples were stacked one on top of the other and processed at 8.0 GP/1000°C/15 min. The small gap between the contacting surfaces became infiltrated with carbon, not unlike samples that cracked during HPHT processing.

We conclude, therefore, that cracked grain boundaries in fine- and coarse-grained Y_2O_3 are infiltrated with carbon-containing species during HPHT processing, resulting in carbon deposition, even in the smallest crack opening, such as at the tip of a propagating crack. Specifically, the proposed mechanism involves transport of gaseous carbon-containing species from source (carbon heater) to sink (sample), driven by the high carbon-activity gradient in the enclosed pressurized system.

Variations in surface coverage and morphology of infiltrated carbon may be ascribed to the influence of grain-boundary misfit, e.g. coherent coincident-site boundaries versus incoherent high-angle boundaries. Thus, surface interactions can vary from one grain boundary to the next, resulting in various carbon deposition morphologies.

Similar carbon-infiltration effects have been observed in fine-grained material, but primarily in regions where internal stresses are complex, such as at sample edges and corners, where grain boundary cracking often occurs. An example of carbon deposition at coarsened equiaxed grains of c- Y_2O_3 , near the edge of a cracked sample, is shown in Figure 8.4.

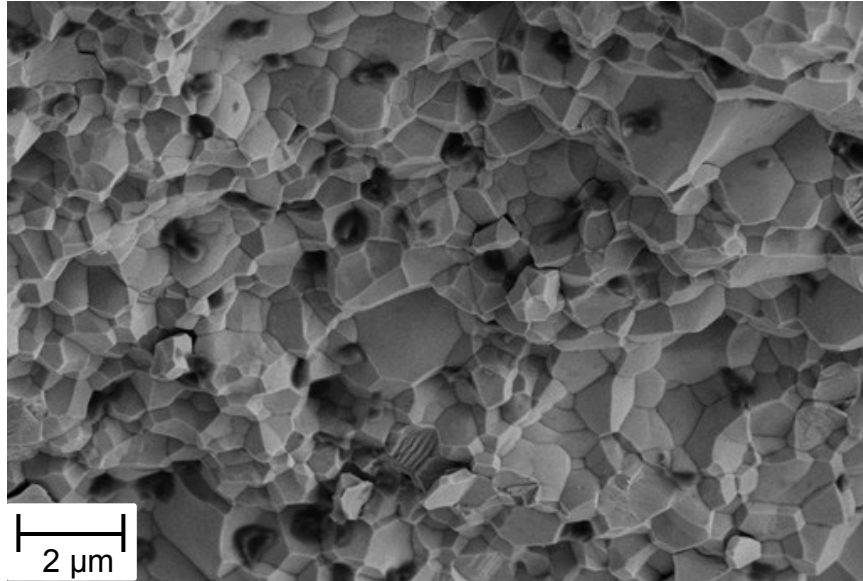


Figure 8.4 Carbon-particle decoration of equiaxed grains of $c\text{-Y}_2\text{O}_3$, after processing at 8.0 GPa/1000°C/15 min and then at 1.0 GPa/1000°C/15 min. The dark-contrasting phase is carbon.

In the mid-section of the same sample, such grain-boundary cracking and infiltration is largely suppressed, but carbon ingress via a grain-boundary diffusion mechanism occurs, as discussed below. An exception is partially-transformed material, where there is a sharp discontinuity between inward-growing columnar grains and underlying equiaxed grains, Figure 8.5. In this particular case, carbon particles decorating the columnar grains of $m\text{-Y}_2\text{O}_3$ have a globular morphology, indicating poor-wetting between particles and matrix.



Figure 8.5 Carbon-particle decoration of columnar-grained $m\text{-Y}_2\text{O}_3$ formed at 3.0 GPa/1000°C/15 min. Growth of coarse columnar grains is from right (surface) to left (interior); the underlying forward-transformed $m\text{-Y}_2\text{O}_3$ is essentially unchanged.

In Figure 8.5, decoration of the columnar grains with carbon particles varies from one boundary to the next. In some cases, particle decoration is fairly uniform in the direction of columnar-grain growth from surface (right) to interior (left), whereas in other cases there is a progressive decrease in particle size with increasing distance from the sample surface, as expected for a propagating crack. In a few cases, there is no visible evidence for carbon-particle decoration, indicating that these particular grain boundaries did not experience fracture, so could not be infiltrated by gas-phase carbon species.

Taken together, these observations are consistent with a carbon-infiltration mechanism that involves vapor transport of carbon species into pre-existing cracks, including propagating cracks, followed by precipitation of nanoparticles when the carbon concentration attains some critical level.

A bundle of columnar grains, such as that shown in Figure 8.5, probably has a preferred orientation (not yet determined), so that carbon precipitation should not vary too much from one grain to the next. In fact, all the carbon nanoparticles, small and large, display roughly the same globular-like morphology, probably reflecting a minimum in the interphase-interface energy between carbon particles and Y_2O_3 matrix.

Finally, we note that anomalous microstructural changes occur at *sample edges and corners*, particularly when a reversible-phase transformation is involved. Taking a typical case, where a forward-transformation at 8.0 GPa/1000°C is followed by a reverse transformation at 1.0 GPa/1000°C, amongst the most commonly observed effects are: (1) increased propensity for grain-boundary cracking, (2) carbon infiltration into the crack openings, (3) exaggerated grain growth, possibly facilitated by impurity carbon, and (4) distorted growth of surface-nucleated columnar grains, as they propagate into the interior. Striking examples of grain coarsening at sample corners are shown in Figure 8.6.

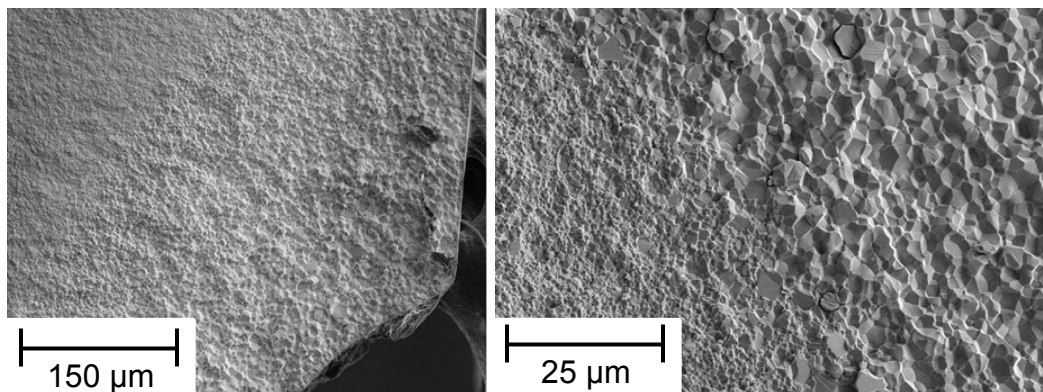


Figure 8.6 Examples of coarsening at the corners of a sample reversibly transformed at 8.0 GPa/1000°C/15 min followed by 1 GPa/1000°C/15 min.

In summary, only mid-sections of a disc-shaped sample display microstructural changes that are reproducible from one sample to the next. Hence, it is in these regions that most of the observations have been made and analyzed.

8.2 Carbon Diffusion

Carbon segregation at grain boundaries has also been detected in crack-free samples of fine-grained material, after various HPHT processing treatments. The carbon concentration is low, but often sufficient to induce intergranular fracture in bending. The evidence points to grain-boundary diffusion of carbon from an external source, here identified as carbon-rich gases formed and entrapped in the pressure cell, as discussed above.

Detection of carbon in HPHT-processed samples by EDS analysis is problematic, since the carbon concentration is low. However, when carbon segregation attains a critical concentration, the fracture mode is invariably intergranular, so that its presence can be inferred. As noted above, it is only in impurity-free material that transgranular fracture is observed.

Figure 8.7 shows EDS spectra for *different regions of the same sample*, after a reversible-phase transformation at 1000°C. *Intergranular fracture near the edge* of the sample, Figure 8.7 (a), indicates the presence of a small amount of carbon (also boron from an unknown source), whereas *transgranular fracture in the mid-section* of the same sample, Figure 8.7 (b), shows no detectable carbon (or boron) present. Since both spectra are taken at a depth of ~500 µm below the sample surface, this is taken to be evidence for inward diffusion of carbon from an external source deep into the interior of the sample. Given a longer holding time under the same processing conditions, such carbon segregation becomes uniform throughout the entire sample. As discussed above, the probable mechanism is gas-phase transport of carbon species from heater to sample,

followed by pressure-assisted diffusion of carbon-containing species into the grain boundaries.

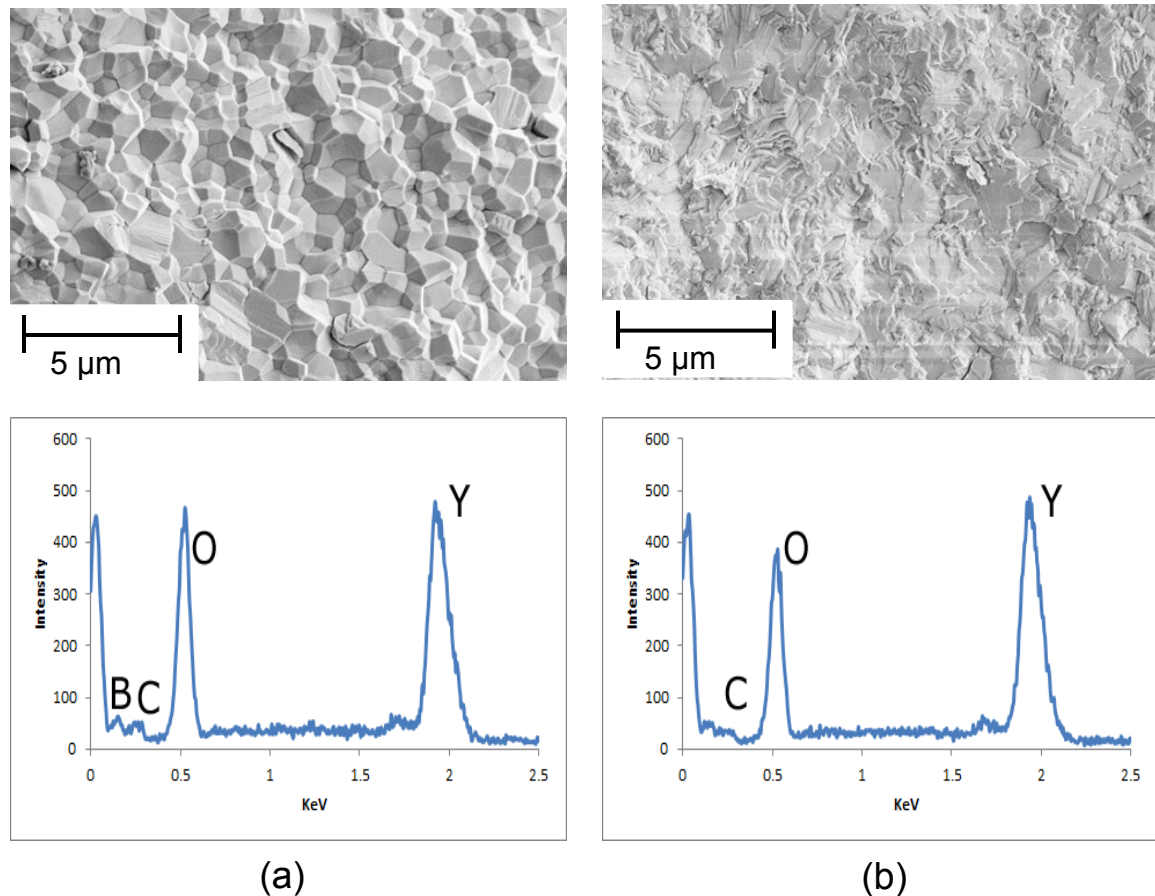


Figure 8.7 SEM and EDS analysis of a sample after a reversible phase transformation (8.0 GPa/1000°C/15 min and 1.0 GPa/1000°C/15 min), comparing carbon segregation in regions of: (a) intergranular fracture near the edge of the sample, and (b) transgranular fracture near the midsection of the sample; both at a depth of ~500 μm below the sample surface.

No evidence has been obtained for carbon diffusion into the *grains themselves*, whatever the processing conditions adopted. However, a surface-reaction layer, Figure 8.8 (a), identified by XRD as an oxy-carbonate phase with composition $Y_2O_2CO_3$, has been observed, but not reproducibly from one sample to the next. It is believed that this variability can be attributed to differences in the

gas-phase composition in the pressure cell during processing, which can change depending on the extent of degassing of carbon heater, and its deformable ceramic container. As shown in Figure 8.8 (b), the oxy-carbonate phase is readily removed by light polishing, revealing the underlying predominant c- Y_2O_3 phase at a depth of about 10 μm .

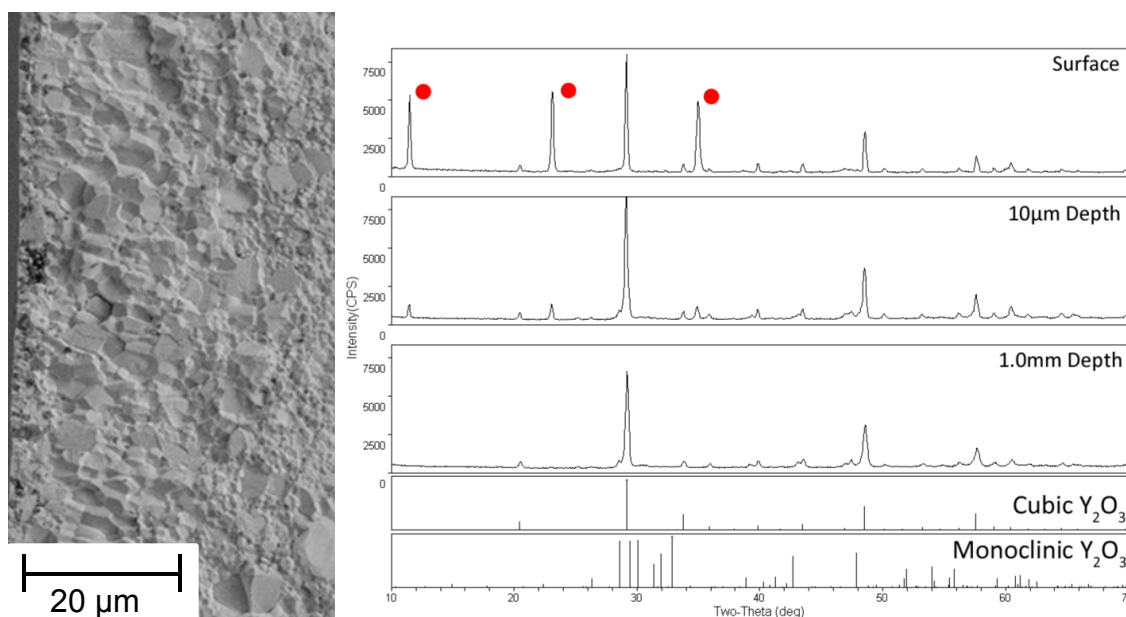


Figure 8.8 (a) SEM image of columnar surface phase for reversibly-transformed sample; (b) XRD spectra identifying the thin surface layer as $\text{Y}_2\text{O}_2\text{CO}_3$ phase. The highlighted peaks are $hkl = 002, 004$ and 006 for $\text{Y}_2\text{O}_2\text{CO}_3$, indicating a high degree of cube texturing.

We have also observed intergranular-fractured surfaces that are decorated with very fine particles of an unknown phase. An example is shown in a high magnification SEM image, Figure 8.9, where fine details are revealed on the fracture surface. There are many sites (top right of micrograph) where some type of surface reaction has taken place. More work is needed to clarify what appears to be an early stage in reaction of carbon with a grain boundary in Y_2O_3 .

There are many grain boundaries where intergranular fracture is also apparent, probably possibly reflecting weakening of the boundaries by the presence of this unidentified phase.

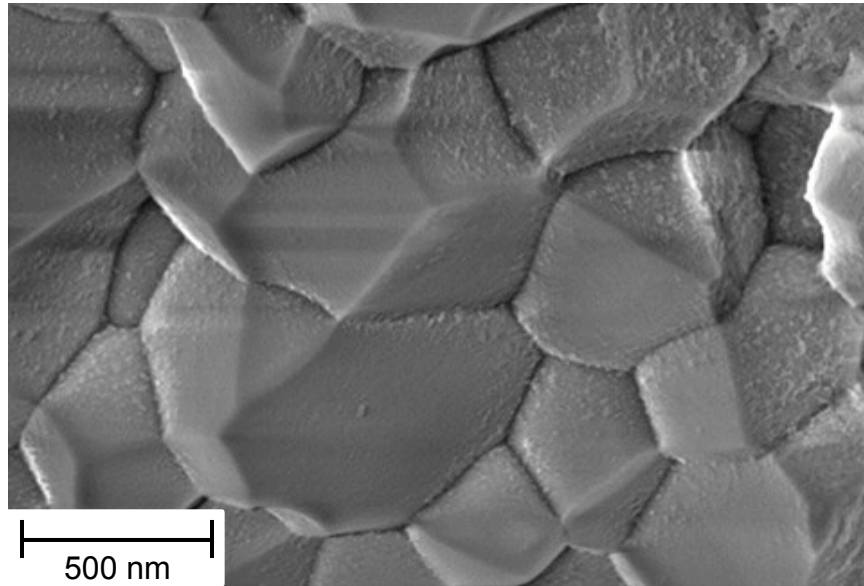


Figure 8.9 SEM image of equiaxed grains of $c\text{-Y}_2\text{O}_3$, showing the presence of an unknown phase at fractured grain boundaries.

8.3 Grain Coarsening

Samples processed at 1.0-2.5 GPa at 1000°C experience significant grain coarsening, as indicated in Table 8-1. This is unexpected since 1000°C is less than $0.5 T_m$, where T_m is the absolute melting point of c-Y₂O₃. Normally upon annealing at ambient pressure, grain growth occurs at temperatures $>0.7 T_m$.

Table 8-1 Density and grain size measurements for samples processed at given pressures at 1000°C and 240mins.

Pressure (GPa)	Density (g/cm ³)	Phase	Grain Size (μm)
Ambient	5.02	Cubic	1.5*
1.0	4.89	Cubic	1.5-30
2.5	4.915	Cubic	40-60

*As-received material.

A typical example for a fine-grained sample, processed at 1.0 GPa/1000°C/240 min, is shown in Figure 8.10. The grain-coarsening effect occurs uniformly throughout the sample, with grain size measuring 20-30 μm on average. This represents a 20-fold increase in grain size relative to the grain size (~1.5 μm) of the starting material. Since no phase change occurs during processing, the grain-coarsening effect accompanied by intergranular fracture may be attributed to carbon segregation at grain boundaries of the untransformed c-Y₂O₃, again from the carbon heater, as discussed above. But why this should affect grain-boundary mobility is puzzling. Possibly, the effective melting point of the carbon-infused grain boundaries is significantly lower than that of the matrix, thus enabling grain-boundary migration to occur at a much lower temperature than for clean boundaries in phase-pure c-Y₂O₃. Another

possibility is that modulus-mismatch stresses developed neighboring grains under a near-isostatic pressure provide a driving force for grain coarsening. This model is consistent with the observation that abnormally-stressed corners of a sample are particularly susceptible to grain coarsening. Further research under well-controlled processing conditions is needed to resolve this problem. In particular, theoretical work is needed to determine the influence of modulus-mismatch stresses between neighboring grains in providing a driving force for exaggerated grain growth at a relatively low temperature.

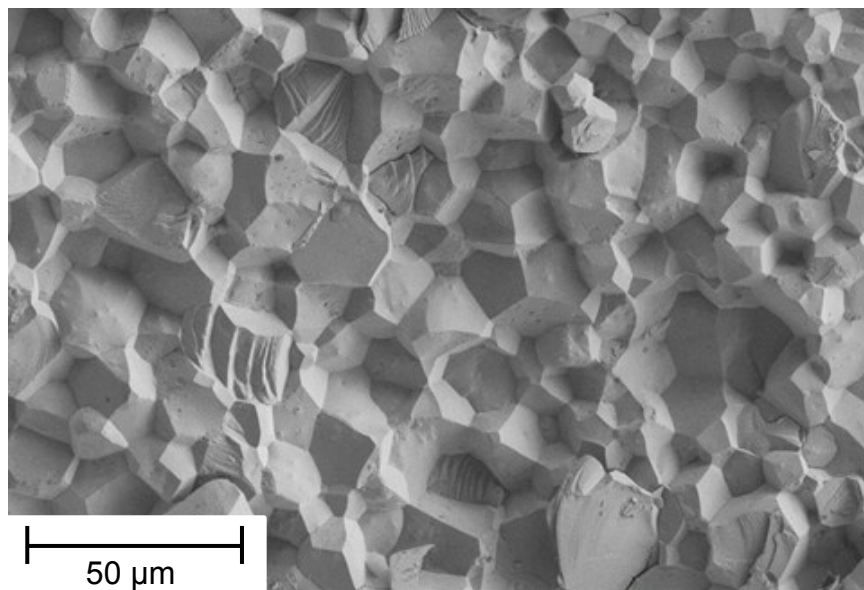


Figure 8.10 SEM image of a fine-grained c-Y₂O₃ sample, after processing at 1.0 GPa/1000°C/240 min, showing significant coarsening of the initial equiaxed grain structure.

A similar behavior is observed in c-Y₂O₃ processed at 2.5 GPa, again with no phase change, except for a thin surface layer of monoclinic phase, Figure 7.12. In the interior of the sample, grain coarsening is observed, Figure 8.11 (a), accompanied by brittle grain-boundary fracture. XPS analysis, Figure 8.11 (b),

conducted along a sputtered-depth profile, shows a decrease in carbon-peak intensity with increase in sputtering depth. This result confirms the presence of carbon enrichment at grain boundaries in $c\text{-Y}_2\text{O}_3$ to a depth of a few nanometers. Apparently, this is more than sufficient to embrittle the grain boundaries, and hence account for the observed intergranular fracture.

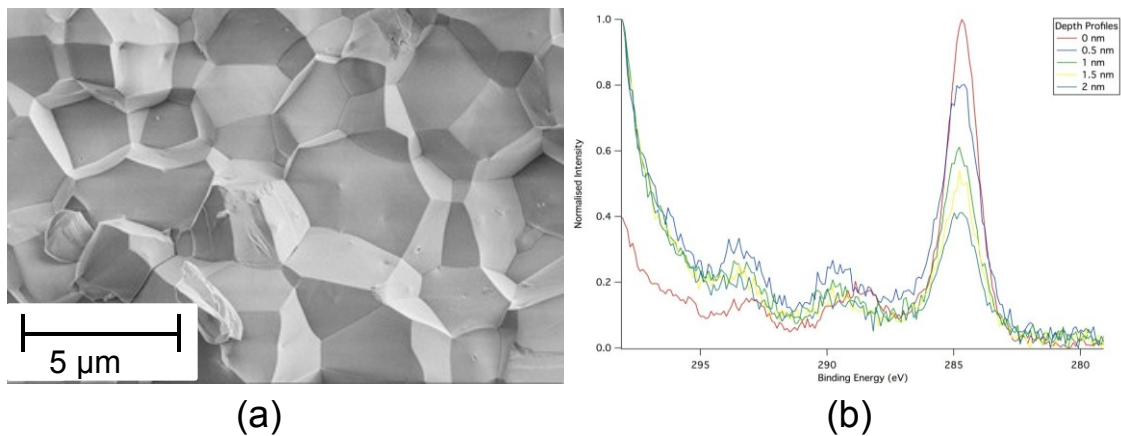


Figure 8.11(a) SEM image, and (b) XPS spectra for an untransformed $c\text{-Y}_2\text{O}_3$ sample that exhibits significant grain coarsening, after processing at 2.5 GPa/1000°C/240 min.⁸⁰

Such grain coarsening has also been observed in reversibly-transformed samples, but usually only at sample corners where internal stresses are complex. In a typical case, Figure 8.12, the grain size progressively decreases with increasing depth in the sample, reflecting the depth of penetration of diffusing carbon-species into the sample.

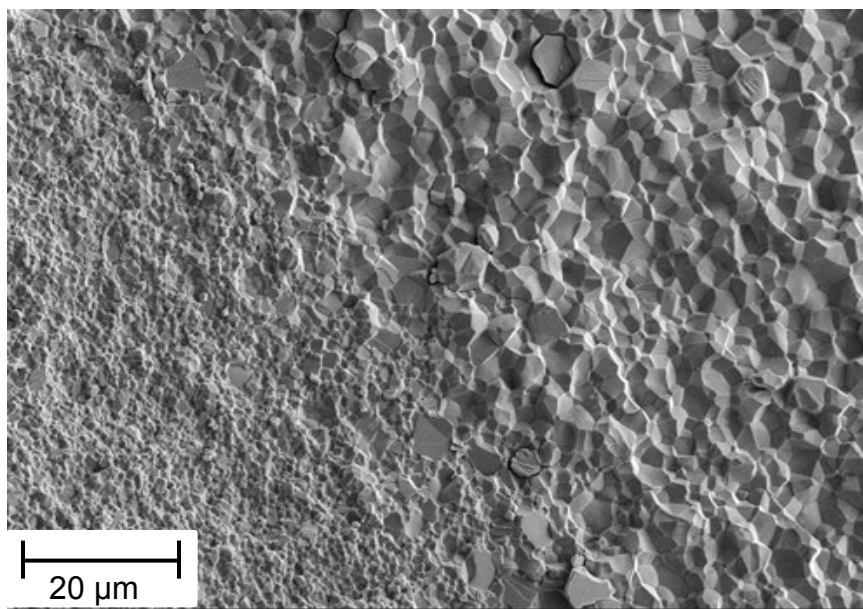


Figure 8.12 SEM image of the corner of a reversibly-transformed $c\text{-Y}_2\text{O}_3$ sample, showing a decrease in grain size from surface (right) to interior (left). The grain size from coarse-to-fine extends over a distance of $\sim 200\mu\text{m}$.

8.4 Conclusions

- Commercial-grade coarse-grained (300 μm) c- Y_2O_3 is susceptible to *intergranular fracture* due to weakening of its grain boundaries by impurity segregation, whereas optical-grade (high purity) fine-grained (1.5 μm) c- Y_2O_3 is essentially free of impurity segregation, and therefore experiences *transgranular fracture*.
- Reactions between the graphitic-carbon heater and entrapped gases (e.g. O_2 , H_2O) in the pressure cell generate carbon-containing gases (e.g. CH_x , CO , CO_2), which interact with HPHT-processed samples in various ways.
- Infiltration of carbon-containing gases into *cracked grain boundaries* results in boundary decoration with carbon via a *vapor-deposition mechanism*. This is so effective that even the very narrowest of crack openings (crack displacements) at a crack tip become decorated with impurity carbon.
- Infiltration of carbon-containing gases into *un-cracked grain boundaries* results in boundary decoration with carbon-rich species via a *boundary-diffusion mechanism*. This has an adverse effect on grain-boundary strength, so that even high purity fine-grained material (initially displaying transgranular fracture) becomes highly susceptible to intergranular fracture.

9 MEASUREMENT OF HARDNESS

HPHT processing of c-Y₂O₃ results in structural changes that are strongly influenced by pressure, temperature, and holding time, as discussed in Chapters 7 and 8. In particular, striking changes in grain size and morphology are observed under various processing conditions. Here, we describe changes in hardness due to variations in HPHT-processing parameters. In all cases, a minimum of 5 Vickers hardness indentations are made on each sample, from which the standard deviation is estimated.

As described in Section 2.5 and shown in Figure 2.7 for the cubic-to-monoclinic Y₂O₃ transformation, pressure and temperature are co-dependent such that an increase in either processing condition should increase the cubic-to-monoclinic transformation driving force. Above critical transformation conditions, higher HPHT conditions should therefore accelerate cubic-to-monoclinic conversion and result in finer-grained m-Y₂O₃ products with greater hardness as per the Hall-Petch relationship.

9.1 Effect of Phase Transformation

Initial hardness measurements were made on samples of coarse-grained (300 μm) c- Y_2O_3 that had been subjected to a forward cubic-to-monoclinic transformation at 8.0 GPa/1000°C/15 min, followed by a reverse monoclinic-to-cubic transformation at 1.0 GPa/1000°C/15 min¹⁰.

As shown in Figure 9.1, an increase in hardness of about 35% accompanies the forward transformation from micro-grained c- Y_2O_3 to nano-grained m- Y_2O_3 . On the other hand, after reverse transformation back to nano-grained c- Y_2O_3 , the hardness is reduced by about 15%, representing an overall increase due to grain size refinement of about 20%. The corresponding changes in density ($\pm 6\%$) reflect the phase changes (cubic-monoclinic-cubic) accompanying a reversible-phase transformation.

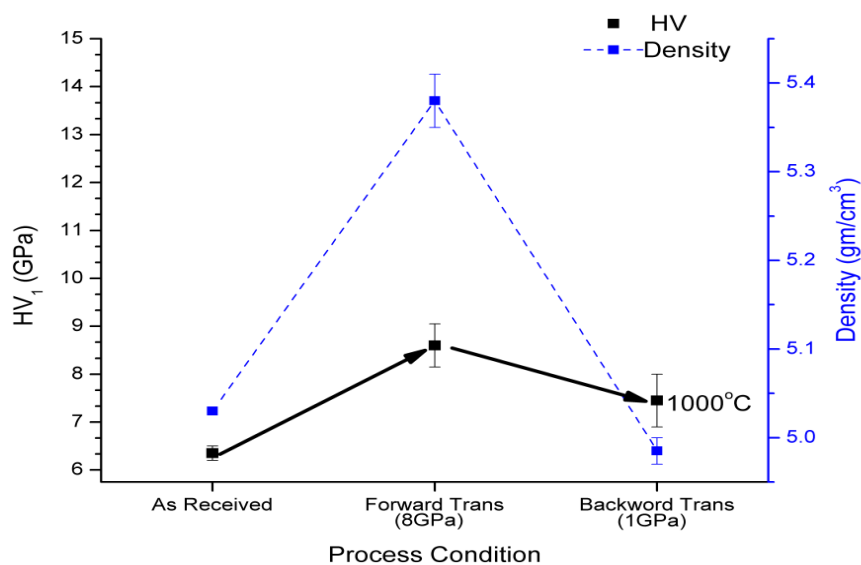


Figure 9.1 Density and hardness changes in Y_2O_3 due to a reversible-phase transformation.¹⁰

Reversibly-transformed fine-grained ($1.5\ \mu\text{m}$) material displays similar hardness values as coarse-grained ($300\ \mu\text{m}$) material, both in the forward-transformed nanocrystalline m- Y_2O_3 state and in the reverse-transformed nanocrystalline c- Y_2O_3 state. Relatively small variations in hardness are attributed to differences in initial grain size and purity of the materials.

Several samples of fine-grained material were first forward-transformed at $8.0\ \text{GPa}/1000^\circ\text{C}/15\ \text{min}$ and then reverse-transformed at $1.0\ \text{GPa}$, but with varying temperatures and holding times. As shown in Figure 9.2, the hardness varies with processing conditions. The largest increase in hardness occurs for partially reverse-transformed material, where varying volume fractions of c- Y_2O_3 and m- Y_2O_3 nanophases co-exist, described in Section 7.4.1 as a self-nanocomposite. In particular, we note that the highest hardness occurs after reverse-transformation at 700°C for $240\ \text{min}$, which according to Table 7-3, corresponds to about 40% conversion to the c- Y_2O_3 state.

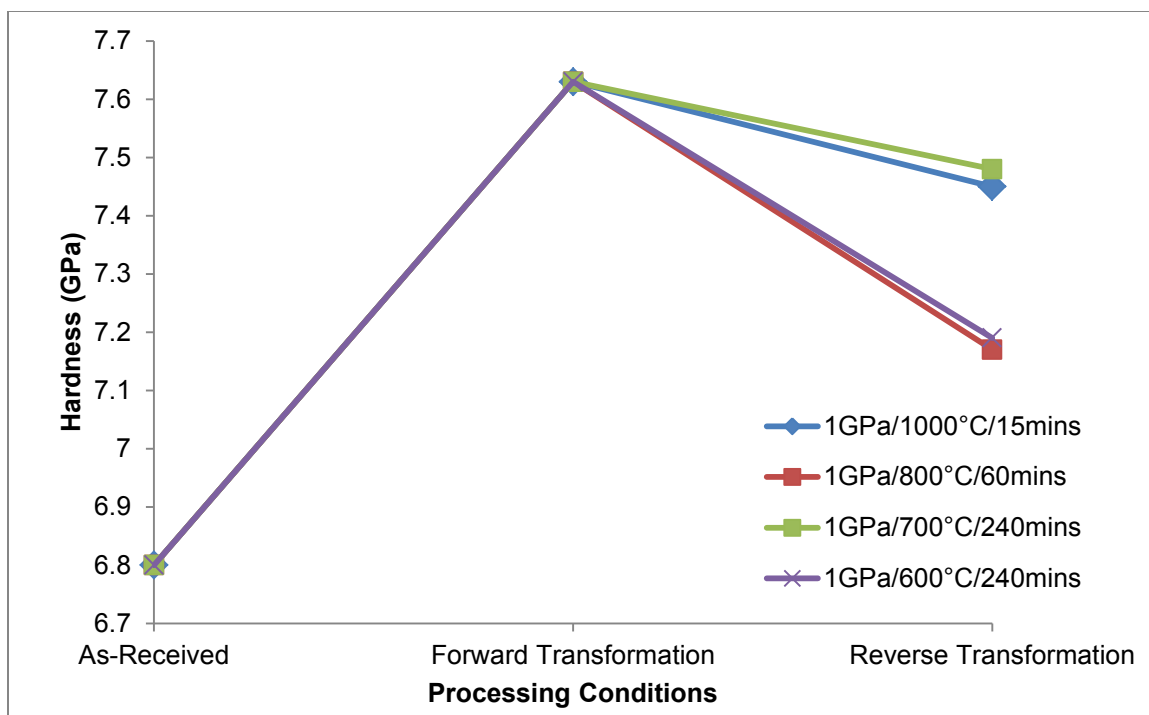


Figure 9.2 Plot of hardness versus reverse transformation processing conditions.

Figure 9.3 correlates processing conditions with changes in density of reversibly-transformed samples. Although samples annealed at 800°C and 700°C both feature a similar percentage of transformed c-Y₂O₃ product, the distribution is different, explaining the difference in hardness. A sample processed at 800°C for a short duration demonstrates a thicker transformed cubic shell structure, while a sample transformed at 700°C for longer duration demonstrates a more uniform distribution of fine-grained transformed cubic material throughout the bulk. There is also evidence that continued annealing of monoclinic Y₂O₃, without successfully inducing the monoclinic-to-cubic transformation, results in loss of hardness.

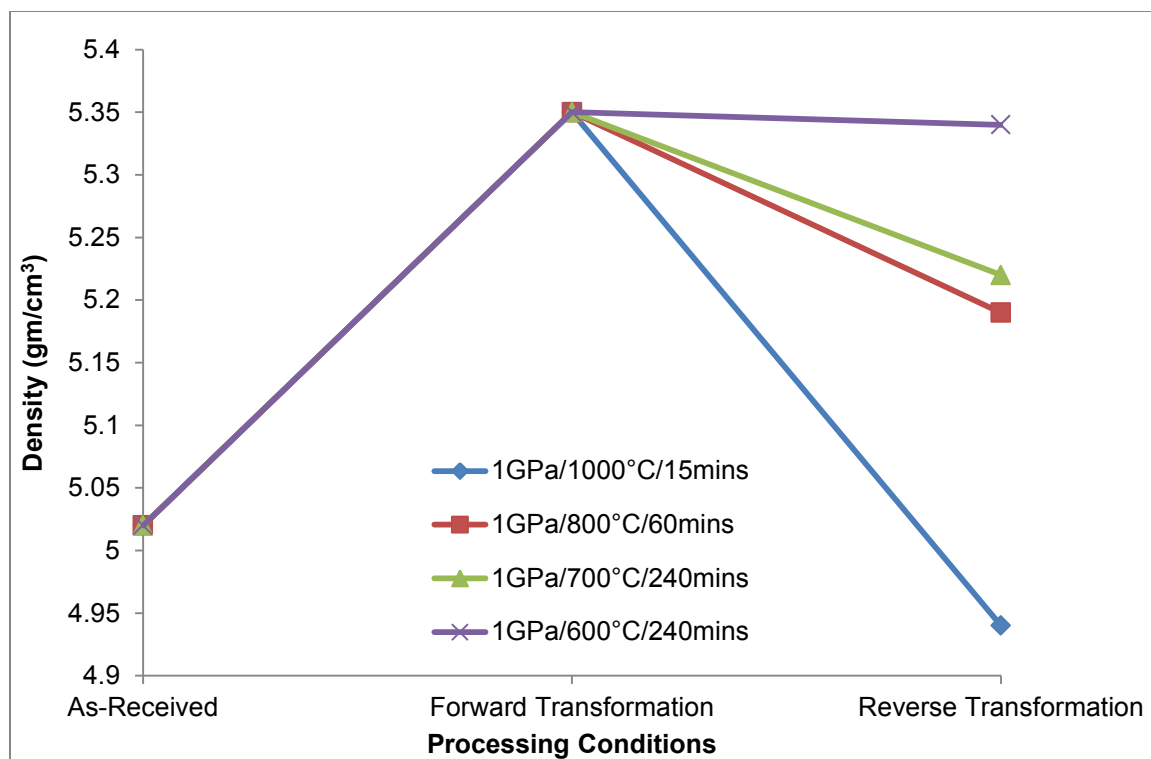


Figure 9.3 Plot of density versus reverse transformation processing conditions.

9.2 Effect of Pressure

Figure 9.4 shows a plot of hardness versus pressure for samples processed at 1000°C for 240 minutes. The discontinuity between 2.5 and 3.0 GPa correlates with the onset of the cubic-to-monoclinic Y_2O_3 transformation. In the untransformed c- Y_2O_3 state at pressures <2.5 GPa, the hardness increases slightly with increasing pressure. Even so, the equiaxed-grain size increases about 30 times, Table 7-1. On the other hand, in the transformed m- Y_2O_3 state at pressures >3.0 GPa, hardness increases significantly with increasing pressure, reaching a plateau at 6.5-8.0 GPa.

The relatively small increase in hardness at pressures <2.5 GPa is not easily explained. One possibility is that the number of cation-anion bonds per unit volume in c- Y_2O_3 is increased via the elimination of *anion vacancies* under high pressure. This could occur by vacancy absorption at grain boundaries and/or by the formation of edge-dislocation loops within the grains themselves. High-resolution TEM is needed to check this model.

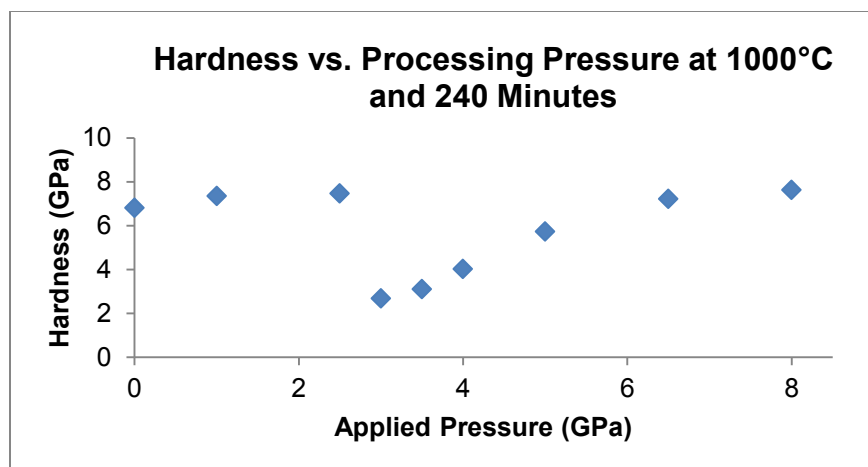


Figure 9.4 Plot of hardness versus processing pressure, showing a sharp discontinuity at 2.5-3.0 GPa, corresponding to the critical phase-transformation pressure.

Table 9-1 Density, grain size, and hardness measurements for samples processed at the given pressures at 1000°C and 240 mins.

Pressure (GPa)	Density (g/cm ³)	Phase	Grain Size (μm)	Hardness (GPa)
Ambient	5.02	Cubic	1.5	6.8
1.0	4.89	Cubic	1.5-30	7.35
2.5	4.915	Cubic	40-60	7.47
3.0	5.27	Monoclinic	20-1500+	2.68*
4.0	5.35	Monoclinic	10 - 100	3.1*
5.0	5.33	Monoclinic	0.05-4	5.73
6.5	5.41	Monoclinic	0.05-0.5	7.21
8.0	5.33	Monoclinic	0.05	7.63

*These samples are easily crushed by the Vickers diamond tip during hardness testing.

The increase in hardness at pressures >3.0 GPa is more understandable, since major changes in grain size and morphology occur in the 3.0-8.0 GPa range. We have described the occurrence of an exceptionally coarse (1500 μm) columnar-grained m-Y₂O₃ at 3.0 GPa, and an exceptionally fine (<50 nm)

equiaxed grained m-Y₂O₃ at 8.0 GPa. At intermediate pressures in the 4.0-6.5 GPa range, there is a gradual transition from micro-to-nano grained structures, accompanied by a change in grain morphology from columnar-to-equiaxed forms. Hence, the grain size changes progressively with increasing pressure in the 3.0-8.0 GPa range, with the most drastic changes at 3.0-4.0 GPa. When plotted as hardness versus inverse square root of grain size (Hall-Petch relationship), a linear relationship is found, Figure 2.11. Thus, the hardness increase in the 3.0-8.0 GPa range is attributed to a major reduction in grain size of the forward-transformed m-Y₂O₃.

9.3 Effect of Temperature

In an early series of experiments, three 300 μm -grain samples underwent HPHT processing at 1000°C, 1100°C, and 1200°C, with the applied pressure and holding times fixed at 8.0 GPa and 240 mins. Hardness measurements of the m-Y₂O₃ products, Figure 9.5, show a trend where hardness increases linearly with temperature.

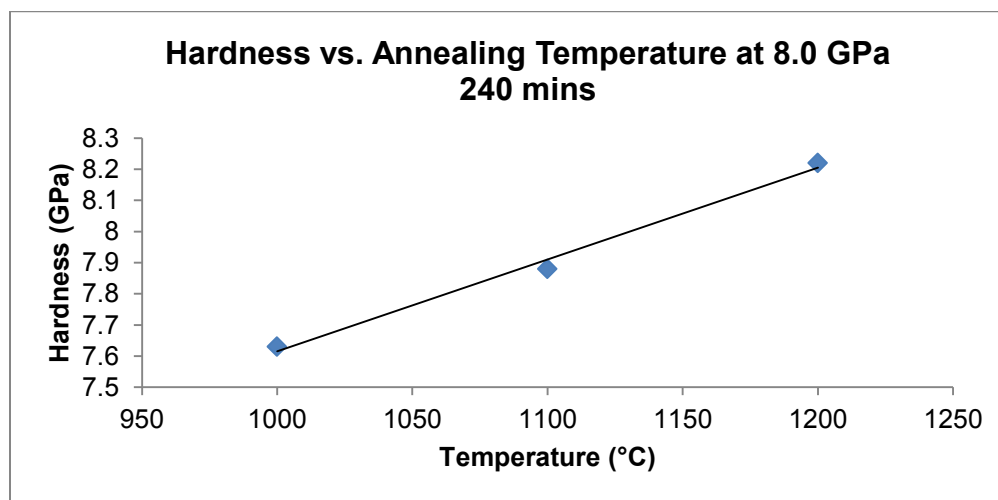


Figure 9.5 Plot of hardness vs. annealing temperature at 8.0 GPa and 240 minutes.

9.4 Conclusions

- Reversibly-transformed fine- and coarse-grained c-Y₂O₃ samples at 1000°C display an increase of about 35% in the forward-transformed state, and about 20% in the reverse-transformed state.
- Partially reverse-transformed samples, where the reverse transformation is conducted at 600-800°C, show hardness variations due to different degrees of transformation from the nanocrystalline m-Y₂O₃ state to the nanocrystalline c-Y₂O₃ state.
- The largest increase in hardness occurs in partially reverse-transformed samples, where varying volume fractions of c-Y₂O₃ and m-Y₂O₃ co-exist, described herein as a self-nanocomposite.
- A significant increase in hardness due to a forward phase-transformation from cubic-to-monoclinic Y₂O₃ at pressures >3.0 GPa is due to a reduction in grain size from micron- to nano-scale dimensions.
- A modest increase in hardness due to grain coarsening upon annealing at pressures <2.5 GPa, accompanied by a major increase in grain size, is tentatively attributed to an increase in the number of strong cation-anion bonds per unit volume in c-Y₂O₃ due to the elimination of anion vacancies under high pressure.
- An increase in HPHT processing temperature beyond 1000°C results in a linear increase in hardness, suggesting that further increases in temperature may yield even finer-grained and harder m-Y₂O₃ materials.

- Increasing HPHT processing conditions, such that the holding time required for full transformation is minimized, should result in the finest-grained and hardest m-Y₂O₃ product possible.

10 SUMMARY AND DISCUSSION

Numerous studies have been performed on high-pressure/high temperature phase transitions in rare-earth sesquioxides, as summarized in Chapter 2. Most of these studies were performed using a diamond-anvil press, which limits the size of samples that can be processed. Hence, studies of microstructural and properties changes accompanying the phase transitions have been neglected.

The purpose of this study has been to fill this gap, working with polycrystalline cubic- Y_2O_3 because of its importance for IR window and dome applications. We also selected Diamond Materials Inc. as partner in this investigation, since this company has the expertise to make test pieces under well-controlled HPHT-processing conditions, thus ensuring that the results obtained for one batch of samples to the next are reproducible. This turned out to be crucial, since relatively small variations in applied pressure (1.0 to 8.0 GPa range), and holding times (seconds to hours) resulted in significant structural changes, as documented in Chapters 7 and 8. The temperature was fixed at 1000°C in order to limit HPHT-processing variables to pressure and holding time. *However, in view of the results reported here, it now seems clear that extending the investigation to higher temperatures and lower pressures has merit.*

10.1 Reversible Phase Transformation

Subjecting polycrystalline cubic- Y_2O_3 , irrespective of its initial grain size, to a reversible-phase transformation under well-controlled HPHT-processing conditions has been shown to be the key to transforming the material into the nanocrystalline state. Specifically, a forward-phase transformation (cubic-to-monoclinic) at 8.0 GPa/1000°C/15 min generates nanocrystalline m- Y_2O_3 , and a reverse-phase transformation (monoclinic-to-cubic) at 1.0 GPa/1000°C/15 min regenerates c- Y_2O_3 , but now with a nanocrystalline (<50 nm grain size) structure.

When the grain size of c- Y_2O_3 is <1/30 of the wavelength of light of interest (as in the present case), little or no scattering occurs at the grain boundaries, thus ensuring high optical transmission. Along with that, reducing the grain size to nanoscale dimensions enhances fracture strength and increases hardness. Taken together, these property benefits make nanocrystalline c- Y_2O_3 a candidate material for future IR-transmission applications. But the pressure required to induce a forward transformation to the nano-monoclinic state must be lowered, otherwise scaling the technology is impractical.

Increasing temperature reduces the critical pressure to induce a cubic-monoclinic transformation for the entire family of rear-earth sesquioxide phases, Figure 2.7. In the case of Y_2O_3 , the pressure needed to induce such a phase transformation is reduced from 2.5 GPa at 1000°C to ~1.7 GPa at 1400°C. It seems reasonable, therefore, that a decrease in pressure coupled with an increase in temperature would also yield nanocrystalline m- Y_2O_3 via a forward-

phase transformation, which is a prerequisite for generating nanocrystalline c-Y₂O₃ via a reverse-phase transformation. Possibly, the forward-transformation step to create the desired homogeneous nanocrystalline m-Y₂O₃ state can be lowered from 8.0 GPa to 3.0-4.0 GPa at 1400°C, with holding times in seconds. *Additional work at higher temperatures and lower pressures, therefore, seems warranted, since it could lead to a scaled-HPHT process for making nanocrystalline c-Y₂O₃ components or parts, e.g. large area IR windows or domes.* HPHT processing of large pieces at pressures of 5.0-6.0 GPa is well within the capabilities of industrial-scale presses used in the production of diamond and cubic-BN.

10.2 Forward Phase Transformation

The most striking observations were made on samples that had been HPHT-processed at a pressure just above the critical cubic-to-monoclinic transformation pressure, which at 1000°C was determined to be 2.5-3.0 GPa, depending on holding time. At a pressure of 3.0 GPa, i.e. just above the critical pressure, a major change in grain size and morphology of the monoclinic phase is observed. Monoclinic columnar grains are nucleated at the sample surface and propagate into the sample interior with increasing holding time. After a long enough holding time, the columnar-grained structure encompasses the entire sample volume, having grown inwards from opposite sides and meeting in the middle.

With increasing pressure, there is gradual transition from heterogeneous (surface) nucleation of very coarse (micro-grained) columnar grains at 3.0 GPa to homogeneous (bulk) nucleation of very fine (nano-grained) equiaxed grains at 8.0 GPa. Thus, at 3.0 GPa nucleation rate is low and growth rate high, whereas at 8.0 GPa nucleation rate is high and growth rate low. At intermediate pressures, there is a gradual transition from surface to bulk nucleation of the m-Y₂O₃ phase.

As noted in Section 7.3, observations made at top and bottom surfaces (mid-sections only) of disc-shaped samples yielded the most consistent results, due to greater uniformity in applied pressure. At edges and corners of the same samples, the observed columnar-grained structures are exceedingly complex,

reflecting inward growth of columnar grains from different directions, often displaying pronounced curvature. Such anomalous effects are attributed to changes in internal-stress distribution driving the phase transformation at these locations during processing.

In the mid-section of a sample processed at 3.0 GPa/1000°C, uniform propagation of a bundle of textured-columnar grains is observed. It is believed that the pressure-induced phase change that occurs at the tips of the growing m-Y₂O₃ columnar grains, accompanied by 6% increase in density, is primarily responsible for driving the interphase-interface forward. Another contributing factor, probably small, is the reduction in total grain boundary energy per unit volume, as the coarse columnar-grained m-Y₂O₃ grows at the expense of the underlying fine equiaxed-grained c-Y₂O₃.

In the pressure-range 1.0-2.5 GPa, where there is no transformation to the monoclinic state, the initial fine-grained (1.5 μm) c-Y₂O₃ also experiences grain coarsening, but with no detectable change in morphology. This surprising result has yet to find an explanation. However, it is proposed that modulus misfit between neighboring grains under high pressure (here quasi-isostatic) provides a driving force for grain boundary migration, and hence grain coarsening. Additional experiments, supported by computational modeling, are needed to validate the model.

10.3 Reverse Phase Transformation

The most significant observations were made on samples that had been subjected to a forward-phase transformation at 8.0 GPa/1000°C/15 min to develop nanocrystalline m-Y₂O₃, followed by a reverse-phase transformation at 1.0 GPa/600-1000°C/15-240 min to develop nanocrystalline c-Y₂O₃, i.e. *at the same pressure for varying temperature and holding time*.

After re-processing at 1.0 GPa/1000°C/15 min, the reverse monoclinic-to-cubic transformation is essentially complete. In contrast, at lower transformation temperatures, much longer holding times are needed to complete the reverse transformation. Even at 700°C, however, it appears that complete transformation is achievable if given a sufficiently long holding time.

While uniform bulk transformation occurs at 1000°C, there is an additional surface-originating inward growth transformational mode at lower temperatures (Section 7.4.1). For short holding times the result is a *core-shell structure*, where the sample interior (core) is *partially transformed monoclinic* phase, and the sample surface (shell) is *completely transformed-cubic* phase. Due to the volume mismatch between transformed shell and untransformed core, circumferential hoop stresses (expansive in nature) are developed at the interphase interface, resulting in decohesion or fracture. There is evidence that similar stresses develop but are relaxed for samples reversibly transformed at 1000°C.

When nanocrystalline m-Y₂O₃ is re-processed at 1.0 GPa/800°C, a relatively slow phase transformation to c-Y₂O₃ is observed. The result is a mixed

cubic/monoclinic nanocomposite, which is described as a self nanocomposite, since the constituent nanophases have the same Y_2O_3 composition.

It is ideal to control reverse transformation holding times such that the sample is not under HPHT conditions longer than necessary for complete conversion back to the cubic phase. As discussed in Chapter 8, prolonged treatment within the carbon heater can lead to undesirable effects. Samples that undergo complete reverse transformation back to the cubic phase are highly susceptible to coarsening at corner regions (Section 8.3) and can form a surface-localized oxycarbonate phase (Section 8.2).

10.4 Crystal Growth

As described in Section 7.3, when fine-grained c-Y₂O₃ is processed (annealed) at 3.0 GPa/1000°C/15-240 min, i.e. just above the critical phase transformation pressure at 2.5 GPa, there is a dramatic change in grain size and morphology, marked by the progressive growth of m-Y₂O₃ columnar grains from surface to interior. The m-Y₂O₃ columnar grains grow at the expense of the underlying c-Y₂O₃ equiaxed grains, eventually realizing via a competitive growth mechanism a well-developed textured structure.

This behavior suggests a method to grow large columnar-grained structures by restricting grain nucleation to a few favorable surface sites. This may be done, for example, by introducing a few indentations into the sample surface, such that the resulting stress concentrations induce early nucleation of new columnar grains, providing them with a head start in subsequent competitive growth into the sample interior.

It may also be possible to grow a *single crystal (monocrystal)* of monoclinic Y₂O₃ and other rear-earth sesquioxides under appropriate HPHT-processing conditions. For example, by establishing a temperature gradient in a rod-shaped sample, it may be possible to propagate a crystallization front from one end of the sample to the opposite end of the sample. To provide a favorable site for nucleation of a single grain, one end of the rod may be tapered down to a sharp point, but this gives no control of crystal orientation. To ensure growth of a single crystal with a specific orientation, a seed crystal may be used, as is standard practice in the crystal-growth field.

As shown in Figure 2.7, the pressure needed to induce a cubic-to-monoclinic transformation is reduced from 2.5 GPa at 1000°C to ~1.7 GPa at 1400°C. This opens the possibility of achieving higher single-crystal growth rates due to the faster kinetics at the higher temperature. For example, if the growth of a single crystal rod, say 10 cm in length, could be achieved in tens of minutes, this would surely be economically attractive. Moreover, such single-crystal growth may also purify the material by means of a zone-refinement method.

To our knowledge, crystal growth of high-pressure phases, such as m-Y₂O₃, by transformation-induced crystallization (TIC) has not previously been investigated, and therefore, is a fertile area for future research. No other process in use today has the ability to fabricate single crystals of high pressure oxide phases, such as m-Y₂O₃, entirely in the solid state. Application of the new technology to oxide-ceramics of commercial interest, such as monoclinic and tetragonal ZrO₂, warrants investigation.

The driving force for TIC is believed to have two components: (1) reduction in total grain-boundary energy in transforming fine equiaxed-grained c-Y₂O₃ into much coarser columnar-grained m-Y₂O₃; and (2) enhanced driving force for columnar-grain growth provided by pressure-induced transformation from c-Y₂O₃ phase to the higher density m-Y₂O₃ phase at the tips of the growing columnar grains. The latter is believed to be the principal rate-controlling mechanism driving the columnar-grained interface forward.

As a final point, there is still some uncertainty regarding the influence of carbon segregation at grain boundaries in controlling grain-boundary mobility

under high pressure. This issue needs to be resolved. Hence, another area for future research is to investigate the effect of placing an inert barrier layer between sample and heater, or better still encapsulating the sample in a carbon-gettering agent.

In diamond-grit manufacture, encapsulating the starting material (carbon/catalyst mixture) in an evacuated envelope of niobium to exclude oxygen and water vapor is a prerequisite for successful processing. *In the present case, such encapsulation would eliminate impurity contamination from ambient air, while providing an effective barrier between sample and carbon heater.*

10.5 Powder Processing

Fully dense nanocrystalline c-Y₂O₃ may also be produced from well-characterized nanopowder, making use of the so-called Transformation-Assisted Consolidation (TAC) process^{4,6}, previously developed at Rutgers' CNR. In this process, the starting material is a metastable nanopowder synthesized via a Chemical-Vapor Condensation (CVC) process⁸¹, also developed at Rutgers' CNR.

As shown in Figure 10.1 for TiO₂, a nanopowder compact of anatase-TiO₂ (metastable phase) subjected to pressure-assisted sintering (>1.5 GPa) is transformed into fully dense nanocrystalline rutile-TiO₂ (stable phase). Moreover, the grain size of the nanocrystalline product decreases with increasing pressure, such that at 5.5 GPa the final grain size is about one-half of the initial nanopowder particle size! Even higher pressures involve transformation to srinlakite-TiO₂, with consequences that have not yet been determined. Similarly, a nanopowder compact of γ -Al₂O₃ (metastable phase) is converted by high-pressure sintering into fully dense nanocrystalline α -Al₂O₃ (stable phase).

We conclude, therefore, that similar work on high-pressure sintering of nanopowder compacts of m-Y₂O₃ (metastable phase) is needed to establish an optimal procedure to generate fully dense nanocrystalline c-Y₂O₃ (stable phase). Previous work has shown that CVC-synthesized Y₂O₃ nanoparticles, with particle size <30 nm, have the metastable monoclinic structure; larger nanoparticles have the stable cubic structure. This behavior was attributed to the influence of the

Gibbs-Thomson effect, i.e. high pressures exerted on nano-sized particles by surface tension forces¹³.

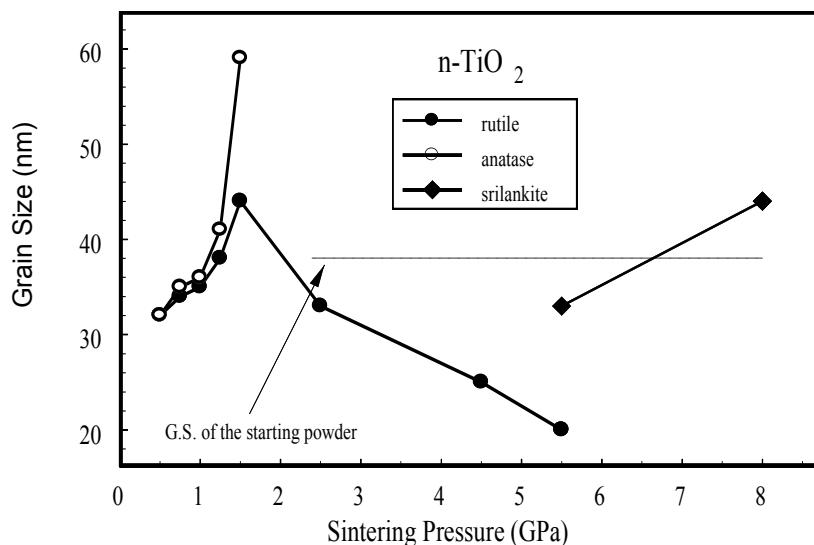


Figure 10.1 Effect of pressure on the grain size of sintered TiO_2 at $400^\circ\text{C}/60 \text{ min}$; anatase-to-rutile transformation occurs at 1.5 GPa.¹¹

A few experiments were carried out to determine the effect of high pressure on cold-compaction density (“green density”) of $\text{c-Y}_2\text{O}_3$ powders. Figure 10.2 shows that the green density for micron-sized particles is higher than that for nano-sized particles, apparently because the larger particles are less prone to aggregation. Even so, the green density of a nanopowder compact increases sharply with pressure up to about 2.0 GPa, and then flattens off with further increase in pressure. Apparently, nanoparticle aggregates are broken up under high pressure, and rearrange themselves to achieve a higher packing density. This is a significant finding, since without a high initial green density it is difficult to achieve full density by pressure-less or pressure-assisted sintering.

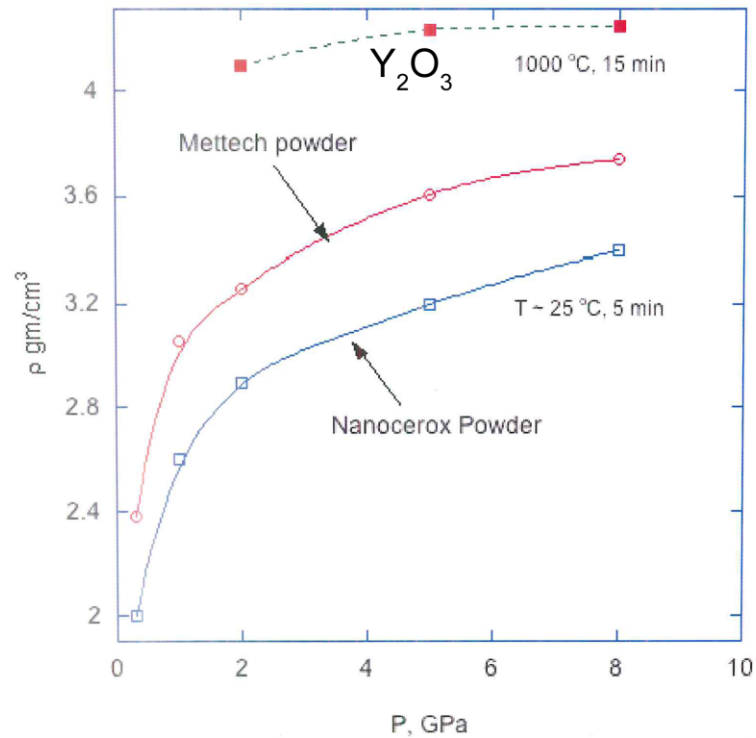


Figure 10.2 Density vs. hot-pressing pressure for Y_2O_3 and Y_2O_3 -MgO composites.⁸²

Figure 10.2 also shows that near theoretical density can be accomplished by sintering a nanopowder compact under high pressure, as observed for nano- TiO_2 and nano- Al_2O_3 . However, only a small fraction of the as-synthesized nanoparticles had the metastable m- Y_2O_3 structure, so that the full benefit of the TAC process was not realized. Further work, therefore, is needed to develop and optimize the CVC process to ensure the production of a metastable starting powder, as required to take full advantage of the TAC process.

We conclude that both transformation-assisted consolidation (TAC) and reversible-phase transformation (RPT) processes have merit, but it remains for future work to determine which of these two processes offers the greatest benefits in terms of process scalability, fabricability, and cost.

Finally, Y_2O_3 , Er_2O_3 , and Yb_2O_3 powders were consolidated at 8.0 GPa/1000°C/15 min and examined for structure and phase. As expected, all three compositions experienced transformation to the nanocrystalline monoclinic state, thus opening new possibilities for control of grain size and morphology of rare-earth sesquioxides.

11 APPENDICES

APPENDIX A: NANOPOWDER SOLUTION SYNTHESIS & DENSIFICATION

A1 Y_2O_3 Nanopowder Synthesis

Although much of this study involves HPHT processing of fully-densified Y_2O_3 samples, an in-house means by which to produce a nano-scale cubic- Y_2O_3 precursor has been developed.

Solution synthesis is an attractive means by which to produce nanoscale cubic- Y_2O_3 powders given that it is easily scalable and can be accomplished with off-the-shelf parts. The product can be used as-is or can be further refined using an inductively coupled plasma (ICP) system.

The process begins with a dilute solution of dissolved (0.13M) yttrium nitrate ($\text{Y}(\text{NO}_3)_3 \cdot 6\text{H}_2\text{O}$) that is added via peristaltic pump into a high-pH (>12) ammonium hydroxide (NH_4OH) bath. A high-shear mixer or attritor mill is used to rapidly disperse the precursor droplets, leading to near-instantaneous reaction with the ammonium hydroxide. The mixture is then centrifuged and washed several times to remove volatiles from the yttrium hydroxide ($\text{Y}(\text{OH})_3$) product. Pyrolyzation at 500°C produces nanoscale cubic- Y_2O_3 powder.

A2 Single-Step Consolidation and Densification via HPHT

Processing

In early experiments, Y_2O_3 -MgO and Y_2O_3 powders were densified using HPHT equipment. The Y_2O_3 powder was formed into green compacts at 0.3 GPa that were then subjected to applied pressures of 2, 5, and 8.0 GPa at 1000°C for 15 minutes. It was shown that the sintered density increases with pressure, with up to 99% theoretical density achieved at 8.0 GPa, Figure A.1.⁸²

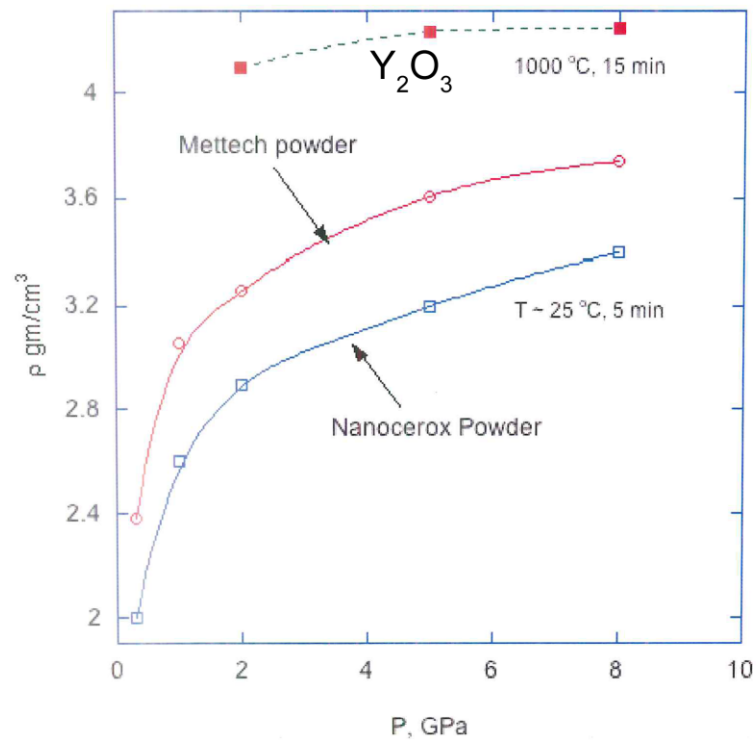


Figure A.1 Density vs. hot-pressing pressure for Y_2O_3 and Y_2O_3 -MgO composites.⁸²

Direct consolidation of Y_2O_3 and other Rare Earth sesquioxide powders at 8.0 GPa and 1000°C has been shown to produce a similar degree of near-theoretical densification. However, considerable internal stresses develop during

HPHT processing, resulting in samples' spontaneous fracturing upon removal from the encapsulating graphite crucibles.

Examination of the inner structure of materials densified via HPHT processing reveals uniform faceted intergranular fracture tendencies, Figure A.2. Section 8.3 discusses grain boundary embrittlement as a time-dependent effect that originates at fully-densified sample surfaces due to interaction with the graphite crucible during HPHT processing. At the onset of HPHT processing, powdered materials contain a high level of porosity that facilitates the influx and diffusion of carbon, logically leading to a greater extent of grain boundary interaction and embrittlement.

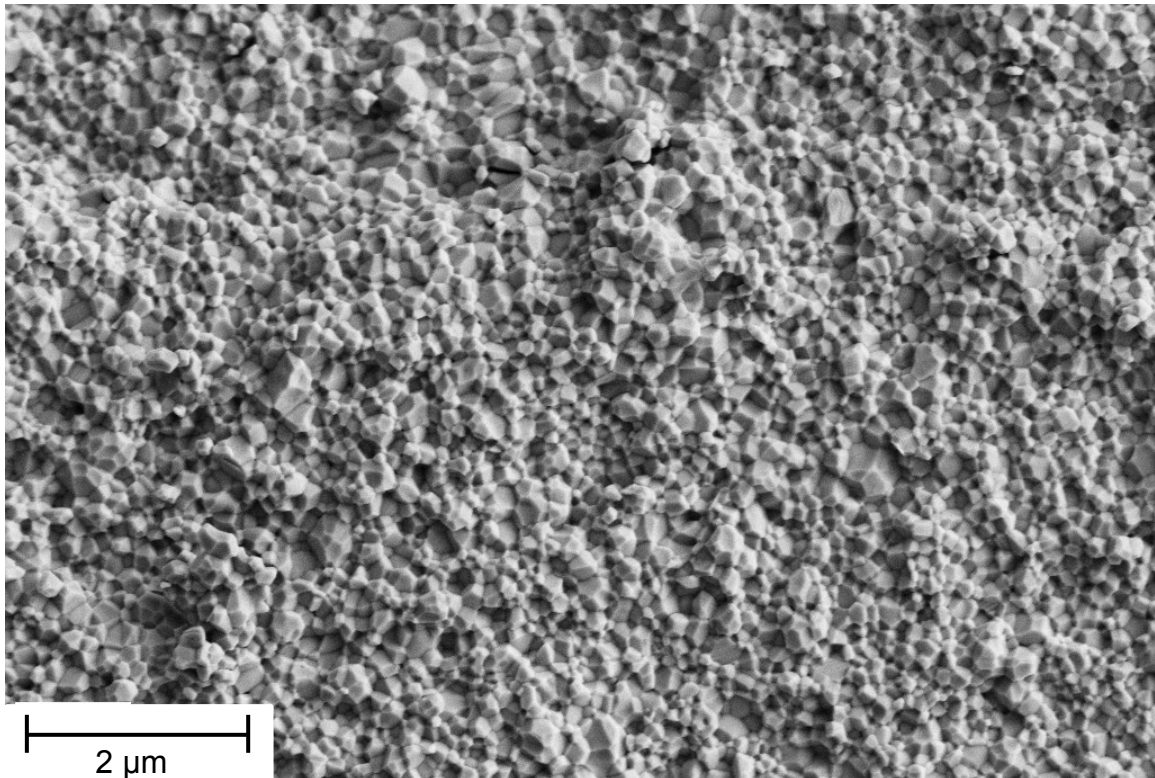


Figure A.2 SEM image of a powdered Y_2O_3 sample completely transformed to the monoclinic phase at 8.0 GPa and 1000°C for 15 mins.

A reasonable conclusion is that, although it is possible to densify and transform cubic Y_2O_3 powder directly into a bulk monoclinic product, it is not particularly beneficial to do so. Intermediate consolidation steps and optimizing HPHT processing methodology for powdered materials may reduce the likelihood of spontaneous stress-induced post-treatment fracturing, but it will be difficult to mitigate the effects due to the more rapid influx of carbon. Therefore, it is preferable to select for HPHT processing monolithic materials that have already been fully densified via conventional consolidation and sintering methods.

APPENDIX B: X-RAY DIFFRACTION POWDER DIFFRACTION FILES (PDF)

PDF#97-001-6394 (Cubic Y_2O_3)

Radiation=CuK α 1 Lambda=1.5406

Cubic, Ia-3 (206) Z=16

CELL: 10.6073 x 10.6073 x 10.6073 <90.0 x 90.0 x 90.0> P.S=

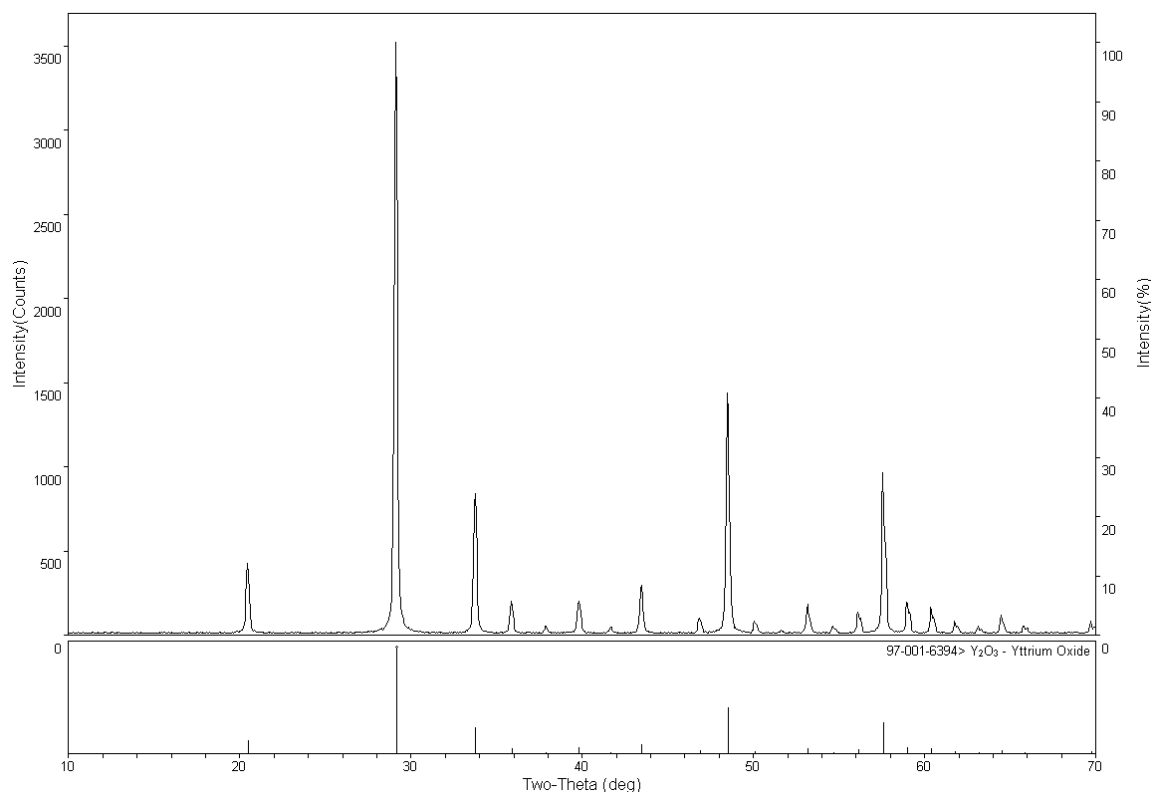
Density(c)=5.027 Density(m)= Mwt= Vol=1193.5

Strong Lines: 3.06/X 1.88/4 1.60/3 2.65/2 4.33/1 2.08/1 1.56/1 2.26/1

NOTE: FIZ#16394: "Refinement of the Y_2O_3 structure at 77K", Faucher, M.,
Acta Crystallographica B (24,1968-38,1982), v36 (1980) 3209-3211, Golden
Book of Phase Transitions, Wroclaw, v1 (2002) 1-123, R=0.038.

Temperature in Kelvin: 77.

Structure type : Mn_2O_3



PDF#97-016-0219 (Monoclinic Y_2O_3)Radiation=CuK α 1 Lambda=1.5406

Monoclinic, C2/m (12) Z=6

CELL: 14.1191 x 3.5174 x 8.6958 <90.0 x 100.279 x 90.0> P.S=

Density(c)=5.294 Density(m)= Mwt= Vol=424.9

Strong Lines: 2.73/X 2.97/9 3.03/9 3.12/9 1.90/7 2.80/7 2.12/6 2.85/5

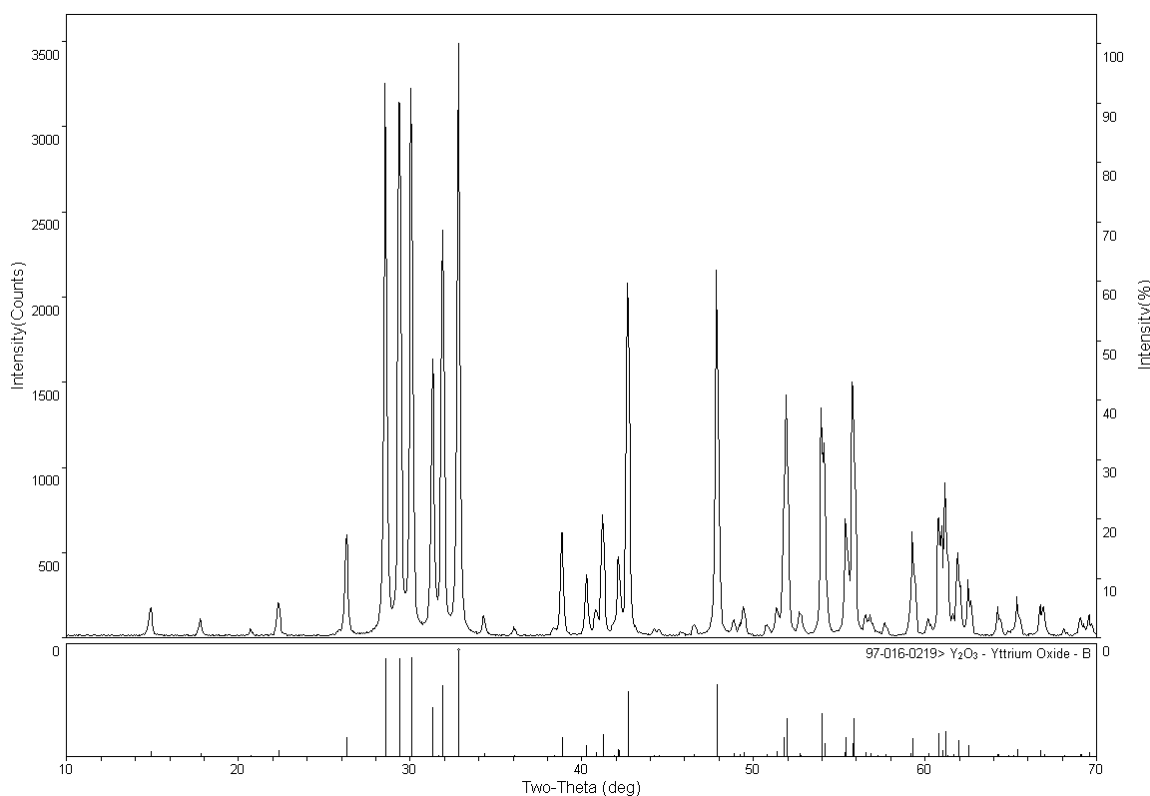
NOTE: FIZ#160219: "Ab initio study on structure and phase transition of A- and B-type rare-earth sesquioxides Ln_2O_3 (Ln= La-Lu, Y and Sc) based on density function theory", Wu Bo;Zinkevich, M.;Aldinger, F.;Wen Dingzhong;Chen Lu, Journal of Solid State Chemistry, v180 (2007) 3280-3287, Structure calculated theoretically.

Structure type : Sm_2O_3 .

X-ray diffraction from single crystal.

No R value given in the paper.

At least one temperature factor missing in the paper.



PDF#00-058-0472 (Yttrium Oxide Carbonate $\text{Y}_2\text{O}_2\text{CO}_3$)Radiation=CuK α Lambda=1.5418

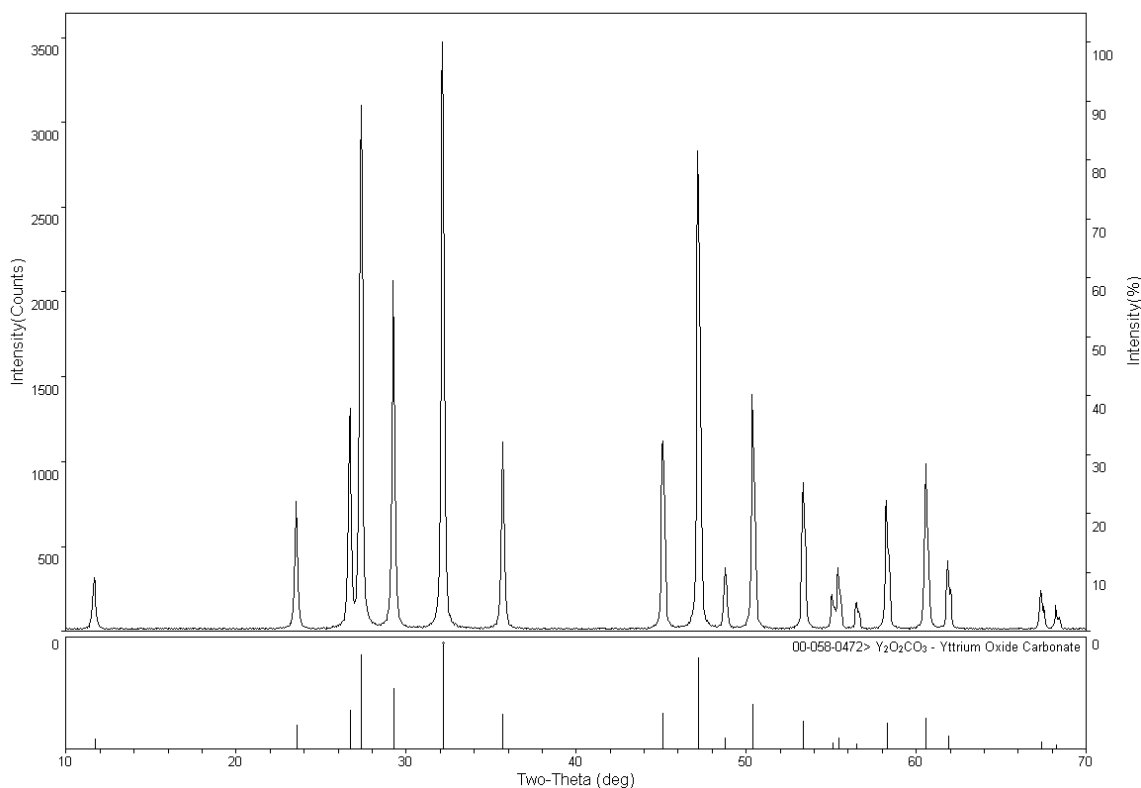
Hexagonal - Powder Diffraction, P63/mmc (194) Z=
 CELL: 3.848 x 3.848 x 15.078 <90.0 x 90.0 x 120.0> P.S=hP?
 Density(c)= Density(m)= Mwt=269.82 Vol=193.35 F(20)=39(0.0190,27/0)
 Strong Lines: 2.78/X 3.26/9 1.92/9 3.05/6 1.81/4 3.33/4 2.01/3 2.51/3

Decomposes to "Y₂ O₃" at ~773 K.

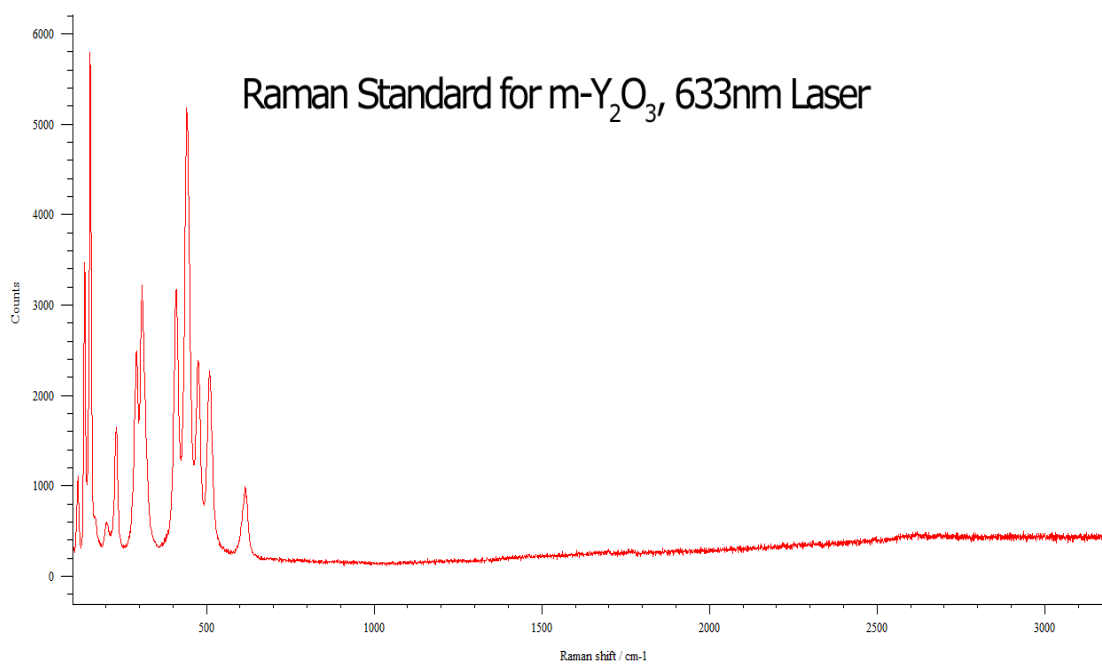
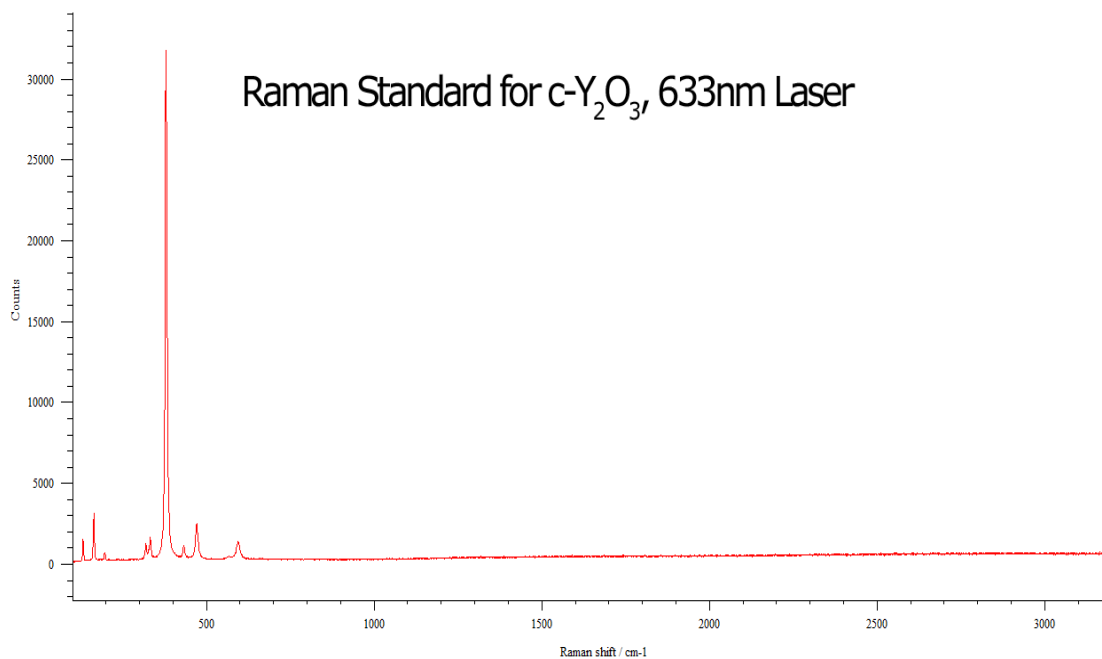
Sample Preparation: "Y (C H₃ C O O)₃ · 4 H₂ O" was calcined at 673 K for 6 hours and mixed with a 0.476"Li₂ C O₃"-0.270"Na₂ C O₃"-0.254"K₂ C O₃" eutectic flux mixture and heated at 723 K for 12 hours in flowing "C O₂"(10%)"N₂".

The sample was calcined in air at 673 K for 1 hour and washed with "H₂ O" and then ethanol.

Unit Cell Data Source: Powder Diffraction.



APPENDIX C: FULL-RANGE RAMAN SPECTRA FOR C-Y₂O₃ AND M-Y₂O₃ WITH 633NM SOURCE



APPENDIX D: MONOCLINIC Y₂O₃ JEMS SIMULATION

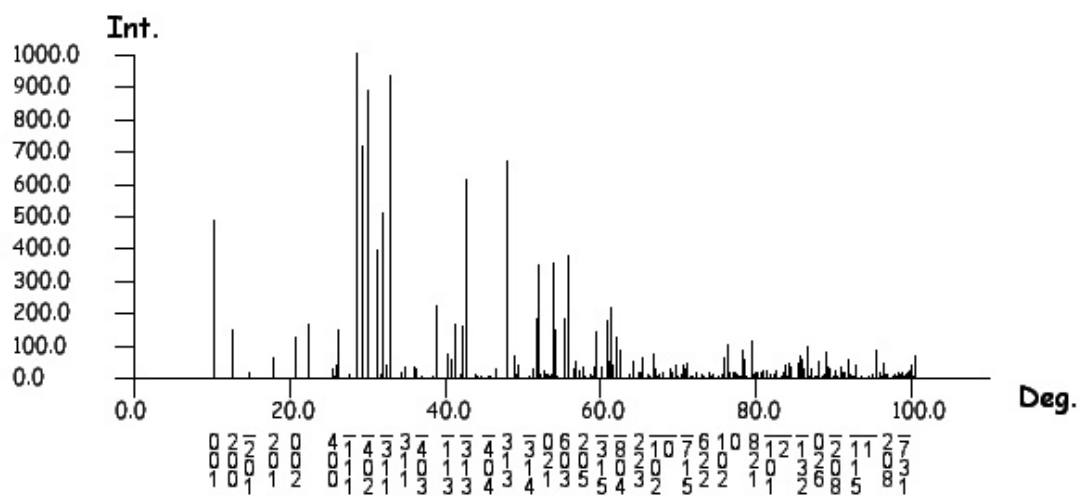
FOR TEM ANALYSIS

```

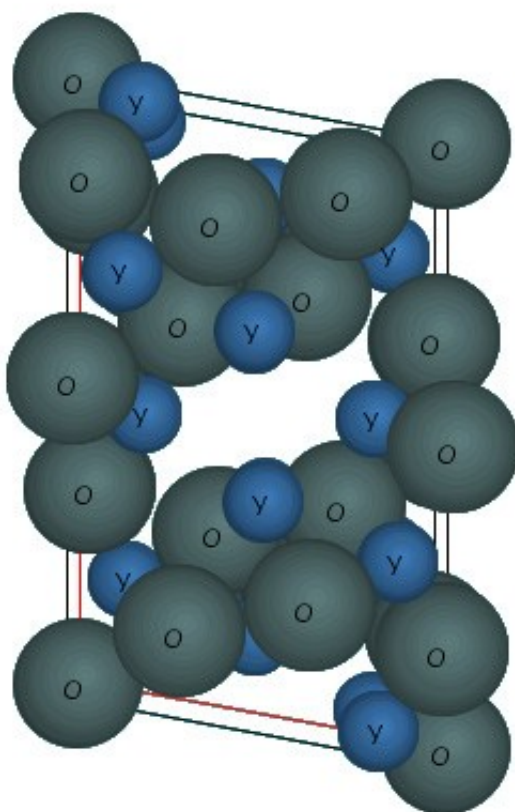
file|C:\Documents and Settings\admin\Desktop\mono Y2O3.txt
name|mono Y2O3
creator|Rao
date|Wed Aug 18 17:00:59 EDT 2010
system|monoclinic
superCell|false
HMSymbol|12|2|1|0|0| C 2/m
rps|0| x , y , z
rps|1| -x , y , -z
lattice|0|1.41191
lattice|1|0.35174
lattice|2|0.86958
lattice|3|90.0
lattice|4|100.279
lattice|5|90.0
atom|0|Y ,_,0.6351,0.000,0.488,0.005,1.000,0.060,Def,2
atom|1|Y ,_,0.6914,0.000,0.1374,0.005,1.000,0.060,Def,2
atom|2|Y ,_,0.968,0.000,0.1858,0.005,1.000,0.060,Def,2
atom|3|O ,_,0.1281,0.000,0.2818,0.005,1.000,0.029,Def,2
atom|4|O ,_,0.8255,0.0304,0.0304,0.005,1.000,0.029,Def,2
atom|5|O ,_,0.8255,0.000,0.0304,0.005,1.000,0.029,Def,2
atom|6|O ,_,0.7933,0.000,0.3775,0.005,1.000,0.029,Def,2
atom|7|O ,_,0.000,0.500,0.000,0.005,1.000,0.029,Def,2
aff|0|Y |4.129,27.548,3.012,5.088,1.179,0.591,0.0,0.0|Smith - Burge Acta Cryst. 15 (1962), 182
aff|1|O |0.455,23.78,0.917,7.622,0.472,2.144,0.138,0.296|Doyle - Turner Acta Cryst. A24
(1968), 390
aff|0|Y |0.56627274,164.76625,0.6687032,0.064765856,2.6360722,2.04221420.10834482,0.1920
5335,0.0064134332,0.016797304,0.970128,1.64599|Earl J. Kirkland, Advanced Computing in
Electron Microscopy
aff|1|O |0.36859024,0.36754256,0.13289645,19.395483,0.27710122,0.367539550.08393093,0.7
58355,0.18163113,2.0436034,0.0010528987,0.031250093|Earl J. Kirkland, Advanced
Computing in Electron Microscopy
nsl|0|Y |0.775
nsl|1|O |0.58
aff|0|Y |0.3234,0.1244,1.2737,1.1948,3.2115,7.2756,4.0563,34.143,3.7962,111.2079|L. Peng et
al., Acta Cryst. A52 (1996) 257-276::Def
aff|1|O |0.0365,0.0652,0.1729,0.6184,0.5805,2.9449,0.8814,9.6298,0.3121,28.2195|L. Peng et
al., Acta Cryst. A52 (1996) 257-276::Def
aff|0|Y
|17.776,1.4029,10.2946,12.8006,5.72629,0.125599,3.26588,104.354,1.91213|XRay::*RHF::Def
aff|1|O |3.0485,13.2771,2.2868,5.7011,1.5463,0.3239,0.867,32.9089,0.2508|XRay:: RHF::Def

```


Crystal : mono-1::Anode : Cu Ka1



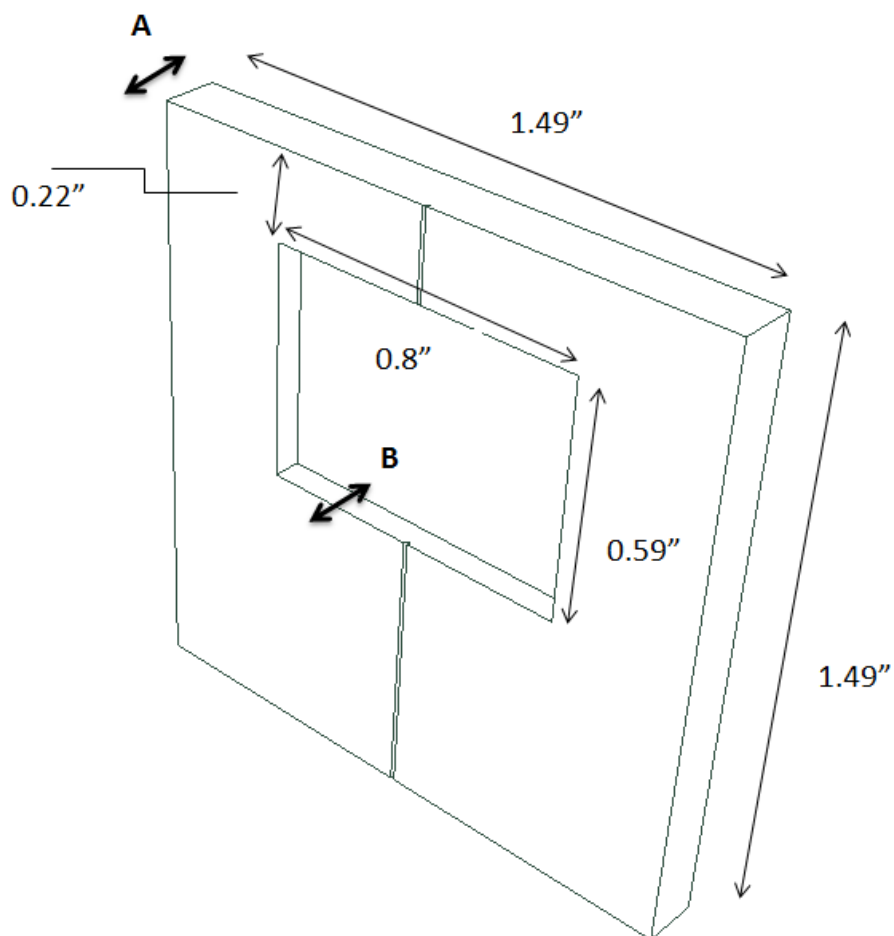
γ (2) at : (0.968, 1.0, 0.1858)



mono Y2O3 : [0, 1, 0]

APPENDIX E: XRD HOLDER DESIGNS

X'Pert Diffractometer Sample Holder for Powder and Bulk Samples



Material: Aluminum, with front and back milled parallel.

Dimensions:

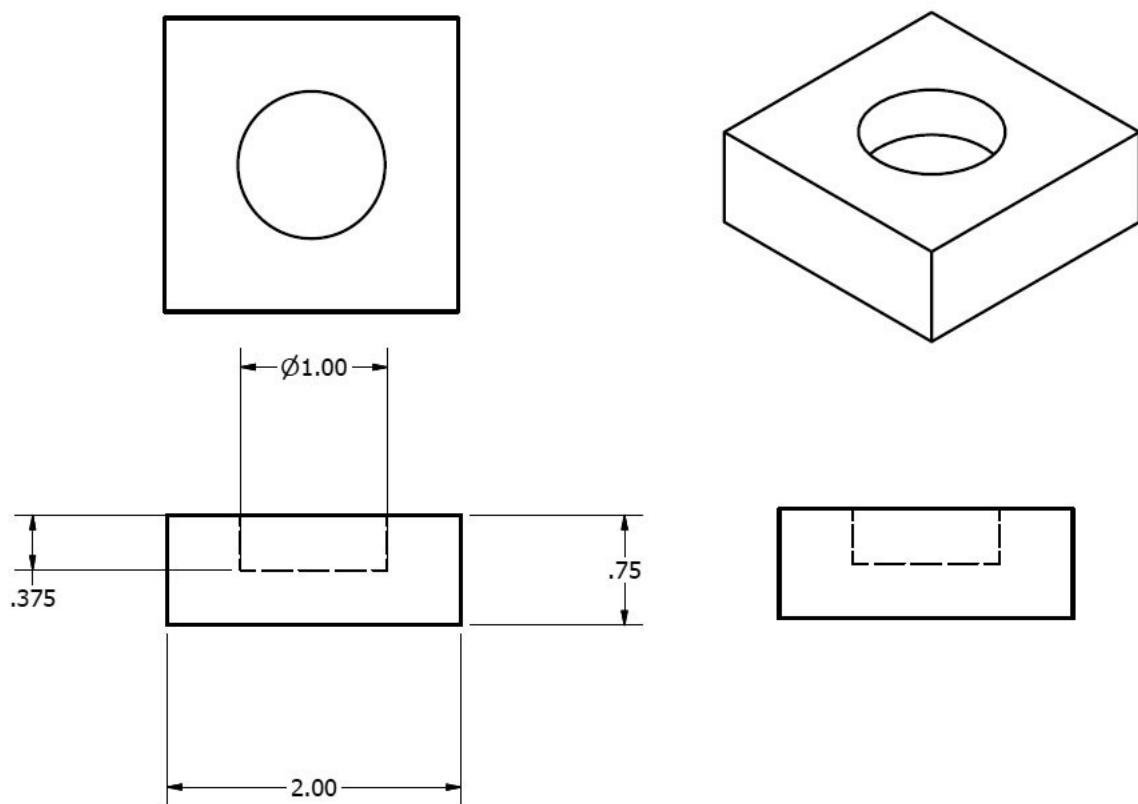
Holder 1: A: 0.14"; B: 0.07"

Holder 2: A: 0.14"; B: 0.035"

Holder 3: A: 0.18"; B: 0.14"

Holder 4: A: 0.18"; B: 0.10"

Phillips X-Ray Diffractometer Sample Holder for Bulk Samples



Material: Aluminum with front and back milled parallel.

Dimensions: Three holders with receptacle depths of 0.25", 0.375", and 0.5".

12 REFERENCES

- 1 Hogan, P., Stefanik, T., Willingham, C., Gentilman, R., "Transparent Yttria for IR Windows and Domes – Past and Present" Raytheon Integrated Defense Systems, Presented at 10th DoD Electromagnetic Windows Symposium, (2004).
- 2 Owen, D.M., Chokshi, A. H., "An evaluation of the Densification Characteristics of Nanocrystalline Materials," *Nanostructured Materials*, **2**(2), 181-187 (1993).
- 3 Hahn, H., "Microstructure and Properties of Nanostructured Oxides," *Nanostructured Materials*, **2**(3), 251-265 (1993).
- 4 Liao, S., Chen, Y., Mayo, W., Kear, B. H., "Transformation-Assisted Consolidation of Bulk Nanocrystalline TiO₂," *Nanostructured materials*, **11**(4), 553-557 (1999).
- 5 Liao, S.-C., Pae, K. D., Mayo, W. E., "Retention of Nanoscale Grain Size in Bulk Sintered Materials via a Pressure-Induced Phase Transformation," *Nanostructured Materials*, **8**(6), Issue 6, 645-656 (1997).
- 6 Liao, S.-C., Y.-J. Chen, Kear, B.H., Mayo, W. E., "High Pressure/Low Temperature Sintering of Nanocrystalline Alumina," *Nanostructured Materials*, **10**(6), 1063-1079 (1998).
- 7 Liao, S.-C., Mayo, W. E., Pae, K. D., "Theory of High Pressure/Low Temperature Sintering of Bulk Nanocrystalline TiO₂," *Acta Materialia*, **45**(10), 4027-4040 (1997).
- 8 Liao, S.-C., Pae, K. D., Mayo, W. E., "The Effect of High Pressure on Phase Transformation of Nanocrystalline TiO₂ During Hot-Pressing," *Nanostructured Materials*, **5**(3), 319-325 (1995).
- 9 Liao, S.-C., Pae, K. D., Mayo, W. E., "High Pressure and Low Temperature Sintering of Bulk Nanocrystalline TiO₂," *Materials Science and Engineering: A*, **204**(1-2), 152-159 (1995).
- 10 Kear, B. H., Al-Sharab, J. F., Sadangi, R. K., Deutsch, S., Kavukcuoglu, N. B., Tse, S. D., Mann, A., Voronov, O. A. and Nordahl, C. S., "On the Conversion of Bulk Polycrystalline Y₂O₃ into the Nanocrystalline State," *Journal of the American Ceramic Society*, **94**, 1744–1746 (2011).
- 11 Kear, B. H., Mukherjee, A. K., "Far-from-Equilibrium Processing of Nanostructured Ceramics," *Materials Processing Handbook*, 7-1 to 7-18 (Mar 2007).

- 12 Goldschmidt, V. M., Ulrich, F., Barth, T., Skrifter Norske Videnskaps-Akad. Oslo, I. Mat. Naturv. Kl. **52**, 5–4 (1925).
- 13 Skandan, G., Foster, C., Frase, H., Ali, M., Parker, J., & Hahn, H., “Phase Characterization and Stabilization Due to Grain Size Effects of Nanostructured Y_2O_3 ,” *Nanostructured Materials*, **1**(4), 313–322 (1992).
- 14 Zinkevich, M., “Thermodynamics of Rare Earth Sesquioxides,” *Progress in Materials Science*, **52**(4), 597–647 (2007).
- 15 Husson, E., Proust, C., Gillet, P., & Itie, J., “Phase Transitions in Yttrium Oxide at High Pressure Studied by Raman Spectroscopy,” *Materials Research Bulletin*, **34**(12-13), 2085–2092 (1999).
- 16 Lejus, AM, and Collongues, R., “Lanthanide Oxides, Structural Anisotropy, Physical and Mechanical Properties,” *Current Topics in Materials Science*, **4**, 481–577 (1980).
- 17 Sawyer, J. O., Hyde, B. G., Eyring, L., “Pressure and Polymorphism in Rare Earth Sesquioxides,” *Inorg Chem*, **4** 426–7 (1965).
- 18 Fedorov, P., & Nazarkin, M., “On Polymorphism and Morphotropism of Rare Earth Sesquioxides,” *Crystallography Reports*, **47**(2), 316–321 (2002).
- 19 Foex, M.; Traverse, J., “Investigations About Crystalline Transformation in Rare Earth Sesquioxides at High Temperatures,” *Rev. Int. Hautes Temp. Refract*, **3**, 429–53 (1966).
- 20 Warshaw, I., and Rustum, R., “Polymorphism of the Rare Earth Sesquioxides,” *The Journal of Physical Chemistry*, **65** (11), 2048–2051 (1961).
- 21 Weigel F, Scherer V., “Chemistry of Promethium. II. Polymorphism of Promethium-(III) Oxide,” *Radiochim Acta*, **4**(4):197–202 1965.
- 22 Glushkova, V. B., Boganov, A. G., “Polymorphism of Rare-Earth Sesquioxides,” *Russian Chemical Bulletin*, **14** (7) 1101–1107 (1965).
- 23 Shannon, R. D., Prewitt C. T., “Effective Ionic Radii in Oxides and Fluorides,” *Acta Crystallographica Section B*, **25**, 925–946 (1969).
- 24 Atou, T., Kusaba, K., Tsuchida, Y., Utsumi, W., Yagi, T., Syono, Y., “Reversible B-type–A-type Transition of Sm_2O_3 Under High Pressure,” *Mater Res Bull*, **24**, 1171–1176 (1989).
- 25 Chen, G., Stump, N. A., Haire, R.G., Peterson, J. R., “Study of the Phase Behavior of Eu_2O_3 Under Pressure via Luminescence of Eu^{3+} ,” *J Alloys Compd*, **181**, 503–509 (1992).

- 26 Chen, G., Stump, N. A., Haire, R. G., Burns, J. B., Peterson, J. R., "A Luminescence Study of B-type Eu_2O_3 Under Pressure," *High Press Res* **12**, 83–90 (1994).
- 27 Meyer, C., Sanchez, J.P., Thomasson, J., Itie, J. P., "Mossbauer and Energy-Dispersive X-ray-Diffraction Studies of the Pressure-Induced Crystallographic Phase Transition in C-type Yb_2O_3 ," *Phys Rev B*, **51**, 12187–93 1995.
- 28 Chen, G., Peterson, J. R., Brister, K. E., "An Energy-Dispersive X-ray Diffraction Study of Monoclinic Eu_2O_3 Under Pressure," *J Solid State Chem*, **111**, 437–9 (1994).
- 29 Guo, Q., Zhao, Y., et-al, "Pressure-Induced Cubic to Monoclinic Phase Transformation in Erbium Sesquioxide Er_2O_3 ," *Inorganic Chemistry*, **45**(15), 6164-6169 (2007).
- 30 Ma, Y. M., Ma, H. A., Pan, Y. W., Cui, Q. L., Lin, B. B., Cui, T., et al, "Pressure-Induced Structure Phase Transition on Y_2O_3 ," *He Jishu/Nucl Tech*, **25**, 841–4 (2002).
- 31 Atou, T., Kusaba, K., Fukuoka, K., Kikuchi, M., Syono, Y., "Shock-Induced Phase Transition of M_2O_3 (M=Sc, Y, Sm, Gd, and In)-Type Compounds," *J Solid State Chem*, **89**, 378–84 (1990).
- 32 Atou, T., Kikuchi, M., Fukuoka, K., Syono, Y., "Shock-Induced Phase Transition of Scandium Sesquioxide: Geometric Factor Governing High Pressure Transitions on Rare Earth Sesquioxides," *AIP Conf Proc*, **309**, 331–4 (1994).
- 33 Hoekstra, H. R., & Gingerich, K. A., "High-Pressure B-type Polymorphs of Some Rare-Earth Sesquioxides," *Science*, **146**(3648), 1163–1164 (1964).
- 34 Halevy, I., et al, "Pressure-Induced Structural Phase Transitions in Y_2O_3 Sesquioxide," *Journal of Physics: Conference Series*, **215**(1), (2010).
- 35 German, V. N., Podarets, A. M., Tarasova, L. A., *Neorg. Mater.* **18**, 1736 (1982).
- 36 Husson, E., Proust, C., Gillet, P., Itie, J. P., "Phase Transitions in Yttrium Oxide at High Pressure Studied by Raman Spectroscopy," *Materials Research Bulletin* **34** (12-13), 2085–2092 (1999).
- 37 Wang, L., Yang, W., et al, "Size-Dependent Amorphization of Nanoscale Y_2O_3 at High Pressure," *Physical Review Letters*, **105**(9), 1-4 (2010).
- 38 Barsoum, M.W., "Fundamentals of Ceramics," 67–69, McGraw-Hill Co. Inc., 1997, ISBN 978-0070055216.

- 39 Hongo, T., Kondo, K. I., et al, "High Pressure Raman Spectroscopic Study of Structural Phase Transition in Samarium Oxide," *Journal of Materials Science*, **42**(8), 2582–2585 (2007).
- 40 Hoekstra, H. R., "Phase Relationships in Rare Earth Sesquioxides at High Pressure," *Inorg Chem*, **5**, 754–7 (1966).
- 41 Wang, L., Pan, Y., Ding, Y., Yang, W., Mao, W. L., Sinogeikin, S. V., Meng, Y., et al., "High-Pressure Induced Phase Transitions of Y₂O₃ and Y₂O₃:Eu³⁺," *Applied Physics Letters*, **94**(6), 061921 (2009).
- 42 Guo, Q., Zhao, Y., Jiang, C., Mao, W. L., & Wang, Z., "Phase Transformation in Sm₂O₃ at High Pressure: In situ Synchrotron X-ray Diffraction Study and ab initio DFT Calculation," *Solid State Communications*, **145**(5-6), 250-254 (2008).
- 43 Lonappan, D., Chandra Shekar, N. V., Sahu, P. C., Kumarasamy, B. V., Bandyopadhyay, a. K., Rajagopalan, M., "Cubic to Hexagonal Structural Transformation in Gd₂O₃ at High Pressure," *Philosophical Magazine Letters*, **88**(7), 473-479 (2008).
- 44 Dilawar, N., Varandani, D., Mehrotra, S., Poswal, H. K., Sharma, S. M., Bandyopadhyay, A. K., "Anomalous High Pressure Behaviour in Nanosized Rare Earth Sesquioxides," *Nanotechnology*, **19**(11), 115703 (2008)..
- 45 Sharma, N. D., Singh, J., Dogra, S., Varandani, D., Poswal, H. K., Sharma, S. M., & Bandyopadhyay, A. K., "Pressure-Induced Anomalous Phase Transformation in Nano-Crystalline Dysprosium Sesquioxide," *Journal of Raman Spectroscopy*, **42**(3), 438-444 (2011).
- 46 Paton, M. G., Maslen, E. N., "A Refinement of the Crystal Structure of Yttria," *Acta Crystallographica*, **19**(3), 307–310 (1965).
- 47 Katagiri, S., Ishizawa, N., Marumo, F., "A New High Temperature Modification of Face-Centered Cubic Y₂O₃," *Powder Diffraction*, **8**, 60 (1993).
- 48 Tresvyatkii S. G., Lopato L. M., Schwetschenko A. W., Kutschewskij A. E. "Untersuchung des Einflusses Hochschmelzender Oxide der Elemente II. Gruppe des Periodischen Systems. Auf Polymorphe Hochtem- peratur-Umwandlungen von Oxiden der Seltenerdelemente," *Colloq Intern Centre Natl Rech Sci Paris*, **205**, 247–53 (1971).
- 49 Shevtchenko A. V., Lopato, L. M., "TA Method Application to the Highest Refractory Oxide Systems Investigation," *Thermochim Acta*, **93**, 537–40 (1985).
- 50 Shpil'rain E. E., Kagan D. N., Barkhatov, L. S., Koroleva, V. V., "Measurement of the Enthalpy of Solid and Liquid Phases of Yttria," *High Temp High Press*, **8**, 183–6 (1976).

- 51 Glushkova, V. B., Adylov, G.T., Yusupova, S. G., Sigalov, L. M., Kravchinskaya, M. V., Rakhimov, R. K., "Phase Ratios in $\text{YO}_{1.5}$ – $\text{TbO}_{1.5}$ and $\text{YO}_{1.5}$ – TbO_x Systems," *Inorg Mater*, **24**, 665–9 (1988).
- 52 Adylov, G. T., Voronov, V. G., Sigalov, L.M., "The System Nd_2O_3 – Y_2O_3 ," *Inorg Mater*, **23**, 1644–6 (1987).
- 53 Andrievskaya, E. R., Zaitseva, Z. A., Shevchenko, A. V., Lopato, L. M., "Phase Diagram of the Eu_2O_3 – Y_2O_3 System," *Inorg Mater*, **33**, 390–3 (1997).
- 54 Navrotsky, A., Benoist, L., Lefebvre, H., "Direct Calorimetric Measurement of Enthalpies of Phase Transitions at 2000–2400° C in Yttria and Zirconia," *J Am Ceram Soc*, **88**, 2942–4 (2005).
- 55 Swamy, V., Dubrovinskaya, N. A., Dubrovinsky, L. S., "High-Temperature Powder X-ray Diffraction of Yttria to Melting Point," *J Mater Res*, **14**, 456–9 (1999).
- 56 Swamy, V., Seifert, H. J., & Aldinger, F., "Thermodynamic Properties of Y_2O_3 Phases and the Yttrium-Oxygen Phase Diagram," *Journal of Alloys and Compounds*, **269**(1-2), 201–207 (1998).
- 57 Granier, B., Heurtault, S., "Density of Liquid Rare-Earth Sesquioxides," *J Am Ceram Soc*, **71**, 466–8 (1988).
- 58 Hlavac, J., "Melting Temperatures of Refractory Oxides Part 1," *Pure Appl Chem*, **54**, 682–8 (1982).
- 59 Coutures, J. P., Rand, M. H., "Melting Temperatures of Refractory Oxides Part 2 Lanthanoid Sesquioxides," *Pure Appl Chem*; **61**, 1461–82 (1989).
- 60 Navrotsky, A., Benoist, L., Lefebvre, H., "Direct Calorimetric Measurement of Enthalpies of Phase Transitions at 2000°–2400°C in Yttria and Zirconia." *International Studies Review*, **7**(3), 387–406 (2005).
- 61 Guo, B., Harvey, a., Risbud, S. H., & Kennedy, I. M., "The Formation of Cubic and Monoclinic Y_2O_3 Nanoparticles in a Gas-Phase Flame Process," *Philosophical Magazine Letters*, **86**(7), 457–467 (2006).
- 62 Guo, B., Harvey, A. S., et-al, "Atmospheric Pressure Synthesis of Heavy Rare Earth Sesquioxide Nanoparticles of the Uncommon Monoclinic Phase," *Journal of the American Ceramic Society*, **90**(11) 3683–3686 (2007).
- 63 Guo, B., & Luo, Z.-P., "Particle Size Effect on the Crystal Structure of Y_2O_3 Particles Formed in a Flame Aerosol Process," *Journal of the American Ceramic Society*, **91**(5), 1653–1658 (2008).

- 64 Guo, B., Mukundan, M., & Yim, H., "Flame Aerosol Synthesis of Phase-Pure Monoclinic Y₂O₃ Particles via Particle Size Control. Powder Technology, **191**(3), 231-234 (2009).
- 65 Lane, R., Battat, B., "IR Windows and Domes Materials - Critical Review and Technology Assessment," AMMTIAC, (1999).
- 66 Harris, D. C., "Materials for Infrared Windows and Domes: Properties and Performance," The International Society for Optical Engineering, (1999). ISBN 0-8194-3482-5.
- 67 Smith, W. F., Hashemi, J., "Foundations of Materials Science and Engineering," (4th ed.), McGraw-Hill, (2006). ISBN 0-07-295358-6.
- 68 Adelhelm, C., Pickert, T., Balden, M., Rasinski, M., Plocinski, T., Ziebert, C., Koch, F., et al. (2009). Monoclinic B-Phase Erbium Sesquioxide (Er₂O₃) Thin Films by Filtered Cathodic Arc Deposition. Scripta Materialia, **61**(8), 789-792.
- 69 Voronov, O. A., Tompa, G. S., Kear, B. H., "High Pressure-High Temperature Device for making Diamond Materials", Diamond Materials, The Electrochemical Society, **25**, 264-271, (2001).
- 70 Voronov, O. A., Street, K. W., "Raman scattering in a new carbon material," Diamond & Related Materials, **19**, 31-39 (2010).
- 71 Voronov, O. A., Kear, B. H., "Diamond-Hardfaced Carbide/Metal Composites for Submersible-Pump Bearings in Geothermal Wells," Geothermal Resources Council Transactions, **33**, 653-657 (2009).
- 72 Voronov, O. A., Kear, B. H., Yan, P., "Supercell for Achieving Very High Static Pressure and Temperature in a Relatively Large Working Volume," Report DMI-0060309 to NSF, 1-24, (2001).
- 73 Voronov, O. A., Kear, B. H., "Method for Rapidly Synthesizing Monolithic Polycrystalline Diamond Articles," U.S. Patent 8,021,639 B1, Sept. 20th, 2011.
- 74 Voronov, O. A., "High Pressure and High Temperature Apparatus", US Patent 6,942,729, Sept.13, (2005).
- 75 Scherrer, P., "Bestimmung der Grösse und der inneren Struktur von Kolloidteilchen mittels Röntgenstrahlen," Nachr. Ges. Wiss. Göttingen, **26**, 98–100 (1918).
- 76 Wilson, E., Decius, J.C., Cross, P., "Molecular Vibrations: The Theory of Infrared and Raman Vibrational Spectra," Dover Publications, NY, 1955. ISBN 0-486-63941-X.

77 Chen, J., Weidner, D. J., Parise, J. B., Vaughan, M. T., Raterron, P., "Observation of Cation Reordering during the Olivine-Spinel Transition in Fayalite by In Situ Synchrotron X-Ray Diffraction at High Pressure and Temperature," *Physical Review Letters*, **86**, 4072-4075 (2001).

78 Akdogan, E. K., Savklydz, I, Berke., B., Zhong, Z., Wang, L., Vaughan, M., Tsakalakos, T., "High-Pressure Phase Transformations in MgO-Y₂O₃ Nanocomposites," *Applied Physics Letters*, **99**, 141915 (2011).

79 Akdogan, E. K., Savklydz, I, Berke., B., Zhong, Z., Wang, L., Weidner, D., Croft, M. C., Tsakalakos, T., "Pressure Effects on Phase Equilibria and Solid Solubility in MgO-Y₂O₃ Nanocomposites," *Journal of Applied Physics*, **111**, 053506 (2012).

80 Analysis performed by Dr. Jafar Al-Sharab with the assistance of Dr. Silva.

81 Singhal, A., Skandan, G., Wang, A, et-al, "On Nanoparticle Aggregation During Vapor Phase Synthesis," *Nanostructured Materials*, **11**(4), 545-552 (1999).

82 Kear, B.H., "Fabrication of Y₂O₃-MgO Nanocomposites," Program Review Meeting at Arlington, VA, July 2008.